https://orcid.org/0000-0003-0284-5843
https://doi.org/10.15388/vu.thesis.812

VILNIUS UNIVERSITY
CENTER FOR PHYSICAL SCIENCES AND TECHNOLOGY

Romualdas Jonas Čepas

Studies of Charge Carrier Recombination and Transport in Disordered Materials and their Application in Optoelectronic Devices

DOCTORAL DISSERTATION

Technology Sciences,
Materials Engineering (T 008)

VILNIUS 2025

The dissertation was prepared between 2019 and 2024 in Vilnius University, Institute of Chemical Physics.

Academic Supervisor – Dr. Kristijonas Genevičius (Vilnius University, Institute of Chemical Physics, Material Engineering, T 008)

This doctoral dissertation will be defended in a public meeting of the Dissertation Defense Panel:

Chairman – Prof. Dr. Nerija Žurauskienė (Center of Physical Sciences and Technology, Technology Sciences, Material Engineering T 008)

Members:
Prof. Habil. Dr. Vidmantas Gulbinas (Center of Physical Sciences and Technology, Nature Sciences, Physics, N 002),
Prof. Dr. Edvinas Orentas (Vilnius University, Nature Sciences, Chemistry, N 003),
Dr. Steponas Raišys (Vilnius University, Technology Sciences, Material Engineering, T 008),
Prof. Dr. Arvydas Ruseckas (University of St. Andrews, Scotland, Technology Sciences, Material Engineering, T 008).

The dissertation shall be defended at a public meeting of the Dissertation Defense Panel 11:00 on 12 September 2025 in Room B336 of the National Center of Physical Sciences and Technology.
Address: Saulėtekio ave. 3 10257, Vilnius, Lithuania
Tel. +370 645 15550; e-mail: romualdas.cepas@ff.vu.lt

The text of this dissertation can be accessed at the library of Vilnius University, as well as on the website of Vilnius University:
www.vu.lt/lt/naujienos/ivykiu-kalendorius

https://orcid.org/0000-0003-0284-5843
https://doi.org/10.15388/vu.thesis.812

VILNIAUS UNIVERSITETAS
FIZINIŲ IR TECHNOLOGIJOS MOKSLŲ CENTRAS

Romualdas Jonas Čepas

Krūvininkų rekombinacijos ir pernašos tyrimai netvarkiose medžiagose ir jų taikymas optoelektroniniuose prietaisuose

DAKTARO DISERTACIJA

Technologijos mokslai,
Medžiagų inžinerija (T 008)

VILNIUS 2025

Disertacija rengta 2019–2024 metais Vilniaus universitete Cheminės Fizikos institute.

Mokslinis vadovas – Dr. Kristijonas Genevičius (Vilniaus universitetas, tehcnologijos mokslai, medžiagų inžinerija, T 008).

Gynimo taryba:
Pirmininkė – prof. Dr. Nerija Žurauskienė (Fizinių ir technologijos mokslų centras, Technologijos mokslai, Medžiagų inžinerija T 008)
Nariai:
Prof. habil. dr. Vidmantas Gulbinas (Fizinių ir technologijos mokslų centras, gamtos mokslai, fizika, N 002),
Prof. dr. Edvinas Orentas (Vilniaus universitetas, gamtos mokslai, chemija, N 003),
Dr. Steponas Raišys (Vilniaus universitetas, technologijos mokslai, medžiagų inžinerija, T 008),
Prof. dr. Arvydas Ruseckas (University of St. Andrews, Škotija, technologijos mokslai, medžiagų inžinerija, T 008).

Disertacija ginama viešame Gynimo tarybos posėdyje 2025 m. Rugsėjo mėn. 12 d. 11 val. Nacionaliniame fizinių ir technologijos mokslų centre B336 posėdžių salėje.
Adresas: : Saulėtekio al. 3 10257, Vilnius, Lietuva
Tel. +370 645 15550; e-mail: romualdas.cepas@ff.vu.lt

Disertaciją galima peržiūrėti Vilniaus universiteto bibliotekoje ir VU interneto svetainėje adresu:
https://www.vu.lt/naujienos/ivykiu-kalendorius

ABBREVIATIONS

EIC	–	Extraction of injected charge carriers
BHJ	–	Bulk-heterojunction
OSC	–	Organic solar cell
PSC	–	Perovskite solar cell
P3HT	–	Poly(3-hexylthiophen-2,5-diyl) and [6,6]-phenyl-C61 butyric acid methyl ester
ETL	–	Electron transport layer
HTL	–	Hole transport layer
HTM	–	Hole transporting material
CT	–	Charge transfer
CTS	–	Charge transfer state
CTM	–	Charge transporting material
TOF	–	Time-of-flight
OPV	–	Organic photovoltaics
HOMO	–	Highest occupied molecular orbital
LUMO	–	Lowest unoccupied molecular orbital
PCE	–	Power conversion efficiency
oDCB	–	1,2-dichlorobenzene
CB	–	Chlorobenzene
DIO	–	1,8-diiodooctane
NGR	–	Non-geminate-recombination
CE	–	charge extraction
TRCE	–	Time-resolved charge extraction
TAS	–	Transient absorption spectroscopy
TPV	–	Transient photovoltage
TPC	–	Transient photocurrent
CELIV	–	Charge extraction by linearly increasing voltage
TDCF	–	Time-delayed collection field
FDM	–	Finite difference method
PESA	–	Photoelectron emission spectroscopy in air

TABLE OF CONTENTS

1. INTRODUCTION 10
1.1. Aim and objectives 13
1.2. Scientific novelty 14
1.3. Statements to defend 15
1.4. Publications related to dissertation 15
1.5. Conference presentations 16
1.6. Participation in scientific projects 16
1.7. Authors contributions 17
1.8. Dissertation layout 17
2. Literature review 19
2.1. Working principles of bulk-heterojunctions 19
2.2. P3HT:PCBM blend system 21
2.2.1. Thermal annealing and morphological optimization 22
2.2.2. Solvent annealing techniques 23
2.2.3. Influence of additives: The role of 1,8-Diiodooctane (DIO) …. 23
2.3. OSC degradation and thermal equilibrium 26
2.3.1. Intrinsic degradation 26
2.3.2. Extrinsic degradation 26
2.3.3. Strategies to improve stability in OSCs 27
2.3.4. Encapsulation techniques 28
2.4. Recombination of charge carriers in donor:acceptor systems 29
2.4.1. Non-geminate recombination (NGR) 30
2.4.2. Reduced Langevin recombination and its origins 31
2.4.3. Energy disorder, trap states and charge transfer states 34
2.4.4. Super second order recombination 40
2.4.5. Limitations of the Bimolecular recombination parameter .. 41

2.4.6. Charge carrier dependent recombination rate measurements …. 42
3. Investigation techniques 46
3.1. Time-of-flight (TOF) technique 46
3.2. Extraction of injected charge carriers (EIC) 53
3.3. Investigation of charge carrier transport using finite difference method (FDM) 54
4. Results and discussion 57
4.1. Investigation of recombination processes in P3HT:PCBM bulk heterojunction device by extraction of injected charge carriers 57
4.2. Cross-linkable fluorene-based hole transporting materials 63
4.2.1. Disorder and charge transport in fluorene-based cross-linked hole transporting materials 66
4.3. Fluorene-based bipolar charge transporting materials with balanced charge mobility 74
4.3.1. Charge transport and recombination in fluorene-based bipolar charge transporting materials 76
CONCLUSIONS 84
SANTRAUKA 85
1. Įvadas 85
1.1. Darbo tikslas ir uždaviniai 88
1.2. Mokslinis naujumas 88
1.3. Ginamieji teiginiai 89
1.4. Autoriaus indėlis 90
2. Literatūros apžvalga 91
3. Metodikos 93
3.1. Lėkio trukmės metodas (TOF) 93
3.2. Injektuotų krūvininkų ekstrakcijos metodas (EIC) 95
3.3. Baigtinių skirtumų metodas (FDM) krūvio pernašai ir rekombinacijai tirti 95
4. Rezultatai ir jų aptarimas 97

4.1. Rekombinacinių procesų tyrimas P3HT:PCBM tūrinėje heterosandūroje, pasinaudojant injektuotų krūvinikų ekstrakcijos metodu … 97

4.2. Skersaryšinamos fluoreno pagrindo skylių pernašos medžiagos … 99

4.2.1 Krūvininkų pernaša ir netvarka fluoreno pagrindo skersaryšinamose skylių pernašos medžiagose 101

4.3. Subalansuoto judrio bipolinės fluoreno pagrindo krūvio pernašos medžiagos 105

4.3.1. Krūvio pernaša ir rekombinacija bipoliniuose fluoreno pagrindo dariniuose 106

IŠVADOS 112

REFERENCES 114

APPENDIX I 123

APPENDIX II 125

APPENDIX III 126

APPENDIX IV 128

AKNOWLEDGMENTS

First and foremost, I extend my heartfelt gratitude to Kristijonas Genevičius for his unwavering support and extraordinary patience while guiding me through this dissertation, even at times when patience was undoubtedly wearing thin. Special thanks go to Vygintas Jankauskas for generously sharing his extensive expertise, making challenging tasks seem manageable. To Jonas Nekrasovas, I'm sincerely grateful for his valuable insights, and to Egidijus Kamarauskas, who enthusiastically encouraged me to pursue doctoral studies – despite knowing exactly what he was getting me into. A shout-out to Liudas Tumonis, who made absolutely no contribution to this dissertation but reliably kept the mood light with an endless stream of jokes. I'm equally thankful to my other colleagues for their advice, collaboration, and moral support throughout this journey.

Special gratitude to Adelė, whose evening interruptions demonstrated that no dissertation is more important than immediate attention to absolutely anything else.

Finally, sincere thanks to my family and all my friends, especially Paulius Gaigalas, who provided support, shared their experiences, and reminded me regularly that dissertations eventually do end. Your presence made this experience significantly less lonely and infinitely more enjoyable.

1. INTRODUCTION

In recent years the development of cheap and efficient photovoltaic devices has been associated with organic and hybrid structures[1]. They have shown tremendous potential as alternatives to their inorganic counterparts, with devices that are low-cost, lightweight, easily processed and with a low environmental footprint[2–5]. Remarkable progress has been made in developing high-performance active layer materials, electrodes, interlayers, and innovative device structures within the OSC field. Notably, advancements in active layer materials, particularly the creation of novel acceptors and donors, have substantially enhanced the power conversion efficiency (PCE) of OSCs.
The first generation of organic solar cells had a single active layer between two electrodes with different work functions. These devices had poor power conversion efficiency (PCE) below 0.1 % due to inefficient exciton (electron-hole pair) dissociation and significant recombination. In 1986, Tang introduced a bilayer heterojunction structure with donor and acceptor materials[6], achieving a PCE of around 1%. However, the limited donor/acceptor interface hindered efficient exciton diffusion and separation.
In 1995, Yu et al. proposed bulk heterojunction (BHJ) OSCs, where the donor and acceptor materials are mixed in the active layer[7]. This BHJ structure enhanced the donor/acceptor interface and reduced the diffusion distance for exciton separation, significantly improving device performance. Since its inception, the PCE of OSCs has soared to over 18%[8], establishing it as a promising photovoltaic technology.
The performance of OSCs is intricately tied to their morphology – the arrangement and distribution of materials within the active layer. Understanding and controlling this morphology is crucial for optimizing device efficiency, stability, and overall performance. Ideal morphology should facilitate efficient charge separation at the donor-acceptor interface and provide continuous pathways for charge transport to the electrodes while minimizing recombination losses. The processing conditions used to fabricate BHJs, such as solvent choice, annealing temperature, and deposition methods, have profound impact on the morphology[9–12]. In simpler systems, these conditions could be optimized relatively easily through combination of trial-and-error and guided experimentation. However, in complex multi-component systems, the processing window becomes narrower, and the interplay between different components makes it harder to predict the outcome.
Initially, OSCs were dominated by binary blends of donor and acceptor materials such as P3HT (polymer donor) and PCBM (a fullerene acceptor)[13].

The challenges of morphology control were already significant. Nevertheless, morphology of the simple systems could be reasonably well-characterized using techniques like transmission electron microscopy (TEM)[14,15], atomic force microscopy (AFM)[16], and X-ray diffraction (XRD)[17]. These methods allowed researchers to study phase separation, crystallinity, and domain purity, providing insights into how processing conditions influenced device performance.

However, the pursuit of higher efficiencies has driven the development of ternary[18] and quaternary[19] systems, which include additional donor or acceptor components. The ternary OSC strategy enhanced the absorption coverage by using multiple materials with different bandgaps while preserving processing simplicity of binary devices[20]. Additionally, adding a third component can create energy cascade effect, enhancing charge transfer and reducing recombination[21]. While these multicomponent systems offer performance benefits, they also introduce a greater degree of complexity in the morphology, as it now involves interactions between more than two materials, each with its own crystallization tendencies, miscibility, and phase separation behavior. Understanding how these materials interact on the nanoscale requires more sophisticated characterization techniques and theoretical models. For example, TEM and AFM provide high-resolution images of surface morphology[22], but they often are limited in their ability to probe the internal structure of thick films. Techniques like X-ray scattering, such as grazing incidence wide-angle X-ray scattering (GIWAXS), have become crucial for studying crystallinity and phase behavior of these complex systems[23,24]. However, interpreting the data from these techniques requires advanced models and simulations, as the scattering patterns become more intricate with increased material complexity.

Moreover, multi-component systems often exhibit mixed-phase morphologies where different components form interpenetrating networks. This leads to difficulties in distinguishing between the phases using conventional imaging techniques. Advanced methods like resonant soft X-ray scattering (RSoXS) and electron tomography have been developed to address these challenges[25], but they require specialized equipment and expertise, making them less accessible.

Additionally, the dynamic nature of morphology in OSCs adds another layer of complexity. During operation, OSCs can undergo morphological changes due to factors like light exposure, thermal stress, and mechanical deformation. Studying these dynamic changes requires in-situ characterization techniques, such as in-situ GIWAXS or in-situ AFM, which can monitor morphological evolution in real-time[26,27]. However, these techniques are still in their early

stages of development and often provide limited temporal and spatial resolution.

The introduction of such complex morphology has led to a complicated dynamic of charge carrier transport and recombination in blends with multiple donor-acceptor interfaces, diverse energy levels, and varying material properties. The presence of multiple donors and acceptors increases the number of potential recombination pathways. Identifying and quantifying these different mechanisms is challenging, particularly when they occur on different timescales and at different locations within the layer.

Even in simple binary blends recombination kinetics are often non-trivial, involving multiple time constants and dependencies on factors such as charge carrier density, temperature, and electric field[28,29]. Such complexity makes it difficult to extract meaningful kinetic parameters, such as recombination coefficients or charge carrier lifetimes, from experimental data.

Another major problem that adds to the complexity of development and characterization of OSCs is their degradation[30–32]. Over time, especially under operational conditions such as elevated temperatures, exposure to light, and electrical bias, the materials in the active layer tend to migrate towards a more thermodynamically stable state. As the system approaches thermal equilibrium, the free energy of mixing may favor the demixing of the donor and acceptor phases into larger, more distinct domains. Initially small, well-distributed donor and acceptor domains can grow larger as the materials migrate to reduce their interfacial energy. This growth is often accompanied by a reduction in the interfacial area between the donor and acceptor, leading to less effective charge separation. As phase separation progresses, the once-interconnected network of donor and acceptor materials may break down. This disruption can lead to the loss of continuous pathways for charge transport. This morphological evolution eventually reduces efficiency of charge separation and transport, increases recombination, and ultimately reduces the overall performance of OSC. An emerging idea of cross-linkable charge transporting materials, could stabilize the morphology and enable self-encapsulating architecture (for protection from oxygen and moisture), solving multiple degradation problems.

Apart from the aforementioned issues, OSCs typically consist of multiple layers, including the active layer, electron transport layer (ETL), hole transport layer (HTL), and electrodes, where each layer must be carefully engineered to optimize charge extraction and minimize losses. The interfaces between these layers are particularly critical, as defects or interlayer mixing can lead to significant performance degradation. The complexity of these multilayered structures increases the difficulty of device fabrication and the

likelihood of defects, which can affect yield and reliability. Incorporation of novel bipolar charge transporting materials into these multilayered devices and/or directly into BHJ would eliminate some complexity from the structure and solve the energetic level compatibility issue.
The complexity of OSCs translates directly into higher R&D costs. The need for sophisticated equipment, advanced materials, and extensive testing increases the financial investment required to develop commercially viable OSCs. For companies and investors, the high upfront costs and uncertain returns can be a significant deterrent.
Understanding and mitigating problems like phase separation, complex morphology and expensive investigation methods through new and cheap material design, processing strategies and novel investigation techniques is critical for sparking a new momentum in their development and commercialization.

1.1. Aim and objectives

The focus of this dissertation encompasses several research areas within the development of organic solar cells (OSCs), ranging from charge transport and recombination processes and their characterization methods to blend morphology and its stabilization. It addresses the enhancement of established methods for analyzing charge carrier recombination in OSCs, particularly aiming to establish the dependency of recombination rates on charge carrier concentration and the influence of processing additives. Additionally, this work delves into the development of cross-linkable hole-transporting materials (HTMs), which are designed to serve dual roles: as insulating layers for the active layer and as matrices for donor-acceptor blends, thereby helping to prevent morphological degradation over time. Furthermore, the thesis investigates novel fluorene-core bipolar charge-transporting materials, which can exhibit balanced hole and electron mobilities. These materials hold potential for use in organic photovoltaic devices, donor-acceptor blends to enhance overall device performance by optimizing charge transport. To achieve the objectives of this research, the following tasks were undertaken:

- Establish the recombination rate dependency on carrier concentration in poly(3-hexylthiophen-2,5-diyl) and [6,6]-phenyl-C61 butyric acid methyl ester (P3HT) bulk heterojunctions using a combination of numerical calculations, the extraction of injected charge carriers technique, and the time-of-flight method.
- Determine the recombination rate dependency on the layer thickness of P3HT:PCBM bulk heterojunctions, with and without the addition of 1,8-

diiodooctane (DIO), using numerical calculations, the extraction of injected charge carriers technique, and the time-of-flight method.

- Investigate the effects of cross-linking on charge transport, as well as spatial and energetic disorder parameters, in newly developed fluorene-core hole-transporting materials (HTMs).
- Characterize the performance and properties of new fluorene-based bipolar charge-transporting materials, with a focus on their potential application in improving the efficiency and stability of organic solar cells.

1.2. Scientific novelty

- Utilization of the extraction of injected charge carriers (EIC) method alongside time-of-flight (TOF) technique to quantitatively assess the recombination rate dependency on carrier concentration and BHJ thickness was done for the first time. This combination helped to uniquely identify a two-component dependency of recombination rates on carrier concentration, governed by interfacial states between two pure phases, and demonstrates how DIO-induced morphological changes lead to variations in recombination rates as the device thickness increases. EIC technique enabled a nuanced understanding of recombination dynamics, particularly in thicker samples where DIO appears to enhance recombination losses, provides significant insights into optimizing BHJ solar cell performance by manipulating processing conditions and morphological control, making it a novel contribution to the field of organic photovoltaics.
- Novel cross-linkable HTMs containing vinyl groups that enable thermal polymerization at temperatures above 200°C. It was established that cross-linking process has negligible effects on their energy levels and electrical properties. This addresses a critical challenge in OSC technology: the need for HTMs that not only offer high efficiency but also contribute to the long-term stability of the solar cells.
- The characterization of novel fluorene-based bipolar charge-transporting materials reveals their air stability and solution processability—both critical for practical applications in organic electronic devices. These materials are distinguished by their balanced hole and electron transport, achieved through the integration of electron-transporting anthraquinone, 9-fluorenone, and 9-dicyanofluorenylidene groups with carbazolyl electron-donating moieties. Unlike many bipolar CTMs, that require complex synthesis and expensive starting materials, these new compounds are synthesized through relatively straightforward methods, making them both innovative and practical.

1.3. Statements to defend

- The EIC technique can effectively identify the dependency of recombination velocities on carrier concentrations in P3HT:PCBM bulk-heterojunction devices, providing a detailed understanding of charge recombination dynamics in organic solar cells.
- Filling of interfacial states in P3HT:PCBM bulk-heterojunctions can be probed with EIC technique by analyzing the dependence of recombination velocity on carrier concentration.
- The EIC technique can reveal how 1,8-diiodooctane additive-induced morphological changes in P3HT:PCBM blend lead to variations in recombination rates as the device thickness increases.
- Vinyl cross-linking of fluorene-core HTMs boosts thermal and morphological stability while introducing only minor changes in electronic properties.
- Stable amorphous fluorene-based bipolar charge-transporting materials with anthraquinone and 9-fluorenone electron-transporting moieties exhibit balanced hole and electron mobilities. This balance is crucial for optimizing the performance of organic electronic devices, particularly in ensuring efficient charge transport.

1.4. Publications related to dissertation

1. Romualdas J. Čepas, Gytis Juška, Lukas Kukulas, Egidijus Kamarauskas, Kristijonas Genevičius. "Investigation of recombination processes in bulk-heterojunction solar cell by extraction of injected charge carriers", *Thin Solid Films*, Volume 752 (2022), 139254. DOI: https://doi.org/10.1016/j.tsf.2022.139254
2. Egidijus Kamarauskas, Aistė Jegorovė, Romualdas J. Čepas, Šarunė Daškevičiūtė-Gegužienė, Kristijonas Genevičius, Marius Franckevičius, Martynas Talaikis, Rokas Dobužinskas, Florian Scheler, Kari Sveinbjornsson, Vygintas Jankauskas, Vytautas Getautis. "Cross-linkable fluorene-based hole transporting materials for perovskite solar cells". *Chemical physics*, Volume 579 (2024), 112183. DOI: https://doi.org/10.1016/j.chemphys.2024.112183.
3. Aistė Jegorovė, Marytė Daškevičienė, Kristina Kantminienė, Vygintas Jankauskas, Romualdas J. Čepas, Alytis Gruodis, Vytautas Getautis, Kristijonas Genevičius. "New fluorene-based bipolar charge

transporting materials". *RSC Advances*, 2024, 14, 2975-2982. DOI: https://doi.org/10.1039/D3RA07583D

1.5. Conference presentations

1. Romualdas Jonas Čepas, Lukas Kukulas, Gytis Juška, Kristijonas Genevičius "Recombination of charge carriers in bulk heterojunction solar cells" *OPEN READINGS 2021.*
2. Romualdas Jonas Čepas, Lukas Kukulas, Gytis Juška, Kristijonas Genevičius. "Determination of dominant recombination processes by extraction of injected charge carriers" *Advanced Materials and Technologies 2021.*
3. Romualdas Jonas Čepas, Kristijonas Genevičius. "Investigation of temperature dependent recombination in small molecule charge transporting materials". *E-MRS 2021 Fall Meeting*.
4. Romualdas Jonas Čepas, Kristijonas Genevičius, Vygintas Jankauskas, Egidijus Kamarauskas. "Investigation of cross-linkable hole transporting material as a donor in binary and ternary bulk heterojunction". *E-MRS 2023 Spring Meeting*.
5. Romualdas Jonas Čepas, Egidijus Kamarauskas, Kristijonas Genevičius, Vygintas Jankauskas, Aistė Jegorovė, Šarūnė Daskevičiūtė-Gegužienė, Vytautas Getautis. "Cross-linkable fluorene-based hole transporting materials for perovskite solar cells". *Lietuvos Nacionalinė Fizikos Konferencija 45*.
6. Romualdas Jonas Čepas, Marytė Daškevičienė, Kristina Kantminienė, Vygintas Jankauskas, Aistė Jegorovė, Alytis Gruodis, Vytautas Getautis, Kristijonas Genevičius. "Investigation of novel fluorene-based bipolar charge transporting materials". *International Symposium on Flexible Organic Electronics 2024*.

1.6. Participation in scientific projects

Research Council of Lithuania: **Development of cross-linkable structures for solar cells** (Grant No. S-MIP-22-8). Prof. V. Jankauskas. 2022–2025. New cross-linkable hole transporting materials with fluorene, carbazole or triphenylamine derivatives and electron transport naphthalene or perylene derivatives with reactive styrene groups were investigated. Author contributed by characterizing charge transport properties of newly synthesized compounds.

1.7. Authors contributions

The author conducted comprehensive charge carrier mobility measurements using the time-of-flight technique for both bulk-heterojunction blends and cross-linkable and bipolar charge transfer materials (CTMs). Additionally, the author performed extraction of injected charge carriers (EIC) measurements in tandem with FDM simulations to evaluate and interpret the charge transport dynamics within these materials. The author was responsible for preparing all experimental samples for EIC and TOF analysis, which involved preparing solutions and blends, spray-coating the TiO_2 blocking layer, drop-casting and spin-coating the active and interfacial layers, and depositing electrodes.
The author participated in discussions of the results and contributed to the preparation of related publications. Moreover, the author carried out the analysis of the measurements and wrote this dissertation, ensuring that all information obtained from external sources was properly referenced.
The V. Getautis group at Kaunas University of Technology synthesized cross-linkable hole-transporting and bipolar charge-transporting materials and supplied the corresponding TGA, DSC, Raman, and CV data.
K. Genevičius wrote and provided a code for FDM simulations, while also assisting in interpretation of the data.
A. Gruodis performed quantum chemistry simulations of the bipolar molecules as well as their dimers.

1.8. Dissertation layout

The dissertation is structured to provide a comprehensive exploration of both the known theoretical principles and experimental advancements in this field. This work is divided into three key chapters, each building on the previous to create a cohesive narrative.
The second chapter serves as a Literature Review, laying the foundational understanding necessary for the understanding of research. This chapter begins by introducing organic solar cells, with a particular focus on the principles of bulk heterojunction (BHJ) solar cells. It explores the crucial aspects of charge transport and the various recombination mechanisms that can occur within these systems. Detailed discussions are provided on geminate, non-geminate, trap-assisted recombination, and the multiple trap-release model, which are essential for understanding the efficiency limitations of organic photovoltaics. Additionally, this chapter delves into the importance of morphology control in donor-acceptor blends, a critical factor in optimizing device performance. The review also examines degradation and morphology

stabilization issues in BHJ blends, introducing recent developments in encapsulation techniques and the idea of self-encapsulating cross-linkable structures.

In the third and fourth chapters, the focus shifts to the Investigation techniques and Results, where original research is presented. This chapter introduces an innovative technique for the extraction of injected charge carriers, which is employed to evaluate carrier concentration-dependent recombination in P3HT:PCBM blends — a well-known material system in organic photovoltaics. Through this technique, the dissertation offers new insights into the recombination dynamics within these blends, providing valuable data that can inform the design of more efficient solar cells. The Results chapter also includes the characterization of novel cross-linked and bipolar charge transfer materials, showcasing their potential in improving device performance. The results from these experiments are discussed in detail, highlighting their significance in the context of the broader research field. Key outcomes of the research are summarized, with a discussion on how these findings contribute to the development of organic solar cells. The conclusion chapter reflects on the implications of the experimental work, emphasizing its potential impact on future research and technological advancements in organic photovoltaics.

The dissertation concludes with a Summary in Lithuanian, offering a concise overview of the entire research, encapsulating the objectives, methodologies, results, and conclusions in a manner accessible to a wider audience.

2. Literature review

2.1. Working principles of bulk-heterojunctions

Organic photovoltaics (OPVs) and inorganic photovoltaics both aim to convert light into electricity, but they do so through fundamentally different mechanisms and architectures. In inorganic semiconductors like silicon, absorbed photons generate free charge carriers (electrons and holes) directly due to the material's high dielectric constant, which effectively screens the Coulombic attraction between these charges. This allows for efficient charge separation and transport. In contrast, organic materials have a much lower dielectric constant (approximately 2–4), leading to the formation of tightly bound electron-hole pairs known as excitons. These excitons require additional energy to separate into free charges, so the process of separation of electron and hole is less efficient than in inorganic materials.

Another key difference lies in how these charge carriers move through the materials. In inorganic semiconductors, charge carriers travel through continuous conduction or valence bands (band transport). However, in organic semiconductors, the weak intermolecular forces and inherent disorder result in a hopping mechanism, where localized charge carriers jump from one molecule to another. This hopping transport is less efficient and contributes to higher recombination losses compared to band transport in inorganic materials.

The evolution of organic solar cell architectures reflects these unique challenges. Initially, organic solar cells were designed with a bilayer structure, featuring distinct layers of electron-donating (donor) and electron-accepting (acceptor) materials, similar to the p-n junctions in inorganic cells. This bilayer design, however, was limited by the short exciton diffusion length in organic materials, typically around 10 nm. To address this limitation, the architecture evolved into bulk heterojunction solar cells (**Fig. 1a**), where the donor and acceptor materials are intimately mixed, forming a nanoscale interpenetrating network. This BHJ architecture greatly increases the interfacial area between the donor and acceptor phases, enhancing the probability that an exciton will reach a donor-acceptor interface and dissociate into free charges before it can recombine.

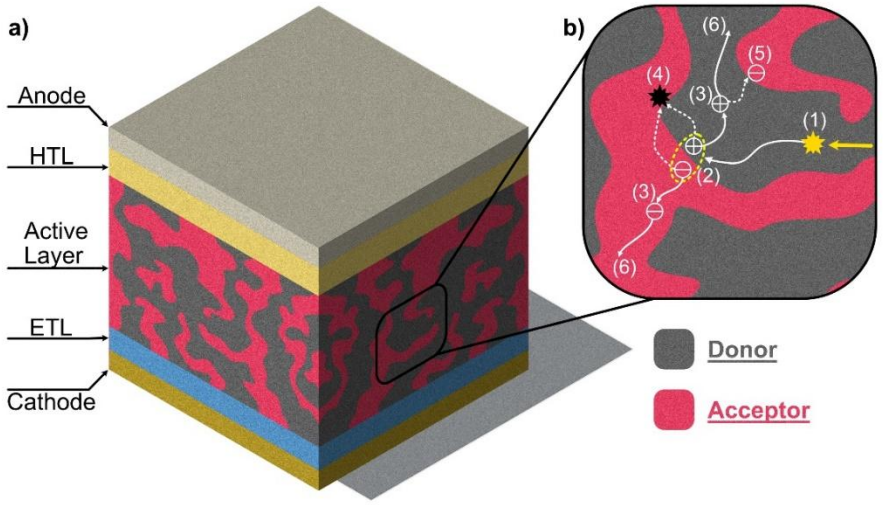

Fig 1. a) typical structure of bulk heterojunction organic solar cell (HTL – hole transporting layer, ETL – electron transporting layer), **b)** bulk-heterojunction under light illumination: (1) photon absorption, (2) exciton diffusion to the interface and charge transfer at the interface, (3) charge dissociation into free carriers or (4) geminate recombination (GR) at the interface. Non-geminate (NGR) recombination of free charge carriers (5) or (6) charge transport to corresponding electrodes.

In BHJ solar cells, the photovoltaic process involves several critical steps: photon absorption (**Fig. 1b** (1)), exciton diffusion to the donor-acceptor interface(**Fig. 1b** (2)), charge separation (**Fig. 1b** (3)), and charge transport to the electrodes (**Fig. 1b** (6)). The dissociated charges, driven by the internal electric field created by the asymmetry of the electrode work functions, then migrate towards their respective electrodes—holes through the donor material to the anode, and electrons through the acceptor material to the cathode.

Despite this intricate design, various loss mechanisms can reduce the overall power conversion efficiency (PCE) of OPV devices. One such mechanism is geminate recombination, where an exciton fails to separate and instead recombines at the donor-acceptor interface (**Fig. 1b** (4)). Even if excitons successfully dissociate, free carriers may still undergo nongeminate recombination, where they recombine with carriers from different excitons before reaching the electrodes (**Fig. 1b** (5)). This type of recombination can be bimolecular, involving free electrons and holes, or trap-assisted, where a trapped carrier recombines with a free carrier.

Several factors influence these recombination processes, including charge carrier mobility, phase separation, material purity, and the morphology of the

active layer. Bimolecular recombination, in particular, is often a dominant loss mechanism in efficient OPV systems. Interestingly, research has shown that this recombination can be reduced compared to the traditional Langevin description due to factors like spatial distribution of charge carriers, phase separation, and the possibility of carriers being re-released from localized trap states before recombining. These traps can play a significant role in shaping the kinetics of nongeminate recombination, impacting device performance even in systems with high efficiency.

In the following sections, we will focus on the well-established P3HT:PCBM blend system, which serves as a reference point in the study of bulk heterojunction organic solar cells. The documented behavior and performance of this system make it an ideal starting point for understanding key processes in BHJs, setting the stage for a more in-depth analysis of advanced multi-component systems.

2.2. P3HT:PCBM blend system

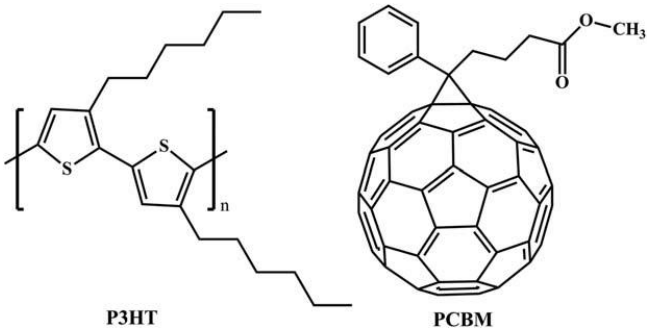

Fig. 2 Molecular structure of P3HT [poly(3-hexylthiophene)] (left) and PCBM [{6,6}-phenyl-C 61 -butyric acid methyl ester] (right).

The P3HT:PCBM blend system has become a benchmark in the field of organic photovoltaics (OPVs), largely due to the complementary properties of P3HT (poly(3-hexylthiophene)) and PCBM ([6,6]-Phenyl-C61-butyric acid methyl ester). This system leverages the high absorption coefficient and hole mobility of P3HT with the excellent electron accepting and transporting abilities of PCBM, resulting in a balanced and efficient photovoltaic material[33]. Early research into P3HT systems was significantly informed by studies on earlier materials, particularly PPV systems, which provided foundational insights into the optimization of organic solar cells[34].

The performance of P3HT solar cells is highly sensitive to the ratio of P3HT to PCBM in the blend. However, identifying a universally optimal ratio is

challenging due to inherent variability in polymer properties such as regio-regularity, polydispersity, and molecular weight, all of which can differ based on the batch and supplier. Additionally, the efficiency of these solar cells is also influenced by the thickness of the active layer, making a one-size-fits-all ratio impractical. Early studies on P3HT blends typically explored compositions with higher PCBM content, in the range of 1:2 to 1:3 (P3HT). For instance, Schilinsky et al. and Padinger et al. reported power conversion efficiencies (PCEs) of 2.8% and 3.5%, respectively, for such ratios[33,35]. However, subsequent research indicated that a more balanced composition, closer to a 1:1 ratio, tends to yield better performance. This consensus was supported by Chirvase et al., who found that the maximum PCE occurred with P3HT ratios between 1:1 and 1:0.9[36]. Huang et al. further confirmed the benefits of a 1:1 weight ratio using time-of-flight techniques, demonstrating that this ratio led to balanced electron and hole mobilities, which is attributed to a more ordered structure in the blend[37]. Li et al. and Reyes-Reyes et al. reported even higher PCEs of 4.4%[38] and 4.9%[39], respectively, at an optimal ratio of 1:0.8, highlighting the importance of fine-tuning the blend composition for achieving peak device performance.

2.2.1. Thermal annealing and morphological optimization

Thermal annealing has been a key technique for enhancing the PCEs of P3HT solar cells. The primary effect of annealing is the improvement of the film morphology, particularly through the increased crystallinity of P3HT and the enhanced mobility of charge carriers. Annealing typically occurs at temperatures between the glass transition temperature (approximately 120°C) and the melting point of P3HT (178°C), with most studies focusing on a range of 110°C to 160°C for durations of 1 to 30 minutes. Chirvase et al. studied the effects of annealing at 130°C, observing a red shift in the absorption spectrum of P3HT, which was more pronounced with longer annealing times. This shift, along with the emergence of a pronounced absorption shoulder around 620 nm, indicated enhanced interchain interactions and a higher degree of ordering in P3HT. Reyes-Reyes et al. demonstrated that devices annealed at 150°C for 5 minutes achieved a maximum short-circuit current (J_{sc}) of 11.1 mA/cm², attributed to improved film crystallinity.

Further insights were provided by Li et al., who compared the effects of annealing before and after cathode deposition. They found that annealing after cathode deposition yielded better PCE improvements, suggesting that the cathode may act as a barrier, hindering morphological changes during annealing. Atomic force microscopy (AFM) images of optimally annealed

films (110°C, 10 minutes) revealed a rougher texture, which likely enhances contact between the polymer and the cathode, facilitating better charge collection.
Erb et al. provided a more systematic analysis, correlating the crystallinity of P3HT:PCBM films with their optical properties. They concluded that annealing promotes the diffusion of isolated PCBM molecules into larger aggregates, allowing P3HT aggregates to crystallize in PCBM-free regions. This reorganization leads to better electron transport through PCBM clusters and improved light absorption by P3HT crystallites, both contributing to enhanced device performance. Building on this understanding, Ma et al. achieved a PCE of 5% by annealing P3HT devices at 150°C for 30 minutes.

2.2.2. Solvent annealing techniques

While thermal annealing is effective, its applicability to large-area and flexible solar cells is limited due to the need for elevated temperatures. As an alternative, room-temperature annealing, often referred to as "solvent annealing," has emerged as a viable method for controlling the growth and morphology of the active layer[40].
Solvent annealing involves exposing the solution-processed active layer to solvent vapor, which slows the evaporation rate of the solvent and allows for more controlled film formation. Li et al. demonstrated a 4.4% PCE in a P3HTcell using this method, with 1,2-dichlorobenzene (oDCB) as the solvent for spin-casting. The slower evaporation rate, due to oDCB's higher boiling point (compared to CB or chloroform), allowed for better polymer self-organization and higher degrees of ordering, leading to improved device performance[38].
Mihailetchi et al. further supported the effectiveness of solvent annealing by showing that hole mobility in slow-grown films improved by a factor of 33 compared to faster-grown films[41]. This significant increase in mobility underscores the importance of controlling film growth rates to optimize the morphology and performance of P3HT:PCBM solar cells.

2.2.3. Influence of additives: The role of 1,8-Diiodooctane (DIO)

Additives have become indispensable in optimizing the morphology and performance of P3HT:PCBM solar cells, with various options such as 1,8-octanedithiol, di(ethylene glycol) diethyl ether, N-methyl-2-pyrrolidinone, 1,8-dichlorooctane, 1,8-dibromooctane, and 1,8-diiodooctane[42] being used to control the morphology of bulk heterojunctions (BHJ). Among these, DIO has

emerged as one of the most effective additives due to its high boiling point, which plays a crucial role in fine-tuning the nanoscale morphology of the active layer. DIO primarily functions by decelerating the evaporation rate of the primary solvent during film formation, allowing for more controlled phase separation between P3HT and PCBM (**Fig. 3**). This leads to an optimized nanoscale morphology that is vital for the device's efficiency. DIO selectively interacts with PCBM, promoting the formation of smaller and more uniformly distributed PCBM domains within the P3HT matrix. Such improved distribution is critical for effective charge separation and transport, increasing the interfacial area between the donor and acceptor phases while maintaining well-connected pathways for charge carriers. However, the effects of additives like DIO are not yet fully understood, as they depend on the different solvents and polymer systems used, where the same additive can exhibit different effects. The varied properties of these additives, such as boiling points, solubility, and polarity, result in additional changes in the layer's morphology either before or after solvent evaporation, influencing polymer chain arrangement, domain dispersion, packing density, and size. Consequently, a significant enhancement in solar cell performance metrics can be achieved.

During the drying process, the presence of DIO also facilitates the formation of more ordered P3HT domains. This often results in an increased face-on orientation of P3HT chains relative to the substrate, which is particularly beneficial for hole transport. The alignment of the π-π stacking direction with the transport direction enhances charge mobility, contributing to the overall efficiency of the solar cell.

The incorporation of DIO into the processing of P3HT:PCBM solar cells has been shown to markedly improve key performance indicators, including power conversion efficiency (*PCE*), short-circuit current density (J_{sc}), and fill factor (*FF*). Research has demonstrated that the addition of DIO can lead to PCE improvements of 10-20% compared to devices processed without additives. This improvement is largely attributed to the optimized phase separation and enhanced crystallinity that DIO enables, which together result in more efficient charge generation, transport, and collection.

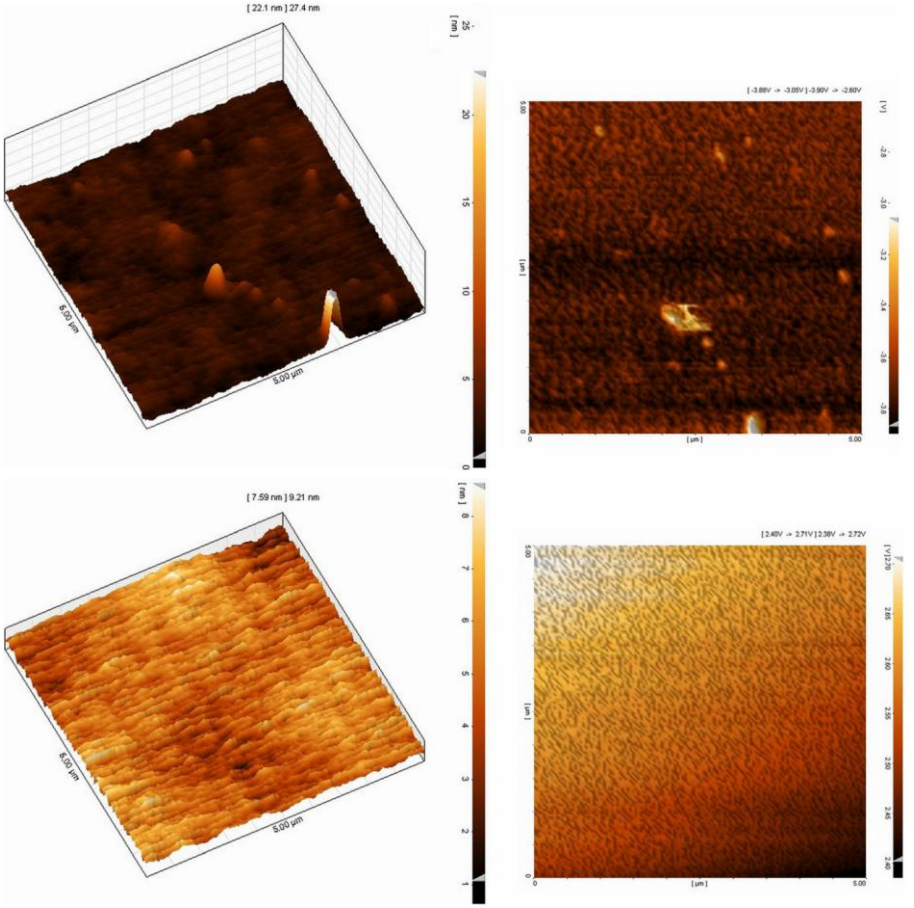

Fig. 3 AFM images of the sample with a 1:2 P3HT:PCBM ratio and a P3HT concentration of 10 mg/ml. Images without diiodooctane: topography (top left) and phase (top right). Images with 1% diiodooctane: topography (bottom left) and phase (bottom right).[43]

Despite the numerous advancements in optimizing P3HT solar cells, the average PCE across published studies hovers around 3.5%. This relatively modest efficiency, compared to newer materials and systems, highlights the inherent limitations of the P3HT system, such as limited absorption range, suboptimal charge carrier mobility, and the sensitivity of performance to processing conditions.

Nevertheless, the P3HT:PCBM blend system remains a critical reference point in OPV research due to its well-understood properties and the wealth of knowledge accumulated over years of study. Future improvements in organic photovoltaics will likely build upon the foundational understanding gained from this system, even as research shifts toward newer, more efficient material combinations.

2.3. OSC degradation and thermal equilibrium

The stability and degradation of BHJ OSCs remain significant barriers to their large-scale commercialization. Several degradation mechanisms can compromise the stability of these devices over time, which are broadly categorized into intrinsic and extrinsic factors.

2.3.1. Intrinsic degradation

Intrinsic degradation refers to the deterioration that occurs due to changes within the materials or at the interfaces between layers, independent of external environmental influences. The BHJ blend is only metastable. Given time and heat, the finely intermixed donor-acceptor network coarsens into larger domains that are no longer within an exciton-diffusion length. A classic example is the MDMO-PPV:PCBM system, whose morphology visibly coarsens after 16 h at 110 °C, with a simultaneous 50 % loss in short-circuit current (**Fig. 4**)[44].

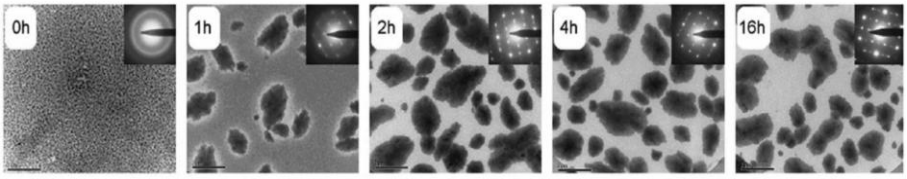

Fig. 4 Morphological changes induced in MDMO-PPV:PCBM layers after 16 hours of thermal annealing at 110 °C.[45]

Chemical change provides a second intrinsic route. Conjugated polymers and fullerene (or non-fullerene) acceptors can oxidise, dimerise or undergo chain scission under illumination and elevated temperature. Such reactions generate trap states that impede charge transport and lower the open-circuit voltage[46]. Interfaces are often even more delicate. The widely used hole-transport layer PEDOT:PSS is acidic and hygroscopic; over time it corrodes the underlying indium-tin-oxide (ITO) anode, and indium ions diffuse into the photoactive layer, creating recombination centres that depress the fill factor[47]. Thermal or mechanical stress can also trigger interlayer mixing or delamination, compounding the loss.

2.3.2. Extrinsic degradation

Extrinsic degradation is caused by external environmental factors such as oxygen, moisture, UV light, and temperature fluctuations. These factors can significantly affect the stability of OSCs:

Even the most inert stack is vulnerable once oxygen, moisture, or ultraviolet (UV) light breaches the encapsulant. Oxygen acts as an electron acceptor and forms super-oxide under illumination, while water accelerates hydrolysis and promotes delamination; together they create a synergistic degradation pathway that shortens device T_{80} lifetimes (denotes time when OSC efficiency drops to 80% of its initial value under ISOS protocols) by orders of magnitude[48].

Continuous exposure to solar UV further aggravates the problem. High-energy photons break π-bonds, generate reactive oxygen species, and initiate unwanted cross-linking or fragmentation of the photo-active molecules. Filtering wavelengths below $\approx 350\ nm$ has been shown to halve the initial "burn-in" PCE loss, underscoring the importance of photodegradation[49].

Finally, thermal stress, whether from daily temperature swings or self-heating under high irradiance—accelerates every intrinsic and extrinsic pathway. Recent work on high-performance blends shows that storage at 85 °C hastens domain coarsening, increases energetic disorder, and cuts T_{80} lifetimes ten-fold compared with operation at 45 °C[50].

2.3.3. Strategies to improve stability in OSCs

To improve the long-term stability and performance of bulk heterojunction (BHJ) organic solar cells (OSCs), researchers have explored several mitigation strategies. These efforts primarily focus on optimizing the device architecture, employing advanced encapsulation techniques, and precisely controlling the morphology of the BHJ layer[51].

Among these strategies, device architecture plays a pivotal role in determining both the initial efficiency and operational durability of OSCs. Two common architectural designs are employed: the non-inverted (or conventional) structure and the inverted structure, each with distinct advantages and limitations.

In the non-inverted architecture, the photoactive BHJ layer is positioned between a transparent anode—typically indium tin oxide (ITO)—and a low-work-function metal cathode, often aluminum. A hole transport layer (HTL), most commonly poly(3,4-ethylenedioxythiophene):poly(styrenesulfonate) - PEDOT:PSS, is applied on the ITO to facilitate hole collection. Despite its relatively high initial efficiency, this architecture is prone to degradation over time. The aluminum cathode is vulnerable to oxidation and moisture ingress[52], while the acidic and hygroscopic nature of PEDOT:PSS can lead to corrosion of the ITO layer. This corrosion promotes the diffusion of indium into the active layer, ultimately diminishing device performance [47].

In contrast, the inverted architecture rearranges the layer sequence to enhance device stability. In this configuration, a low-work-function metal oxide such as zinc oxide (ZnO) or titanium dioxide (TiO_2) serves as the electron transport layer (ETL) and is placed directly on the ITO substrate. The top electrode, instead of aluminum, is composed of more stable, high-work-function metals like silver or gold. This structural inversion improves stability by utilizing materials that are less sensitive to environmental factors. Metal oxides used in the ETL are more resistant to oxidation, and the use of inert top electrodes enhances resistance to air and moisture. Consequently, inverted OSCs tend to demonstrate longer operational lifespans and better resistance to environmental degradation compared to their conventional counterparts[53].

2.3.4. Encapsulation techniques

Encapsulation is the first line of defence against oxygen and water-vapour—the two external agents that most quickly corrode electrodes and disrupt the finely tuned nano-morphology of bulk-heterojunction organic solar cells. When barrier layers reduce the water-vapour-transmission rate (WVTR) below about 10^{-5} g m^{-2} day^{-1}, lifetimes that once measured days can stretch into the thousands-of-hours range under accelerated damp-heat testing, highlighting just how decisive an effective seal can be[54,55].

Rigid glass laminates remain the gold standard in laboratories because soda-lime or aluminosilicate glass blocks virtually all gas diffusion while adding no optical loss. Devices sealed between two glass panes with an epoxy edge-seal routinely show negligible decay during standardized testing protocols; the price is total incompatibility with bendable modules and roll-to-roll lines[54].

For flexible OSCs, the community has converged on protective ultrathin multilayer foils in which alternate nanometre-thick inorganic sheets—grown by atomic- or molecular-layer deposition—and compliant polymer interlayers force any diffusing molecule to follow a long, tortuous path. Modern Al_2O_3/organic stacks just 1 μm thick now reach WVTR values in the 10^{-5} g m^{-2} day^{-1} bracket while surviving tens of thousands of bending cycles without barrier failure[55].

A hybrid route combines the virtues of both worlds: an inorganic oxide provides the dense moisture barrier, and a conformal polymer overcoat heals nanocracks and lends mechanical toughness. Parylene-coated AlO_x laminates, for example, exhibit WVTRs near 3×10^{-4} g m^{-2} day^{-1} at 38 °C/90 % RH and preserve device efficiency after thousands of folding cycles, positioning them for wearable or foldable power sources[54,55].

An emerging idea is to let the hole-transport layer (HTL) itself double as the seal. Cross-linkable chemistries make this concept plausible:

- **Photo-crosslinked PEDOT:PSS**: inserting a bis-azide or glycidyl methacrylate agent into PEDOT:PSS followed by brief UV exposure converts the water-soluble polymer into a dense, water-resistant network. Devices built on the cross-linked film retain both efficiency and morphology after prolonged humidity exposure, showing that the HTL can now act as a thin barrier layer as well[56].
- **In-situ-grown AgO_x HTL**: a 3 μm-thick ultraflexible OSC recently achieved 89 % efficiency retention after four hours of immersion in water thanks to a silver-oxide HTL that is formed right at the electrode/active-layer interface; when over-coated with a 1 μm parylene film, the device survives machine-washing tests—a convincing demonstration that a chemically robust HTL can shoulder much of the waterproofing task[57].
- **Dynamic covalent crosslinkers in the active stack**: thioctic-acid additives that form disulfide networks "freeze" the BHJ morphology, raise the crack-onset strain by >70 %, and keep flexible devices above 96 % of their initial power after 5 000 bending cycles. Such *in situ* crosslinking suggests that mechanically integrated, self-healing barriers can be generated during normal coating steps[58].
- **Molecular six-bridge azide cross-linkers**: adding only 0.05 wt % of a high-efficiency azide cross-linker lifted OPV lifetime by 59 % at 85 °C (1680 h) without harming performance, because the additive immobilised acceptor molecules and suppressed diffusion pathways for oxygen and water[59].

Taken together, these results hint at a "self-encapsulating" architecture in which the HTL—or even the active layer—polymerises into a dense, solvent-resistant network that blocks moisture ingress while still providing favourable energy alignment. If such cross-linkable interfacial materials can be engineered to cure at low temperature, remain optically benign, and withstand further solution processing, they could simplify module fabrication by merging two layers into one and eliminate the need for separate foil laminates on ultrathin, wearable OSCs.

2.4. Recombination of charge carriers in donor:acceptor systems

To understand the operation of a photovoltaic (PV) device, two key processes must occur: (1) the photogeneration of free charge carriers and (2) the collection of these photogenerated carriers. In organic photovoltaics (OPVs),

the first process—converting absorbed photons into free charge carriers—is particularly challenging due to the strong Coulombic attraction between the photo-excited electron-hole pair, known as a geminate pair. For this pair to separate into free charges, the Coulomb binding energy must be overcome; otherwise, the pair will recombine in a process known as geminate recombination.

Geminate recombination occurs when an electron and hole, originating from the same photon, recombine before they can separate into free charges. This includes excitons that fail to reach an interface and relaxes to the ground state, as well as geminate pairs that recombine at the donor-acceptor (D/A) interface. At the D/A interface, the electron and hole form a charge transfer (CT) state, where the electron resides in the acceptor and the hole in the donor. The term "CT state" is commonly used to describe this scenario, although other terms like exciplex, bound polaron pair, and CT exciton are also found in the literature. Regardless of terminology, geminate recombination at the D/A interface is driven by the Coulombic attraction between the electron and hole. Importantly, geminate recombination is a monomolecular process, meaning that the likelihood of recombination for a given geminate pair is independent of the total density of pairs and scales linearly with the number of absorbed photons. This implies that the fraction of geminate pairs lost to recombination remains constant across different light intensities, and the photocurrent in systems dominated by geminate recombination scales linearly with light intensity. However, at very high light intensities, other recombination processes, such as exciton-exciton or exciton-charge annihilation, may also become significant.

In modern BHJ systems, the design of the donor-acceptor interface and the presence of bicontinuous interpenetrating network of donor and acceptor materials greatly enhance the probability of exciton dissociation into free charges. As a result, geminate recombination has become less of a concern compared to other recombination processes.

2.4.1.Non-geminate recombination (NGR)

Non-geminate recombination (NGR) refers to the process where free electrons and holes, generated from different excitons, encounter each other and recombine. This process is critical in BHJ solar cells because it directly competes with the charge extraction process, reducing the overall photocurrent. The term non-geminate recombination encompasses the recombination of any free charge carriers that do not originate from absorption of a single photon. In addition, photogenerated charge carriers, NGR may also

involve injected charge carriers. The recombination originating from these non-geminate charge carriers can be observed as three fundamentally different mechanisms: trap-assisted, bimolecular, and auger.

The most commonly observed NGR in OSC devices is that of bimolecular mechanism: the recombination of a free electron with a free hole. In a disordered semiconductor with localized charge carriers, bimolecular recombination is limited by the rate at which oppositely charged carriers find one another. The faster charge carriers move, the faster they will find each other; consequently, the rate of bimolecular recombination in OSCs is proportional to charge carrier mobilities. This is described by the Langevin expression following the relation,

$$R_L = \frac{e(\mu_n + \mu_p)}{\varepsilon\varepsilon_0}(n \cdot p - n_i^2) \tag{2.1}$$

Where e is the elementary charge, ε the dielectric constant, μ_n the mobility of the electrons through the LUMO of the acceptor, μ_p the mobility of the holes through the HOMO of the donor, n and p represent the electron and hole charge density respectively and n_i is the intrinsic carrier concentration. This relationship underscores how both material properties – mobility and dielectric constant – play a crucial role in determining recombination rates.

In organic semiconductors, the Langevin recombination mechanism is particularly significant due to the intrinsic material properties. Organic materials typically have low charge carrier mobilities and low dielectric constants (around 3-4). These characteristics lead to relatively high Langevin recombination rates, making it a dominant recombination mechanism in many organic photovoltaic devices.

While Langevin theory provides a fundamental understanding of how electrons and holes recombine, real-world organic semiconductor systems often exhibit deviations from the ideal Langevin behavior.

2.4.2. Reduced Langevin recombination and its origins

While the presence of Langevin recombination has been satisfyingly confirmed in many organic semiconductors, the strength of this coefficient in OSC devices is often found to be less than that predicted by the Langevin expression[60]. This has lead to the addition of another term, r, commonly referred to as the Langevin-reduction factor in expressions for the net bimolecular recombination rate, R_{BL}.

$$R_{BL} = r \cdot R_L \tag{2.2}$$

Most polymer:fullerene BHJ systems studied to date seem to have r between 0.01 and 1, with some reports for the P3HT:PCBM system finding r as low as 10^{-4}.

There are several strategies that can be employed to achieve reduced recombination rate and consequently increase the OSC efficiency.

Morphology optimization

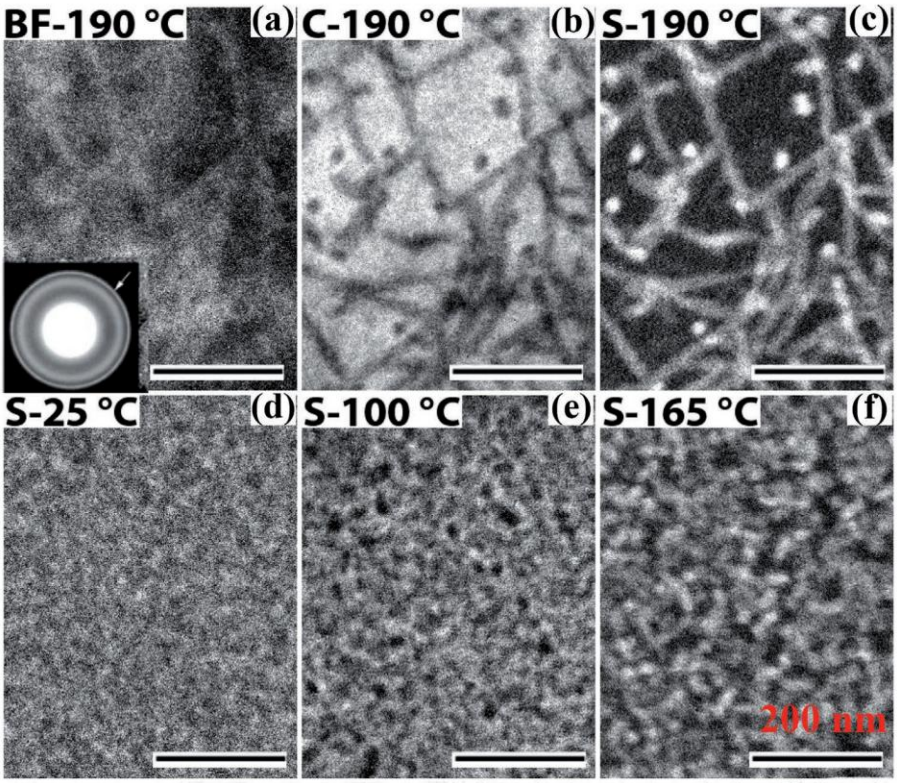

Fig. 5 Top: bright-field (BF), carbon (C), and sulfur (S) maps for a 1:1 P3HT:PC_{61}BM film annealed for 30 min. The same region of the sample is shown, and images were taken at zero defocus. Bottom: sulfur maps of 1:1 P3HT:PC61BM films annealed at 25, 100, and 165 °C. The image intensities of the sulfur maps are proportional to the sulfur concentration, and the light regions correspond to P3HT-rich domains. Films annealed at high temperatures, such as 190 °C, exhibit the presence of P3HT fibers in a PC61BM-rich matrix. The scale bar represents 200 nm.[61]

By optimizing the phase separation between donor and acceptor materials, continuous pathways for charge carriers can be established, facilitating efficient charge transport and reducing the likelihood of recombination.

- **Nanoscale Phase Separation**: Ensuring that the donor and acceptor materials phase-separate at the nanoscale can significantly reduce Langevin recombination. An ideal morphology would consist of well-connected domains for both electrons and holes, which minimizes the time these charge carriers spend in the active layer, thereby reducing their chance of recombination.
- **Crystallinity and Domain Purity**: Enhancing the crystallinity of the donor and acceptor phases improves charge carrier mobility, which further reduces recombination rates. High-purity domains with fewer defects also contribute to lower recombination rates. Techniques such as solvent and thermal annealing are commonly employed to achieve increased crystallinity and domain purity. As shown in **Fig. 5**, EF-TEM bright-field images demonstrate that polymer crystallization is a driving force in the structure formation process within miscible polythiophene/fullerene mixtures. In as-cast films, there is minimal structure. However, annealing enhances molecular motion, allowing polythiophene to precipitate as a crystalline pure phase while rejecting PCBM to the amorphous mixed phase. Consequently, polymer crystallization increases the concentration of PCBM in the amorphous phase and can lead to macroscopic phase separation if sufficient polymer crystallization occurs.

Charge carrier mobility

Upon examining the Langevin recombination expression, it may initially be assumed that materials with higher charge carrier mobility would lead to increased recombination rates in bulk heterojunction (BHJ) organic solar cells (OSCs). This assumption stems from the fact that the Langevin recombination rate is directly proportional to the sum of the electron and hole mobilities. However, both experimental studies and simulations have demonstrated that, paradoxically, the bimolecular recombination rate in OSC devices tends to decrease as mobility increases.

This seemingly counterintuitive phenomenon can be attributed to the improved efficiency of charge extraction in higher mobility materials, which leads to a reduction in charge carrier density within the active layer. Lower carrier density, in turn, reduces the likelihood of non-geminate (bimolecular) recombination, despite the increased mobility. In contrast, when the mobility is too low, inefficient extraction of photogenerated charges causes the carrier

density to rise, thereby enhancing the probability of non-geminate recombination.

Enhancing charge carrier mobility reduces Langevin recombination by decreasing the time carriers spend within the active layer, consequently limiting their exposure to recombination events. Several strategies can be employed to improve mobility:

First, the use of materials with inherently high charge carrier mobilities, such as certain conjugated polymers and small molecules, can significantly reduce recombination losses. For instance, high-mobility polymers like PffBT4T-C_9C_{13}, recognized for its superior hole mobility, have been shown to enhance the performance of OSCs by enabling more rapid charge transport and more efficient charge extraction[62].

Second, achieving optimal molecular alignment within the donor and acceptor materials can create more efficient charge transport pathways, further mitigating recombination. This molecular alignment can be achieved through specific design strategies, such as the incorporation of side chains that promote planarization and efficient π-π stacking.

Both electron and hole mobilities are crucial in this process, and an imbalance between them can lead to the development of space charge. In such cases, one type of charge carrier, either electrons or holes, may be extracted more efficiently than the other, resulting in the accumulation of the slower carrier. This accumulation generates an internal electric field that opposes the extraction of the remaining charge carriers, thereby exacerbating recombination losses.

Thus, optimizing the performance of OSCs requires careful balancing of electron and hole mobilities, ensuring that both charge carriers are extracted at comparable rates. Achieving this balance is critical for minimizing space charge effects, reducing recombination losses, and enhancing the overall efficiency of organic solar cells.

2.4.3. Energy disorder, trap states and charge transfer states

Organic semiconductors present a unique set of challenges and opportunities due to the inherent energy disorder within their active layers. Unlike crystalline semiconductors, where charge transport occurs in a highly ordered and predictable manner, organic materials are characterized by a significant degree of structural and energetic disorder. This disorder influences the behavior of charge carriers—electrons and holes—particularly in relation to charge transport, recombination dynamics, and the overall efficiency of the

device[60]. Understanding and controlling these factors is paramount to optimizing OSC performance.

Energy disorder in organic semiconductors arises from the amorphous nature of organic materials, where variations in molecular packing and electronic structure result in a broad distribution of energy states[63]. These variations introduce localized potential minima and maxima, creating a landscape that charge carriers must travel. While this disorder might initially appear detrimental, it can, under certain conditions, actually reduce the rate of bimolecular recombination by promoting spatial separation between charge carriers.

The extent to which disorder mitigates recombination is often expressed in terms of the recombination radius, r_c, which denotes the critical distance within which an electron and hole can recombine under the influence of Coulombic attraction. In an ideal system without disorder, this radius is determined by the equation:

$$r_c = \frac{e^2}{4\pi\varepsilon\varepsilon_0 k_B T}$$

where e is the elementary charge, is ε the relative permittivity of the material, ε_0 is the permittivity of free space, k_B is the Boltzmann constant, and T is the temperature. This equation encapsulates the balance between thermal energy and electrostatic attraction, dictating the spatial scale at which recombination occurs.

In disordered organic semiconductors, the energy landscape can effectively extend r_c by introducing energetic barriers and spatially separating the pathways of electrons and holes[64]. As a result, the probability of recombination is reduced, particularly over shorter distances, since carriers must overcome both spatial and energetic obstacles to recombine. This separation enhances charge extraction by allowing more time for charge carriers to reach the electrodes before they encounter one another and recombine.

In addition to energy disorder, trap states in organic semiconductors play a significant role in charge transport and recombination. These trap states represent localized energy levels where charge carriers can become temporarily immobilized. Trap states arise from structural defects, impurities, or variations in molecular packing and can capture either electrons or holes, reducing their mobility.

At first glance, trap states seem inherently detrimental, as they slow charge transport and increase the likelihood of recombination[65]. However, under certain conditions, trap states can mitigate recombination by lowering the free

carrier density. This phenomenon is encapsulated in what is termed trap-assisted recombination, which results in non-Langevin behavior, where the recombination rate is slower than predicted by conventional Langevin theory. The presence of trap states can lead to a reduction in bimolecular recombination by reducing the concentration of free charge carriers. This reduction is critical because recombination is a bimolecular process, which scales with the product of electron and hole densities. Trap states, by capturing carriers and reducing their immediate availability, slow the recombination process and provide an opportunity for trapped carriers to be released and successfully extracted over time.

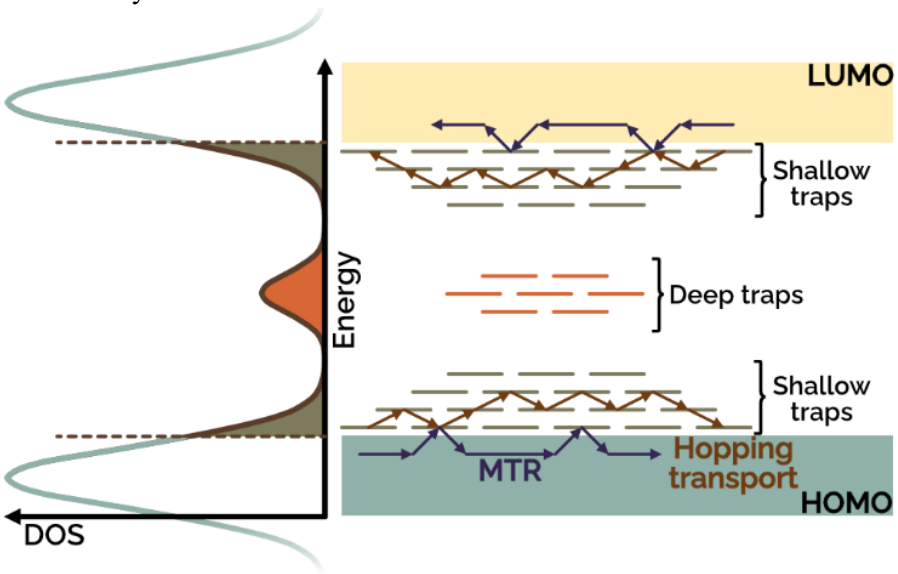

Fig. 6 (Left) The density of states (DOS) function illustrates shallow traps originating from tail states and deep traps within the bandgap. (Right) A conceptual energy diagram of an organic semiconductor (OSC), depicting localized trap states in the bandgap. The diagram shows the different charge transport mechanisms: multiple trapping and release (MTR, blue arrows), and thermally-activated hopping transport between localized states.

The Multiple Trapping and Release (MTR) model is particularly useful in describing this process[63]. According to the MTR model, charge carriers are temporarily immobilized in traps but can be thermally re-excited and released into higher energy states where they continue to contribute to charge transport. The release rate depends on the depth of the trap and the temperature of the material, with shallow traps allowing for more frequent release. This dynamic interaction between trapping and release plays a crucial role in lowering recombination rates while maintaining efficient charge transport.

Another key factor influencing recombination in OSCs is the formation of charge transfer (CT) states at the donor-acceptor interface[66]. When excitons (bound electron-hole pairs) are generated upon photon absorption, they must dissociate into free charges to contribute to the photocurrent. However, at the donor-acceptor interface, excitons first form CT states, where the electron and hole are partially separated but still experience Coulombic attraction.

The stability and lifetime of CT states are critical in determining whether charge recombination or extraction will dominate. If CT states persist for too long without dissociating into free charges, they increase the likelihood of recombination, as the electron and hole remain in close proximity. However, if the CT states are sufficiently long-lived without being overly stable, the spatial separation of the electron and hole reduces the overlap of their wavefunctions, decreasing the recombination probability.

A balance must be struck in designing materials where CT states are neither too stable nor too short-lived. If CT states dissociate too quickly, charge carriers may recombine before being efficiently extracted. Conversely, if CT states are too stable, they can act as bottlenecks, impeding charge transport and limiting overall device efficiency.

The performance of OSCs is governed by the intricate interplay between energy disorder, trap states, and CT states. Energy disorder, by creating a broad distribution of energy levels, can reduce recombination by spatially separating charge carriers and extending the effective recombination radius.

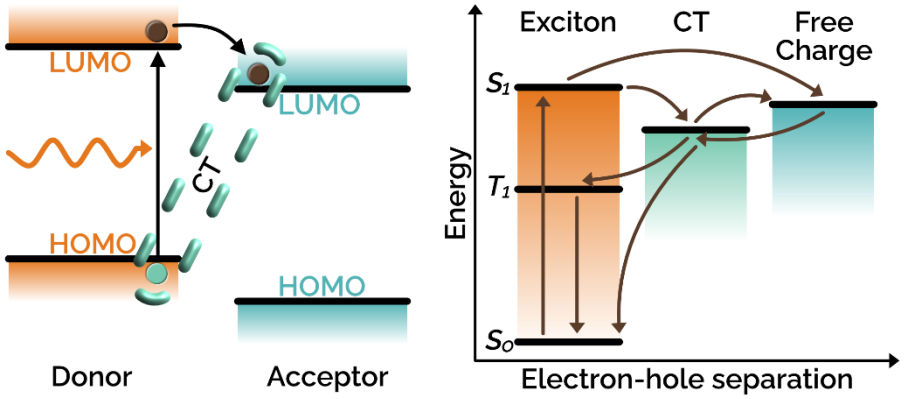

Fig. 7 Illustration of charge separation process in a donor-acceptor system.

Upon photon absorption, an electron is excited from the donor's HOMO to its LUMO, forming an exciton. The exciton moves to the donor-acceptor interface, where charge transfer (CT) occurs, separating the electron and hole between the LUMOs of the donor and acceptor. The right panel shows the energy levels involved: exciton formation in the singlet state (S_1), followed by

transitions to a charge-transfer state and eventual dissociation into free charge carriers. Relaxation pathways via recombination or triplet state formation (T_1) are also shown.

At the donor-acceptor interface, CT states serve as crucial intermediaries in the process of exciton dissociation and charge extraction. The careful balance between the stability and dissociation of CT states determines whether the device will achieve efficient charge separation or suffer from excessive recombination.

Through the strategic management of these factors, organic solar cells can achieve enhanced performance. By controlling energy disorder, optimizing the depth and distribution of trap states, and fine-tuning the behavior of CT states, researchers can mitigate the inherent challenges of recombination while promoting efficient charge transport. The future of OSC technology depends on the continued exploration and optimization of these complex interrelated processes.

Nonfullerene acceptors (NFAs)

Nonfullerene acceptors (NFAs) offer several advantages over traditional fullerene-based acceptors, making them highly attractive for organic solar cell applications. These advantages include stronger absorption coefficients, better energy level alignment, and more favorable morphological properties, all of which contribute to enhanced charge generation, separation, and transport[67,68]. As a result, NFAs minimize recombination losses and improve overall device performance. Some of the most widely studied NFAs include **ITIC**, **Y6**, and **IEICO-4F** (**Fig. 8**).

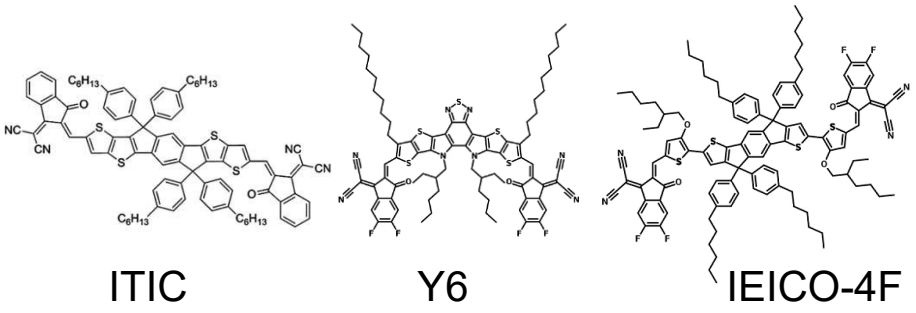

Fig. 8 Chemical structures of ITIC, Y6 and IEICO-4F.

One of the key advantages of NFAs like ITIC and Y6 is their strong light absorption capacity[69,70]. These materials are specifically designed to absorb a broader spectrum of sunlight, particularly in the visible and near-infrared regions, which fullerene-based acceptors typically miss. This broader

absorption spectrum enhances the generation of excitons, thereby increasing the photocurrent. In addition to their absorption properties, NFAs allow fine-tuning of their energy levels to align more effectively with donor materials. This optimized energy level alignment ensures efficient charge transfer at the donor-acceptor interface, facilitating the dissociation of excitons into free charge carriers. NFAs like ITIC and Y6 exhibit excellent energy level matching, which helps reduce energy losses typically associated with charge transfer, minimizes the driving force required for charge separation, and lowers the probability of recombination[67,71].

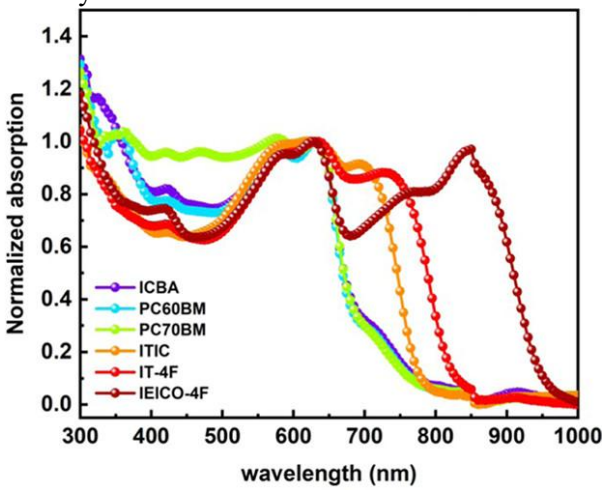

Fig. 9 Normalized UV−vis absorption spectra for the films of various photoactive blends prepared by mixing donor polymer PBDB-T independently with different FBAs and NFAs.[68]

NFAs also tend to form more ordered and crystalline domains within the active layer of organic solar cells (OSCs) compared to fullerene-based acceptors[72,73]. Materials like ITIC, Y6, and IEICO-4F contribute to the formation of well-ordered structures, enhancing charge transport by creating well-defined pathways for electrons and holes to move efficiently toward the electrodes. This improved charge transport reduces the residence time of charge carriers in the active layer, further decreasing the likelihood of recombination. Additionally, the crystallinity of NFAs contributes to the overall morphological stability of the active layer, which is crucial for maintaining high efficiency over time and in diverse environmental conditions.

Moreover, NFAs exhibit lower energetic disorder compared to fullerene acceptors. Energetic disorder, which refers to the distribution of energy states within the material, can lead to traps that impede efficient charge transport. NFAs, particularly those like IEICO-4F, typically demonstrate reduced energetic disorder, enabling higher mobility for both electrons and holes,

which further reduces recombination and improves charge extraction efficiency[74,75].

In summary, the development of bulk heterojunction (BHJ) organic solar cells is becoming increasingly intricate with the introduction of new ternary and quaternary systems, novel polymers, and non-fullerene acceptors. These advancements offer exciting opportunities to enhance photovoltaic performance but also introduce new challenges in understanding the complex interactions between material properties, charge dynamics, and recombination mechanisms. As research into these systems progresses, refining existing analytical techniques will be essential to keeping pace with these innovations. A strategic approach would involve first simplifying and deepening our understanding of BHJ fundamentals, providing a solid foundation before tackling the complexities of more advanced systems.

2.4.4. Super second order recombination

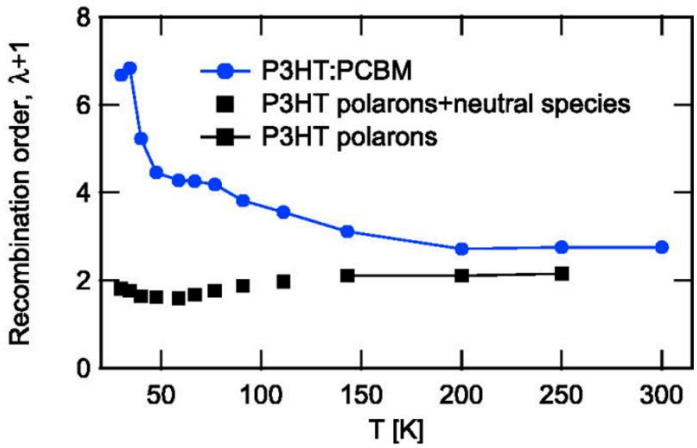

Fig. 10 Apparent recombination order as a function of temperature for neat P3HT and P3HT blend films, derived from transient absorption spectroscopy measurements and temperature-dependent mobility data. The results illustrate the temperature dependence of nongeminate recombination dynamics, with deviations from Langevin theory observed at lower temperatures[28].

Recombination order in OPVs defines how the rate of recombination, R, changes with the density of charge carriers, n. In the simplest scenario, bimolecular or Langevin recombination occurs when free electrons and holes recombine, resulting in a second-order process where R is proportional to the square of the charge carrier density ($R \propto n^2$). However, this idealized picture is often complicated by the presence of traps and energetic disorder within the material. In the case of Shockley-Read-Hall (SRH) recombination, which involves recombination between free and trapped carriers, the process is first-

order ($R \propto n$) because the rate depends on the density of free carriers interacting with a relatively stable population of trapped carriers.

In practical OPV devices, both Langevin and SRH recombination mechanisms can coexist, leading to an effective recombination order that falls between 1 and 2. This mixture of mechanisms is further complicated by the observation that empirical recombination orders often exceed 2 (**Fig. 10**). This behavior highlights additional complexities, such as the role of traps, energetic disorder, and spatial inhomogeneity, which must be accounted for when designing and optimizing OPV devices.

Super-second-order kinetics, or super-second-order recombination, refers to cases where the recombination rate scales more steeply with carrier density than predicted by second-order kinetics.

Several factors contribute to super-second-order kinetics in OPVs. In materials with a high density of trap states, free carriers can become temporarily trapped. The subsequent release and recombination of these carriers lead to a higher recombination rate than would be predicted by a simple second-order model. The effective recombination order increases as a result of this trap-assisted process, particularly when there is a significant disparity between free and trapped carrier populations.

In addition, OPVs are characterized by disordered molecular packing, resulting in a broad distribution of electronic states. If the density of states is broad and asymmetric, carriers can populate low-mobility tail states, leading to an increased probability of recombination. This disorder can cause the recombination rate to become more dependent on carrier density, resulting in an effective reaction order higher than 2.

When recombination involves intermediate states, such as charge transfer states (CTS) or deeply trapped states, the recombination process can involve multiple steps, each with its own kinetics. This can lead to an overall rate that scales more sharply with carrier density, effectively increasing the recombination order.

Understanding reasons behind super-second-order kinetics is crucial for optimizing OPV devices, as it highlights the importance of managing both free and trapped carriers to minimize recombination losses.

2.4.5. Limitations of the Bimolecular recombination parameter

The bimolecular recombination parameter β is a useful metric for understanding how charge carriers—such as electrons and holes—recombine in these materials. However, despite its utility, this parameter comes with several notable limitations that affect its reliability and accuracy in characterizing recombination processes.

One significant limitation of the bimolecular recombination parameter is its lack of specificity. This parameter does not differentiate between the various recombination mechanisms that can occur within a photovoltaic material. For instance, it treats free-free recombination (where two free carriers recombine), free-trapped recombination (where a free carrier recombines with a trapped one), and trapped-trapped recombination (where two trapped carriers recombine) all under the same umbrella. Consequently, it fails to provide detailed insights into the distinct pathways that contribute to recombination losses. This lack of granularity can obscure the underlying physics of the recombination processes, making it challenging to identify and mitigate specific recombination pathways that might be detrimental to device performance .

Additionally, the bimolecular recombination parameter is typically derived under the assumption of a uniform distribution of carriers and a homogeneous recombination environment. This assumption oversimplifies the complex reality of organic photovoltaic (OPV) materials, which often exhibit significant morphological and energetic disorder. In practice, OPV materials are inhomogeneous, featuring regions with varying carrier densities and different energetic landscapes. As a result, the assumption of homogeneity can lead to inaccuracies when predicting real device performance, as the parameter may not accurately reflect the localized recombination dynamics within these materials.

Moreover, the bimolecular recombination parameter is highly sensitive to experimental conditions. Factors such as temperature, illumination intensity, and the presence of external electric fields can significantly influence its value. This sensitivity introduces variability that complicates the use of this parameter for universal comparisons across different materials or device architectures. The dependency on specific experimental conditions means that the recombination parameter obtained in one set of circumstances may not be directly comparable to those obtained under different conditions, further limiting its applicability as a universal metric.

2.4.6. Charge carrier dependent recombination rate measurements

Understanding and improving the performance of organic photovoltaics (OPVs) requires a deep exploration of how charge carriers behave under different conditions. These charge carriers, including both free and trapped carriers, are responsible for generating the electrical current that powers these devices. However, their movement, interaction, and recombination are governed by complex dynamics that must be meticulously analyzed. To gain

meaningful insights into these processes, researchers employ a variety of sophisticated techniques. Each of these techniques provides a different perspective on charge carrier behavior, from their generation and transport to their recombination, and contributes to an overarching understanding of OPV performance[76].

One of the primary methods used to investigate charge carrier density is charge extraction (CE). This relatively straightforward technique involves illuminating the OPV device to generate charge carriers, then applying a reverse bias to extract them after the light is switched off. The current generated during this extraction process is measured over time, and by integrating this current, the total charge density in the device can be determined[77]. Despite its simplicity, CE is not without its limitations. It assumes that all charge carriers are extracted instantaneously, an assumption that falls short when dealing with real devices, particularly those with slow recombination dynamics or significant trapping effects. This can lead to an underestimation of the true recombination rate. Furthermore, CE lacks the ability to provide insights into how charge carriers are spatially distributed across the device or differentiate between free and trapped carriers, limiting its utility in capturing the full complexity of charge transport and recombination mechanisms in more advanced OPV systems[78].

To improve upon this, time-resolved charge extraction (TRCE) extends the CE method by adding a temporal dimension. Instead of simply measuring the current after turning off the light, TRCE involves generating a population of charge carriers with a short light pulse and then tracking how these charges evolve over time by varying the delay between the pulse and the extraction event[79]. This method allows researchers to observe the recombination dynamics over specific time windows, typically on the scale of microseconds to milliseconds. TRCE provides valuable insights into how quickly charge carriers recombine, offering a more detailed understanding than standard CE. However, like CE, TRCE assumes all charges are extracted in the measurement, which may not hold true for devices with slow-moving carriers or significant trap states. Additionally, TRCE lacks the ultrafast temporal resolution needed to capture very rapid recombination events, which are often crucial for understanding the early stages of charge carrier behavior in OPVs.

To probe these ultrafast processes, transient absorption spectroscopy (TAS) is employed. TAS is a powerful technique that can capture events occurring on the timescale of femtoseconds to picoseconds, making it one of the most effective tools for studying the earliest moments of charge generation and recombination in OPVs. In a TAS experiment, a short laser pulse excites the sample, and a delayed probe pulse measures changes in absorption as the

excited states evolve over time. This pump-probe approach allows researchers to track the behavior of transient species such as excitons, charge carriers, and intermediate states[80]. By analyzing changes in absorption across different wavelengths, TAS provides detailed insights into charge generation, transfer, and recombination. Specifically, it excels in capturing the ultrafast dynamics of exciton dissociation and polaron formation, which are critical for understanding the early steps of charge separation. However, TAS requires highly sophisticated and expensive equipment, including ultrafast lasers and sensitive detectors, which limits its accessibility. Additionally, interpreting TAS data can be complex due to overlapping signals from multiple transient species, necessitating advanced deconvolution techniques that can introduce uncertainties. Moreover, TAS is typically performed on thin films rather than fully operational devices, meaning some recombination dynamics that occur under real-world conditions may be missed.

In contrast, techniques such as transient photovoltage (TPV) and transient photocurrent (TPC) measurements are used to study charge carrier dynamics under conditions that more closely simulate real-world device operation[81]. TPV introduces small perturbations in the photovoltage, and the decay of the voltage over time provides information about the lifetime of charge carriers[82]. Similarly, TPC measures how the photocurrent decays, revealing insights into carrier densities. These techniques are performed under steady-state illumination, allowing them to simulate near-operational conditions. One of the key advantages of TPV and TPC is their simplicity, and the fact that they can be performed on fully operational devices[83]. However, they are sensitive to external factors such as light intensity, temperature, and background illumination, all of which can influence the reproducibility of the results. Additionally, TPV and TPC may not effectively distinguish between recombination involving free carriers and trapped carriers, particularly in systems with significant energetic disorder, which is common in organic materials[84]. If the perturbation is too small, the recombination rate can be underestimated, as the system may not be disturbed enough from its steady state to reveal the full dynamics of recombination.

To simultaneously measure charge carrier mobility and recombination rates, researchers employ photoinduced charge carrier extraction by linearly increasing voltage (photo-CELIV). In a typical photo-CELIV experiment, the device is illuminated with a short light pulse to generate charge carriers. After the pulse, a linearly increasing voltage is applied to extract the charges, and the resulting current is measured as a function of time. This method provides insights into both charge mobility and recombination rates, making it particularly valuable for studying materials with complex charge transport

properties[85]. However, photo-CELIV relies on the assumption that the electric field across the device is homogeneous, which may not be the case in thick or highly disordered films[86]. This can lead to inaccuracies in the calculated mobility or recombination rates. The technique's temporal resolution is also limited by the rate at which the voltage is ramped, meaning that very fast recombination processes may not be accurately captured.

Another technique that focuses on the field-dependent dynamics of charge carriers is time-delayed collection field (TDCF). In TDCF experiments, charge carriers are generated in the device with a laser pulse while the device is held at a pre-set bias voltage. After a controlled delay, a stronger collection voltage is applied to extract the remaining charges. By varying both the time delay and the strength of the applied field, TDCF allows researchers to study how charge carriers recombine under different electric field conditions[87]. This technique is particularly useful for investigating how the built-in electric field of an OPV device affects charge separation and recombination[88]. However, TDCF requires precise control over the timing and magnitude of the applied voltages, which can be technically challenging. Even small errors in timing or voltage calibration can lead to significant inaccuracies in the measurement of recombination rates or charge collection efficiency[89]. Additionally, TDCF may struggle to differentiate between fast and slow recombination processes when both occur simultaneously under different field strengths, making the interpretation of the data more complex.

No single technique can capture all aspects of recombination dynamics due to the complex interplay of material properties, device architecture, and external conditions. Therefore, combining multiple techniques is often necessary to obtain a more complete picture. For instance, using TAS to study ultrafast dynamics and TPV/TPC to analyze steady-state conditions can provide complementary insights into both transient and equilibrium recombination processes. Moreover, considering super-second-order kinetics is crucial when interpreting data, as higher-order recombination rates can significantly impact device performance under elevated carrier densities.

3. Investigation techniques

3.1. Time-of-flight (TOF) technique

In order to evaluate charge carrier mobilities and bimolecular recombination rates in the investigated materials the time of flight (TOF) method was employed. Originally developed by R. G. Kepler for studying low mobility amorphous materials, it remains widely used because of its simplicity and effectiveness. The method involves monitoring the drift of photogenerated charge carriers across the full thickness of a sample under applied constant external electric field.

In a typical TOF experiment, a voltage is applied in the reverse bias to a low conductivity sample with at least one blocking contact, to avoid charge carriers injection. After a brief period, the sample is illuminated with a short light pulse that is strongly absorbed by the material. It is crucial that the photogenerated charge Q_0 should be smaller than the charge accumulated on the sample's electrodes ($Q_0 \ll CU$). Once generated, the charge carriers begin to drift under the influence of the electric field. Carriers of one type (either electrons or holes) traverse the entire sample thickness, generating a current as they move (**Fig. 11**). When these carriers reach the opposite electrode, the current decreases. Meanwhile, carriers of the opposite type move towards the illuminated electrode, where they quickly recombine. In the case of strong absorption these carriers have short drift distances and do not significantly affect the current kinetics.

The time it takes for the carriers to reach the opposite electrode, known as the transit time (t_{tr}), allows for the calculation of charge carrier mobility μ using the formula:

$$\mu = \frac{d^2}{U t_{tr}} \tag{3.1}$$

where d is the sample thickness, U is applied voltage. After determining the mobilities using the TOF method, the Langevin recombination coefficient can be calculated. The Langevin recombination coefficient B_L is defined as:

$$B_L = \frac{e(\mu_e + \mu_h)}{\varepsilon} \tag{3.2}$$

where μ_e and μ_h are the mobilities of electrons and holes, respectively, e is the elementary charge, and ε is the permittivity of the material.

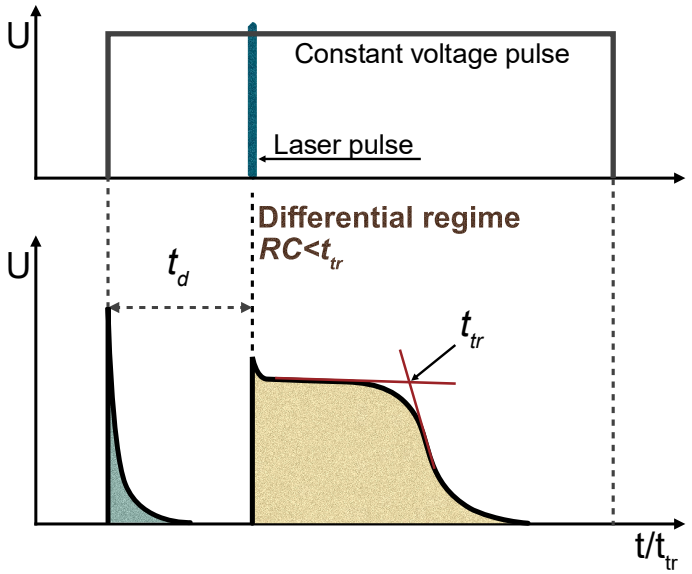

Fig. 11 Illustration of the time of flight (TOF) differential regime for measuring the transit time t_{tr}, here t_d is delay time between voltage and laser pulse.

To ensure accurate measurements, several conditions must be satisfied. The electric field within the sample must be constant and uniform, which requires:

$$t_d > RC \tag{3.3}$$

where R is the load resistance and C is the capacitance of the sample, and t_d is the delay time needed to fully charge the capacitance of the sample. The conductivity of the sample's must also need to be considered, equilibrium charge carriers should not distort the electric field, necessitating:

$$\tau_\sigma = \frac{\varepsilon\varepsilon_0}{\sigma} > t_d + t_{tr} \tag{3.4}$$

where τ_σ is the Maxwell relaxation time, and σ is the material's conductivity. Furthermore, carriers must reach the opposite electrode without recombining, which requires:

$$\mu\tau E > d \tag{3.5}$$

where τ is the carrier lifetime, and E is the electric field strength.

The TOF method can operate in different modes depending on the RC time constant relative to the transit time. If the RC time constant is shorter than the transit time ($RC < t_{tr}$), the method operates in differential mode (current mode), therefore instantaneous drift current is measured; if $RC > t_{tr}$, it operates in integral mode (charge mode) where the measured signal is time integral of the current. By increasing the load resistance, it is possible to switch from differential to integral mode, but in thin layers, due to high sample

capacitance *C*, differential mode is not always feasible. In TOF, it is preferable to generate carriers near the surface, satisfying:

$$\alpha d \gg 1 \qquad (3.6)$$

where α is the absorption coefficient. This condition ensures clear observation of the carriers' transit time across the sample and allows to distinguish between different carrier types (**Fig. 12a**). **Fig. 12b** shows bulk generation current kinetics.

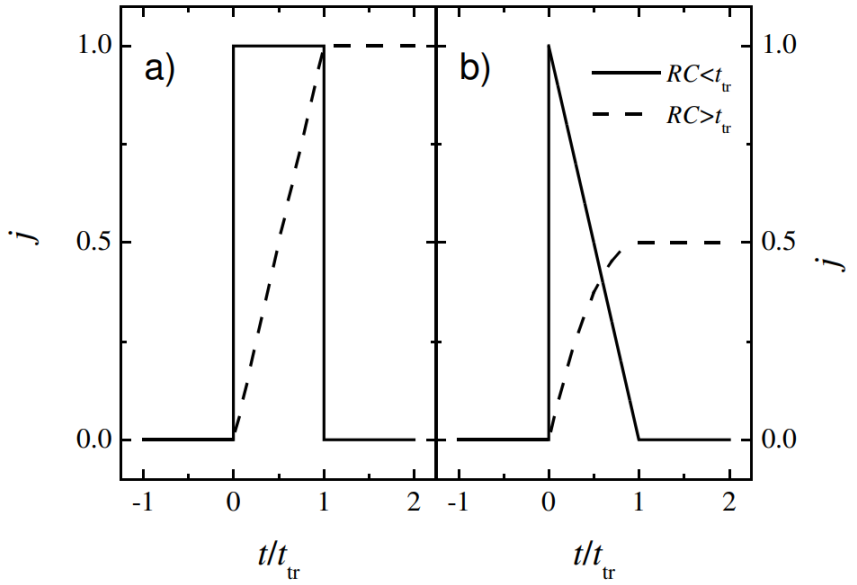

Fig. 12 Idealised photogenerated charge current transients (line – differential, dotted line- integral mode), a) – surface generation, b) - bulk generation.

In realistic organic semiconductors the broad distribution of localized states that forms the DOS tail renders carrier motion intrinsically dispersive. Under these conditions in differential TOF mode the photocurrent trace naturally divides into two power-law regimes that encode complementary information on the transport landscape. For times shorter than the transit time ($0 < t < t_{tr}$) only the fastest carriers—those momentarily occupying the shallowest localized states—contribute to the conduction current. Their relaxation through a broad, quasi-exponential density-of-states tail gives a power-law decay $I(t) \propto t^{-(1-\alpha)}$ with $0 < \alpha < 1$; the exponent $\alpha = kT/kT_0$ is therefore a direct, field-independent measure of the energetic width kT_0 of that trap manifold. The steady drop in current shows that carriers are moving into deeper localized states, where more of them become trapped. After the transit knee ($t > t_{tr}$) the front of the packet has been extracted and the current is carried by slower charge carriers that undergo repeated deep trapping and

release. This yields a fall-off $I(t) \propto t^{-(1+\alpha)}$ for an ideal exponential DOS. Thus, the pre-transit slope diagnoses the shallow-trap energetics that govern initial mobility, whereas the post-transit slope reflects deep-trap relaxation dynamics and any late-time loss channels—together providing a compact fingerprint of the full trap landscape probed by the measurement. At sufficiently low electric fields, where no transit knee appears, the current decay is determined first by capture into increasingly deeper states and subsequently by recombination losses.

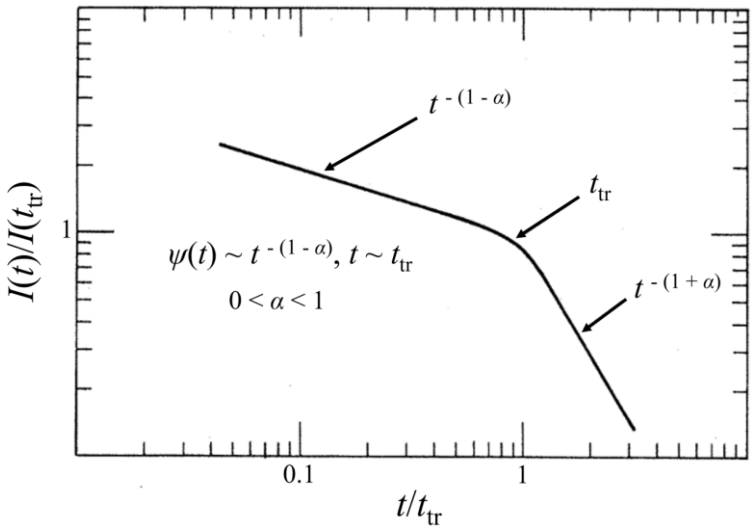

Fig. 13 A log-log photocurrent transient in TOF differential regime and evaluation of t_{tr}. $\Psi(t) \sim t^{-1-\alpha}$ is a hopping time distribution function.[90]

In scenarios where the number of photogenerated carriers is comparable to or exceeds CU, different operational modes arise. When $Q \approx CU$, the system operates in a charge-perturbed mode (**Fig. 14**). When $Q \gg CU$, it enters the space-charge limited current (SCLC) regime. In SCLC regime, only the carriers injected near the contact move at first; as they advance, they screen the electric field behind them, confining it to a thinner region ahead of the front and thereby intensifying its magnitude. This causes the packet of charge carriers to reach the opposite electrode faster than the transit time t_{tr} in $Q \ll CU$. The number of extracted carriers under these conditions is heavily influenced by the recombination coefficient.

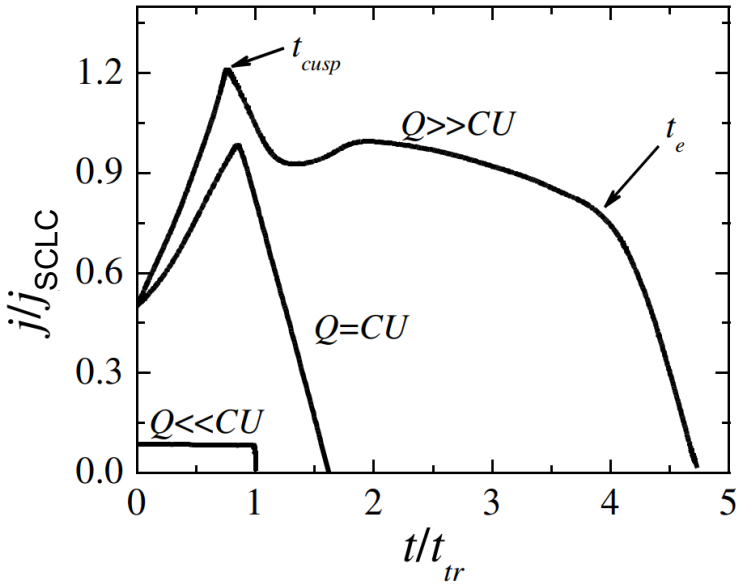

Fig. 14 Photogenerated charge transients in charged perturbed mode ($Q \approx CU$), SCLC mode ($Q \gg CU$) and in case of small photogenerated charge ($Q \ll CU$). t_e - duration of carrier extraction from the sample.

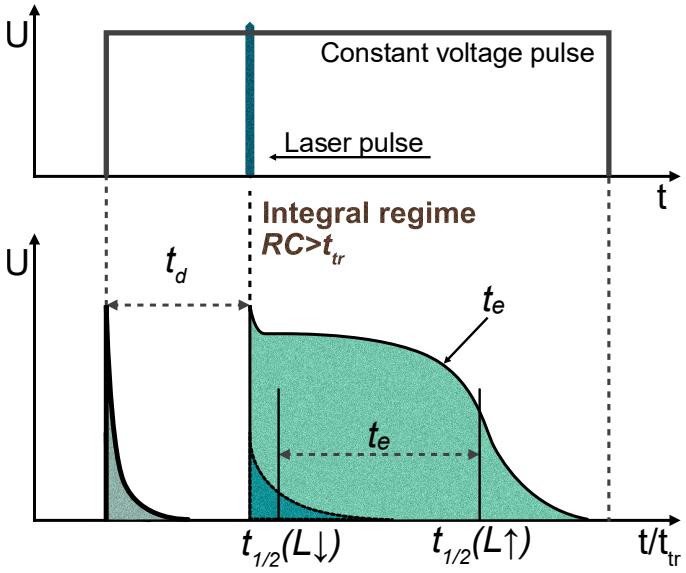

Fig. 15 Illustration of the integral time of flight (TOF) for the measurement of extraction time t_e of the photogenerated current. Here $t_{1/2}(L\downarrow)$ and $t_{1/2}(L\uparrow)$ represent time at half-height of photocurrent for weak $L\downarrow$ ($Q \ll CU$) light intensity and photocurrent saturated on high $L\uparrow$ light intensities.

For thin samples ($\alpha d \leq 1$) in integral mode ($RC > t_{tr}$), a short laser pulse can create a reservoir of charge carriers in the bulk. Over time, the carrier density changes due to monomolecular recombination through the recombination states, described by:

$$\frac{dn}{dt} = -\frac{n}{\tau}, \quad n(t,x) = \frac{L\alpha}{e} e^{-\alpha x} e^{-\frac{t}{\tau}} \tag{3.7}$$

where L is the intensity of the incident laser radiation ($\frac{C}{cm^2}$). The total number of carriers N in the sample at time moment t:

$$N(t) = Le^{-\frac{t}{\tau}}\left(1 - e^{-\alpha d}\right) \tag{3.8}$$

When $RC \gg t_{tr}$, the extraction current will be limited by R and extraction time t_e (**Fig. 15**) will be influenced by recombination rate and R and then the extracted charge Q_e over the extraction time t_e will be:

$$Q_e = \frac{1}{e}\int_0^{t_e} j(t)dt \tag{3.9}$$

When the remaining non-recombined charge equals the extracted charge:

$$Le^{-\frac{t_e}{\tau}}\left(1 - e^{-\alpha d}\right) = Q_e \tag{3.10}$$

the extraction time can be expressed as:

$$t_e = \tau \ln\left(\frac{L\left(1 - e^{-\alpha d}\right)}{Q_e}\right) \tag{3.11}$$

Equation (3.11) demonstrates that with only monomolecular recombination, the extraction time is proportional to the logarithm of the incident radiation intensity. However, at very high laser intensities, linear recombination becomes negligible, and quadratic recombination takes precedence. In this case, the carrier density over time follows:

$$\frac{dn}{dt} = -Bn^2, \quad n(t,x) = \frac{1}{L\alpha e^{-\alpha x} + Bt} \tag{3.12}$$

The total number of carriers can be obtained by integrating over sample thickness:

$$N(t) = \frac{1}{Bt\alpha}\left(\alpha d - \ln\left(BtL\alpha + e^{\alpha d}\right) + \ln(BtL\alpha + 1)\right) \tag{3.13}$$

If $L \to \infty$, this simplifies to:

$$N(t) = \frac{d}{Bt} \tag{3.14}$$

The extraction time t_e for bimolecular recombination is given by:

$$t_e = \frac{ed}{B\int_0^{\infty} j\, dt} \tag{3.15}$$

The bimolecular recombination coefficient B can be calculated using:

$$B = \frac{ed}{t_e \int_0^\infty j\, dt} \tag{3.16}$$

and its ratio to the Langevin recombination coefficient is expressed as:

$$\frac{B}{B_L} = \frac{CU}{Q}\frac{t_{tr}}{t_e}. \tag{3.17}$$

Thus, at saturated photocurrent when $RC \gg t_{tr}$, we can evaluate bimolecular recombination coefficient. TOF method—operating under different regimes provides a versatile platform for probing carrier transport, recombination mechanisms, and how these processes scale with changing thickness, morphology and additives that impact morphology. Combining this technique with EIC experiments and numerical simulations, TOF measurements will lead to deeper insights into the interplay among carrier mobility, recombination coefficients and carrier concentrations in P3HT:PCBM bulk-heterojunctions.

3.2. Extraction of injected charge carriers (EIC)

The extraction of injected charge carriers (EIC) technique (see **Fig. 16**) is used to investigate the interface recombination velocity υ, which governs the injection current j_{in} in planar heterojunction systems[91]:

$$j_{in} = en_0\upsilon, \tag{3.18}$$

where n_0 is carrier concentration at the interface. By measuring how the extracted charge Q depends on j_{in}, the recombination velocity at the interface can be estimated[91]:

$$\upsilon = \frac{2kT\varepsilon\varepsilon_0 j_{in}}{eQ^2}, \tag{3.19}$$

where ε is the dielectric permittivity of the layer.

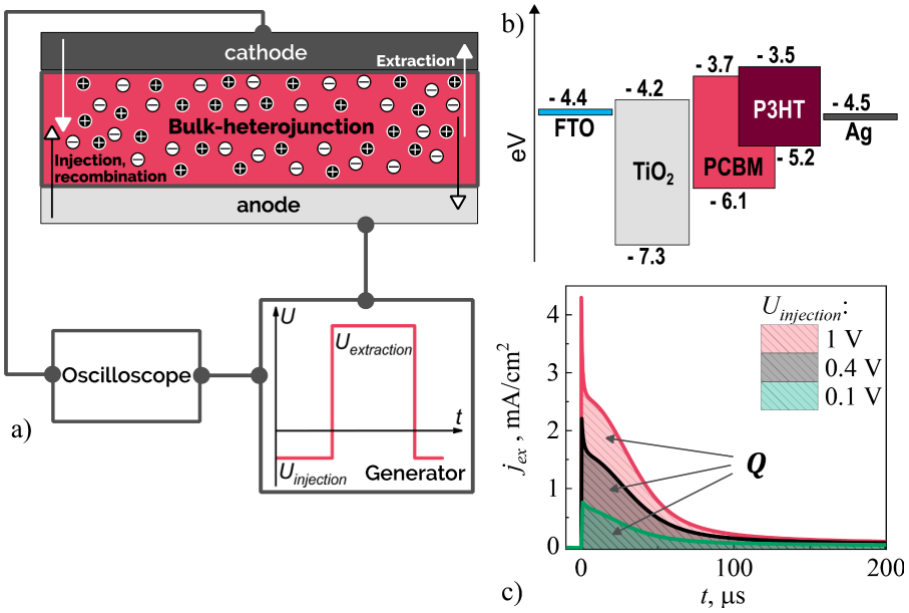

Fig. 16 . Schematic view of injection and extraction of charge carriers in bulk-heterojunction (a), energy band diagram of P3HT: PCBM solar cell configuration (b), and example of numerically calculated current transients for different injection voltages (c), here Q represents charge extracted from the device.

In a bulk heterojunction (BHJ) the photo-active layer is no longer stratified but forms a three-dimensional interpenetrating network of donor and acceptor phases. Charge carriers are therefore generated and recombine throughout the film thickness rather than at a well-defined planar interface. However, the same set of measurements can still yield meaningful insight once we reinterpret υ as an effective volume-averaged recombination velocity.

If the injection current in a BHJ is limited by monomolecular recombination in the bulk, then

$$j_{in} \propto e\frac{n(x)}{\tau} \propto en(x)\upsilon, \tag{3.20}$$

where υ does not change with the carrier concentration $n(x)$, and the carrier lifetime τ is inversely proportional to υ. If there are significantly different potential barriers for electron and hole injection, one type of carrier will accumulate at the interface with the larger barrier, blocking injection of the opposite carrier. In such a scenario, the current is limited by interface recombination at the barrier, and the recombination velocity can be estimated similarly to the ETL/HTL case.

For bimolecular recombination

$$j_{in} \propto e\beta n(x)^2\,, \tag{3.21}$$

so the recombination velocity υ and bimolecular recombination rate β are linearly related:

$$\beta \propto \frac{\upsilon}{n(x)} \propto \frac{\upsilon}{Q}\ . \tag{3.22}$$

In theory, for bimolecular recombination, υ should scale linearly with $n(x)$. However, it is uncertain whether this remains valid in practical BHJ systems, since carriers are distributed throughout the film thickness, leading to recombination across the entire volume. To investigate how volumetric carrier distributions affect υ, the next section presents a numerical model that enables simulation of EIC kinetics and interpretation of the resulting volume-averaged recombination coefficient.

3.3. Investigation of charge carrier transport using finite difference method (FDM)

The Finite Difference Method is a numerical technique used to solve differential equations by approximating derivatives with finite differences. It discretizes the problem domain into a grid of points, allowing complex physical processes to be represented as algebraic equations that can be solved numerically. FDM is particularly useful for problems involving transport phenomena, wave propagation, and diffusion, where it provides an efficient and straightforward approach to obtaining approximate solutions.

In this work, FDM was applied to model the transport and recombination of charge carriers in bulk-heterojunction (BHJ) organic solar cells under conditions of charge injection. The active layer is subdivided into numerous one-dimensional elements, enabling a detailed simulation of how drift, diffusion, and recombination govern carrier behavior within the device.

The experimental setup simulated here involves the extraction of injected charge carriers. The process begins by injecting charge carriers through the electrodes (without barriers), delivering a charge equal to CU, where C is the capacitance and U is applied voltage. The distribution of these carriers in the active layer is governed by the applied electric field, diffusion, and the specific recombination mechanisms and their rates. Once the injection current stabilizes (equilibrium is reached between recombined and injected charge carriers), the carriers are extracted using a constant-voltage pulse of opposite polarity.

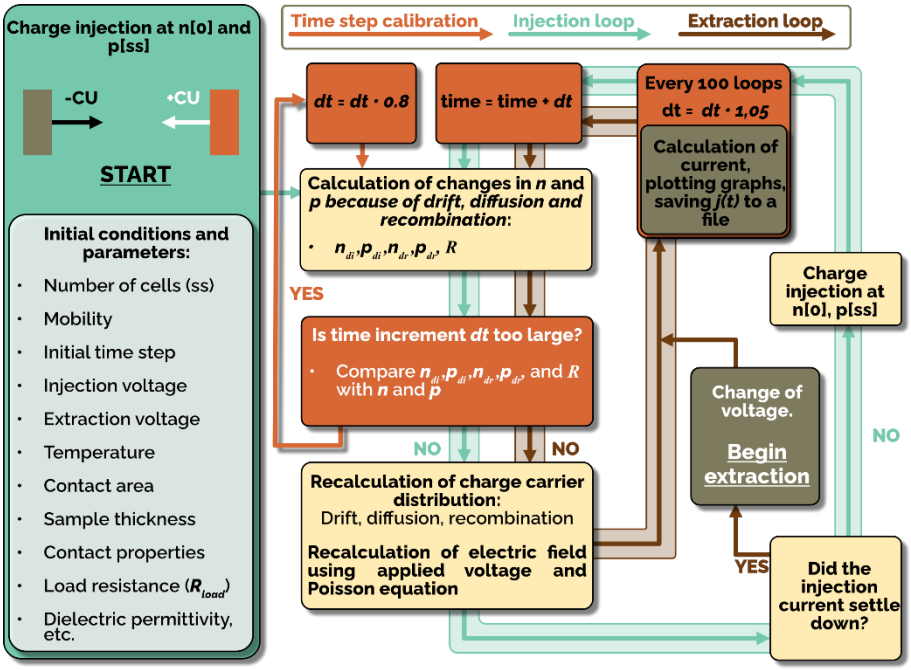

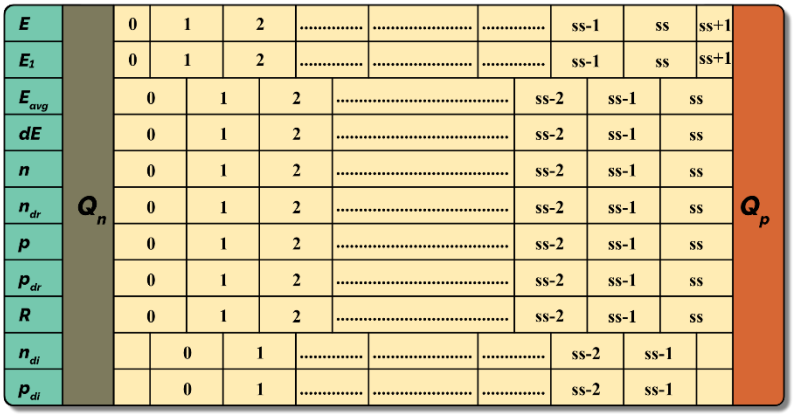

Fig. 17 Flowchart for simulation of extraction of injected charge carriers and active layer cell division of different parameters.

Fig. 17 shows a detailed flowchart of the EIC simulation. Once the initial conditions are set and the simulation begins, charge carriers are injected into the first and last subdivision cells of the active layer for their respective charges. At each iteration, changes in carrier concentrations are recalculated in respect to the number of carriers (n, p) leaving a cell determined by drift (n_{dr}, p_{dr}), diffusion (n_{di}, p_{di}), and recombination (R). If the time step is too large, meaning that number of carriers leaving the cell is to large, the program reduces dt.

The simulation proceed to recalculate the charge carrier distribution across all cells, and then updates the current and electric field based on the applied voltage and Poisson's equation. In the EIC method, the load resistance is much smaller than the resistance of the tested layer, ensuring that the entire voltage drop is across the sample. This makes the electric field calculation straightforward.

At each iteration, charge is injected into the first and last cells, ensuring that the electric field in the first and last cell is zero. The ideal contacts allow only one type of carrier, blocking the other. After every iteration, the simulation checks whether the injection current has stabilized. When the carrier-recombination rate approaches the injection rate, the extraction phase begins: the voltage polarity is reversed, and carriers are extracted through the electrodes. The extraction loop mirrors the injection loop, with the extraction current recorded at intervals. The simulation ends once the extraction current drops below the specified threshold.

The schematic in **Fig. 17** illustrates the discretization of a one-dimensional organic solar cell, where the active layer is divided into a number of small segments or cells. Each row in the table represents a variable tracked in each discretized element or cell of the model. E is the electric field at the cell boundaries, and $E_1$is the electric field at the previous time step. E_{avg} denotes the average electric field between the neighboring cells, while dE is the difference in electric field across the cell boundaries. n and p represent the electron and hole concentrations, respectively. n_{dr} and p_{dr} represent the concentration of electrons and holes leaving the cell due to drift, while n_{di} and p_{di} are the concentrations moving between cells due to diffusion. R is the recombination rate in each cell. The variables are tracked for every discretized segment from cell 0 to ss (the total number of cells).

A more detailed description with fundamental principles of calculation is presented in APPENDIX I.

4. Results and discussion

4.1. Investigation of recombination processes in P3HT:PCBM bulk heterojunction device by extraction of injected charge carriers

As discussed in previous chapters, the recombination rate in poly(3-hexylthiophen-2,5-diyl) and [6,6]-phenyl-C61-butyric acid methyl ester (P3HT:PCBM) bulk heterojunctions (BHJs) is up to 10^4 times slower than predicted by Langevin theory. Furthermore, polymer-fullerene blends do not exhibit the typical second-order (bimolecular) recombination behavior. Instead, the recombination has been observed to follow a higher-order mechanism, with an order ranging between 2.3 and 2.8. This indicates that higher-order decay cannot be explained solely by reduced Langevin recombination, as the reduction factor becomes dependent on carrier concentration. Consequently, recombination may not rely entirely on encounter probability, as described by Langevin theory. The more complex morphology observed in P3HT:PCBM blends, including the presence of a third amorphous phase, suggests that recombination through interfacial states likely dominates. Therefore, this chapter investigates the use of techniques such as extraction of injected charge carriers (EIC), time-of-flight (TOF) measurements, and Finite Difference Method (FDM) calculations to establish the dependence of the recombination rate on carrier concentration and BHJ thickness. Understanding this dependence is particularly important when using the DIO additive, which is known to impair the morphology of P3HT:PCBM blends as the sample thickness increases.[87]

In the case of the reduced recombination in the active layer, carriers are distributed across the full thickness of the layer (**Fig. 18a**). Numerical results in **Fig. 18b** indicate that bimolecular recombination indeed demonstrates a $\upsilon \sim Q$ dependence, as described by Eq. (3.22). Both matched and mismatched carrier mobilities yielded similar recombination profiles in the calculations. Hence, by measuring how extracted charge depends on injection current and the evaluating the resulting recombination velocities in BHJ systems, one can establish the dependence of υ on carrier concentration and identify the dominant recombination mechanisms.

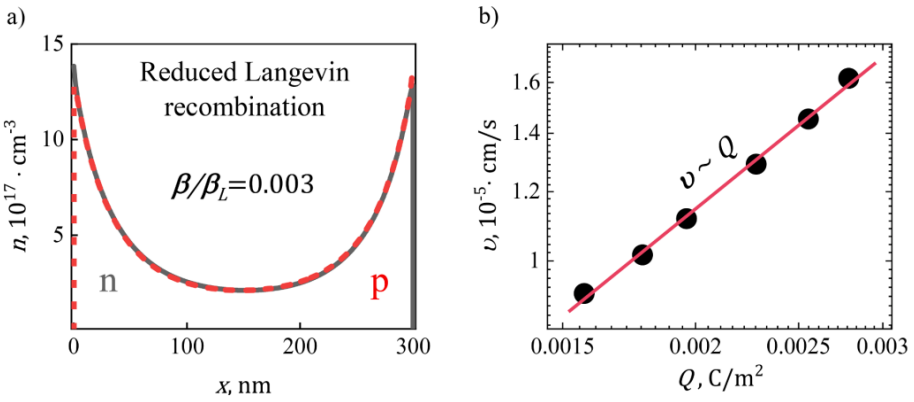

Fig. 18 Numerically calculated plot of charge carriers distribution (n-electrons injected through anode at $x = 0\ nm$, p-holes - through cathode at 300 nm) in case of bimolecular recombination with $\mu_{hole} = \mu_{electron}$ a) and b) numerically calculated recombination velocity dependence on extracted charge in case of bimolecular recombination (P3HT: PCBM 1: 1, $\varepsilon = 3.5$, $\mu_{hole} = \frac{10^{-4}\ cm^2}{Vs}$, $\mu_{electron} = \frac{10^{-3}\ cm^2}{Vs}$, $\frac{\beta}{\beta_L} = 0.003$, where β_L represents Langevin recombination rate).

In real devices, potential barriers for carrier injection often exist (**Fig. 16b**). However, such barriers merely reduce the number of injected carrier; they do not alter the overall $\upsilon(Q)$ dependence for the recombination velocity.

The bimolecular recombination coefficient was determined using TOF technique described in the previous section. A 3 ns Nd: YAG laser was used operating in the second harmonic (532 nm) with integral TOF mode.

For extraction of injected charge carriers' measurements, a signal generator (Tektronix AFG3022B) and oscilloscope (Tektronix DPO4054B) were used. A constant voltage pulse was applied in forward bias for electron and hole injection and a constant voltage pulse of opposite polarity was applied to extract them. Symmetrical injections into the active layer were assumed, because of similar injection barriers for electron and holes as shown in **Fig. 16b**. If, due to strong asymmetric injection, charge accumulates at ETL or HTL interface, this would be reflected in the extraction kinetics and $\upsilon(Q)$ dependence. In the case of weak asymmetric injection, charge and electric field would equibrilate at the donor acceptor interface, and this would not alter the $\upsilon(Q)$ dependence. In a situation where either type of charge carrier cannot enter the ETL or HTL, the injection current will be close to zero.

Samples were prepared by etching fluorine doped tin oxide (DYESOL TEC7 Glass Plates) coated glass slides (2 × 1.5 cm^2), firstly using etch resistant tape to cover part of the slide, where the cell's active area would be, then coating

the sample with zinc powder and covering the slide in a solution of 20% HCl. Then the substrates were cleaned with water, acetone, and isopropanol. After that, the compact TiO_2 layer was deposited by spray pyrolysis at 450°C from the precursor of diluted titanium diisopropoxide bis(acetylacetonate) solution in isopropanol.[92] Finally, solutions of regioregular P3HT (15 mg/ml, Sigma-Aldrich 99.9%) and PCBM (15 mg/ml Sigma-Aldrich, 99% purity) were prepared and then blended in the mass ratio of 1:1 in CB (Sigma-Aldrich, 99.9% purity) solvent with and without 3% of DIO additive (Sigma-Aldrich, 98% purity). The blend solution was stirred for 24 h at 60°C and then drop-casted onto the substrates at different volumes (80–200µl) to get varying thicknesses of the blend film. 40 nm silver electrodes with 5 mm^2 area were thermally evaporated on top of the structure.

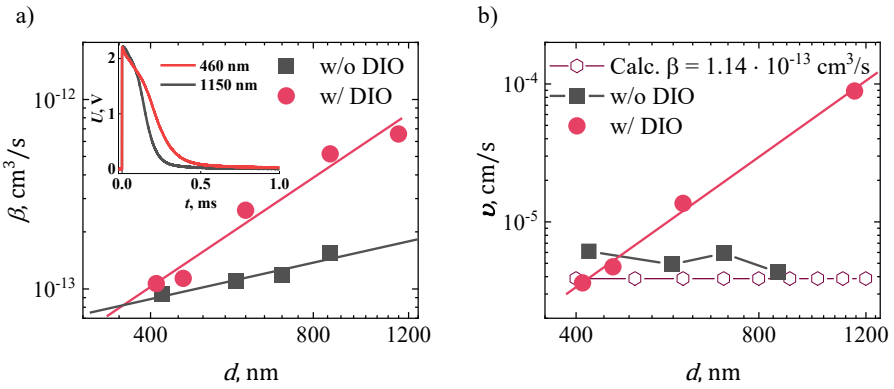

Fig. 19 a) Bimolecular recombination coefficient β determined using TOF and b) recombination velocity υ plotted as a function of P3HT: PCBM (blended in the ratio 1:1) active layer thickness with and without DIO processing additive. Inset in a) shows saturated integral TOF transients for different sample thicknesses w/ DIO.

Fig. 19 shows bimolecular recombination coefficient β and recombination velocity υ dependence on sample thickness. Here DIO additive appears to have a strong increase in recombination with increasing sample thickness. A common interpretation of such additive effect is that it selectively dissolves only the PCBM phase. In addition, it was also demonstrated that the combination of CB solvent and DIO additive reduces an overall number of ordered crystallites [93]. This effect is more pronounced in thicker samples that show increased recombination compared to BHJs made without DIO. υ dependence on thickness without DIO fall in line with numerical calculations, as carrier recombination velocity has no dependence on sample thickness and

bimolecular recombination coefficient is of the same magnitude as numerical calculations suggest (**Fig. 19b**), this shows that second or higher order recombination is present. The slight increase of bimolecular recombination coefficient with increasing sample thickness (**Fig. 19a**), might be because of different generation profiles and diffusion, but this dependence is significantly weaker compared to samples with DIO.

So, total recombination losses (**Fig. 19b**) in samples with DIO follow a steep dependency with increasing BHJ thickness; a similar picture is observed with the bimolecular recombination coefficient. The volatile nature of DIO additive in combination with CB solvent causes progressive morphological changes with increasing sample thickness, hence the additional charge carrier losses in bulk. Thicker samples with DIO have a more favorable morphology for charge carriers' recombination than samples without it.

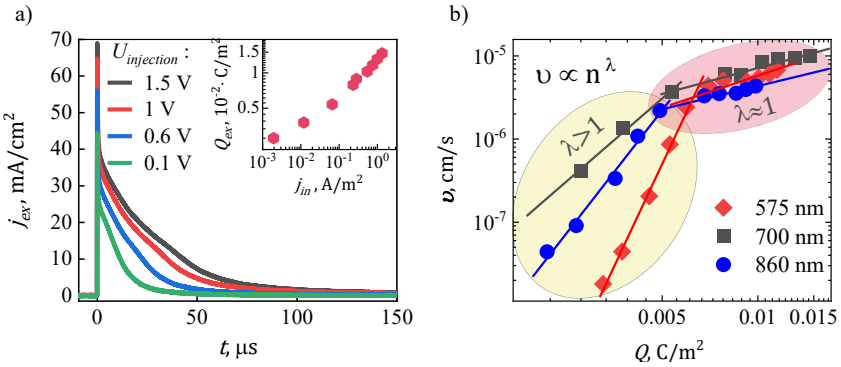

Fig. 20 a) Current transients of P3HT: PCBM 1:1 blend with inset of extracted charge dependence on injection current density for 700 nm sample (a) and recombination velocity dependence on extracted charge for samples of different thicknesses (b).

In order to evaluate recombination dependence on carrier concentration, extraction of injected charge carriers' transient kinetics was measured (**Fig. 20a**). As it can be seen the recombination velocity υ is dependent on the charge carriers' density. This means that recombination is not monomolecular and potential barriers do not obstruct double injection at applied injection voltages. In fact, recombination dependence on carrier density at lower concentrations is much more pronounced than it should be in the case of bimolecular recombination. Since recombination in P3HT: PCBM is known to be super-second-order, υ recombination velocity does not show dependence on carrier concentration as described in Eq (3.20). Considering interfacial states and

recombination through the multiple-trap-release model, pure domains and trap states in the interfacial region would not be populated proportionally, simply because of the fact, that pure domains with a Gaussian density of states are separated by a mixed interfacial phase with an exponential density of states [94]. As shown in **Fig. 20b**, recombination velocity demonstrates higher-order dependency on the extracted charge than in encounter limited regime, which is seen in **Fig. 20b**. That suggests that interfacial states fill up proportionally faster than the states in pure phases, and recombination is not encounter limited. That is why we see a distinct transition between the two components. When carrier concentration increases, interfacial states become fully populated, and recombination becomes encounter limited as states in pure phases are populated, and υ shows dependence on carrier concentration as defined in Eq (3.22).
To summarize, thickness-dependent bimolecular recombination coefficient observed in P3HT:PCBM (1:1) BHJs containing a DIO (1,8-diiodooctane) additive arises from morphological changes that become more pronounced as film thickness increases. In contrast, BHJs prepared without DIO exhibit a largely thickness-independent morphology. Notably, for films thicker than 400 nm, the presence of DIO leads to higher recombination compared to those prepared without the additive. From a practical standpoint, DIO is widely used in organic photovoltaics to promote more favorable phase separation and domain formation in thinner films, thus often improving device performance. So, in conclusion:

- Recombination velocities measured with the EIC technique indicate that, in P3HT:PCBM films thicker than 400 nm, the additive 1,8-diiodooctane induces morphology changes that heighten recombination losses as the layer thickness increases.

Beyond film thickness, the bulk recombination velocity in P3HT:PCBM (1:1) displays a nontrivial, two-component dependence on carrier concentration. The higher-order component arises from filling of interfacial states, eventually transitioning into an encounter-limited regime (where $\upsilon \propto Q$) once those states are fully occupied. The EIC method therefore offers a powerful tool for exploring how recombination processes evolve under varying carrier concentrations, providing deeper insights into the structure–function relationships in bulk-heterojunction systems. This lets us conclude that:

- EIC measurements map how bimolecular recombination velocity varies with carrier density in P3HT:PCBM bulk-heterojunctions, uncovering interfacial-state filling followed by an encounter-limited regime. Two distinct carrier-concentration regimes in P3HT:PCBM

blend originate from traps at the polymer–fullerene interface, confirming that recombination is largely interfacial rather than encounter-limited.

4.2. Cross-linkable fluorene-based hole transporting materials

The stability of bulk heterojunction (BHJ) organic solar cells (OSCs) poses a multifaceted challenge arising from both intrinsic and extrinsic degradation pathways. Strategies for improving stability include optimizing device architectures—often favoring inverted designs for enhanced environmental stability—using advanced encapsulation methods to protect against moisture and oxygen infiltration, and meticulously controlling the morphology of the active layers. In OSCs, cross-linkable materials can be employed within the photoactive layer or as interfacial layer to stabilize morphology, reduce phase separation, and shield the device from environmental stressors. By forming robust networks, these cross-linkable materials bolster the mechanical and chemical stability of the device[95,96].

As discussed previously, BHJs are susceptible to thermal degradation and morphological evolution over time, which leads to phase separation. Cross-linkable strategies offer a possible solution to mitigate these issues. However, the main drawback of cross-linking is its potential to adversely affect charge transport properties: forming new bonds and breaking old ones can introduce spatial and energetic disorder. Thus, in this section, we investigate novel fluorene-based hole-transporting materials (HTMs) synthesized by V. Getautis's group at Kaunas University, with a focus on how cross-linking influences charge transport properties and disorder parameters. In addition, one of these cross-linkable HTMs was tested as a matrix in a BHJ system to evaluate its impact on overall device performance.

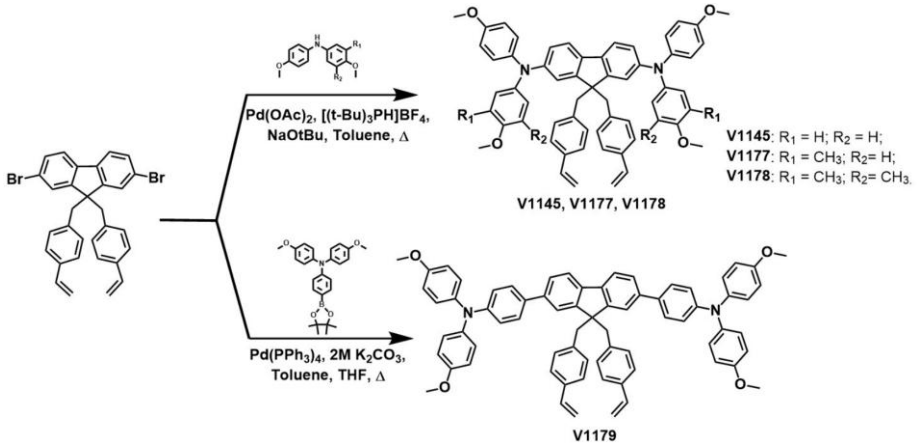

Fig. 21 Cross-linkable HTMs V1145, V1177, V1178, V1179 and their synthesis route.

The application of the fluorene-diphenylamine derivative V1145 has been previously reported in electrochromic devices and perovskite solar cells (PSCs). Considering that the introduction of methyl groups into the side phenyl moieties enhances hole drift mobility and that the presence of two methyl groups is more effective than a single one, V. Getautis group synthesized analogous derivatives with both methyl and additional phenyl groups to test their applicability in PSCs.

The Buchwald–Hartwig amination reaction was employed to synthesize new hole-transporting materials. Commercially available 4,4'-dimethoxydiphenylamine and 4-methoxy-N-(4-methoxyphenyl)-N-(4-(4,4,5,5-tetramethyl-1,3,2-dioxaborolan-2-yl)phenyl)aniline were used as precursors, while other intermediates were synthesized according to literature procedures.[97] These starting materials were coupled with 2,7-dibromo-9,9-bis(4-vinylbenzyl)-9H-fluorene, yielding the target compounds V1145, V1177, V1178, and V1179. Characterizations of target compounds are provided in the APPENDIX II.

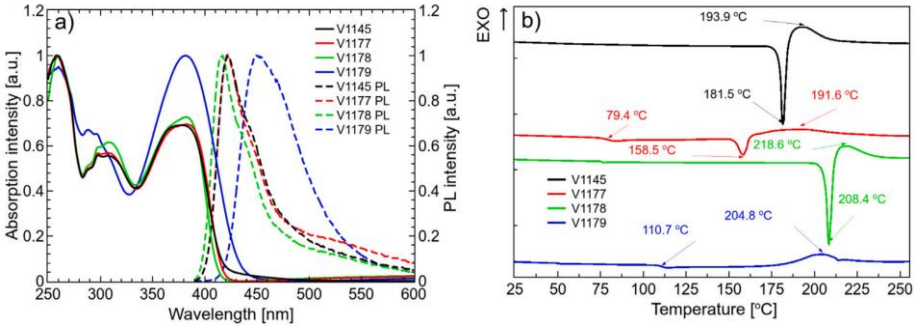

Fig. 22 (a) UV–Vis and photo-luminescence (PL) spectra; (b) DSC curves and melting, cross-linking and glass transition temperatures

UV–Vis and photoluminescence (PL) spectra were recorded from thin layers of the pristine hole-transporting materials (HTMs) (**Fig. 22a**). The absorption spectrum of V1145 shows a maximum at 378 nm, while a small redshift of 5 nm was observed for the derivative with additional linking phenyl groups, V1179. The methylated derivatives, V1177 and V1178, exhibited a shift of the absorption edge to shorter wavelengths, which could mean that methyl groups reduce the conjugation of the overall molecule. The spectra of V1177, V1178, and V1179 show a slight absorption edge in the visible region, suggesting a potential minor negative impact on solar cell performance.

Thermal stability and cross-linking potential of the target compounds were evaluated through differential scanning calorimetry (DSC) and

thermogravimetric analysis (TGA). In the first DSC heating cycle, no glass transition temperature (T_g) was detected for compounds V1145 and V1178 (**Fig. 22b**). However, melting points were observed at 181.5 °C for V1145 and 208.4 °C for V1178, followed by polymerization processes at 193.9 °C for V1145 and 218.6 °C for V1178. Glass transition temperatures were detected for V1177 (T_g = 79.4 °C) and V1179 (T_g = 110.7 °C). The melting point for V1177 was observed at 158.5 °C, indicating that this compound existed as a mixture of amorphous and crystalline states. Polymerization processes for V1177 and V1179 occurred at 191.6 °C and 204.8 °C, respectively. In the second heating cycle, no phase transitions were observed, confirming the formation of cross-linked polymers.

All synthesized materials demonstrated excellent thermal stability, with 5% weight loss (T_{d5}) temperatures around 400 °C: V1145 - 400 °C, V1177 - 396 °C, V1178 - 387 °C, and V1179 - 403 °C (APPENDIX II).

To demonstrate that vinyl bonds may be involved in polymerization reactions at elevated temperatures, V1145 was selected as a model material due to its two vinyl bonds. **Fig. 23** presents the 785-nm excited Raman spectra of the compound before and after thermal treatment. The spectrum before thermal treatment displays the characteristic C=C stretching mode (ν(C=C)) at around 1631 cm^{-1}.[98,99] In the high-frequency region, the =C–H stretching mode (ν(=C–H)) appears at 3012 cm^{-1}. The difference spectra reveal a temperature-induced decrease in the intensity of both bands, with positive-going features at 1633 and 3013 cm^{-1}.

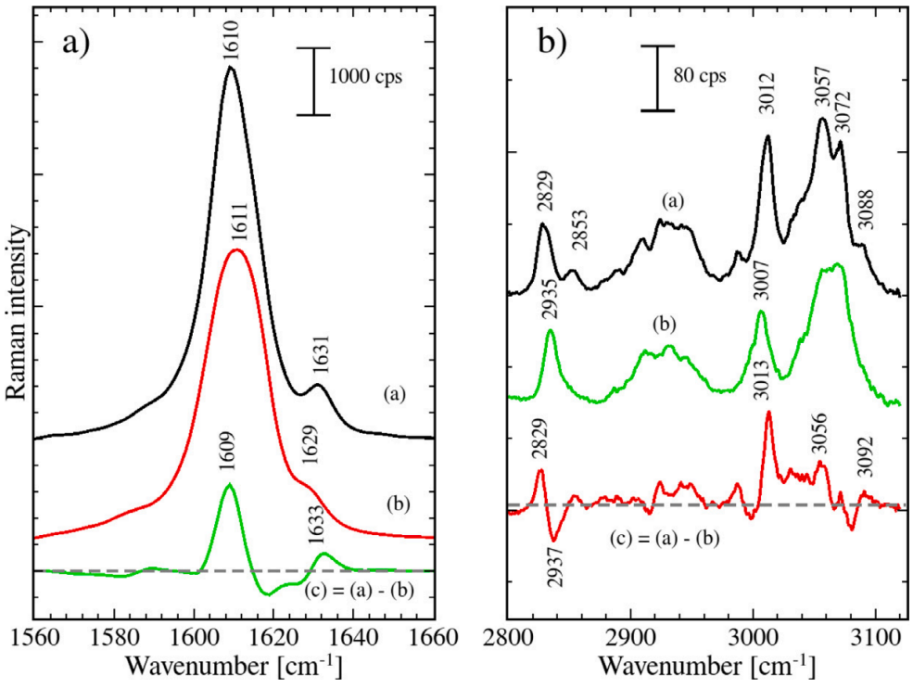

Fig. 23 Raman spectra of studied V1145 compound (a) before and (b) after 1h treatment at 200 ◦C in the spectral regions of (A) 1560–1670 cm^{-1} and (B) 2800–3120 cm^{-1}. Difference spectra (c)=(a)–(b) are also shown. The excitation wavelength is 785 nm (30 mW).

Based on the relative intensities of the 3012 cm^{-1} and 3007 cm^{-1} bands, the polymerization efficiency was estimated to be approximately 40% after 1 hour of cross-linking. The polymerization conversion efficiency of the remaining compounds was evaluated using UV–Vis spectra, with the results provided in APPENDIX II.

4.2.1. Disorder and charge transport in fluorene-based cross-linked hole transporting materials

In order to evaluate the cross-linking influence on charge transport properties, we measured hole mobility dependencies on electric field E under various temperatures in cross-linked and non-cross-linked materials, using the time-of-flight (TOF) method.

FTO substrates ($15 \times 25\ mm$) were sequentially sonicated in water, acetone, and isopropanol, after which $150\ \mu L$ of a $10\ mg\ mL^{-1}$ chlorobenzene solution of each HTM was drop-cast onto the cleaned slides. Wet films intended to remain uncross-linked were dried for 2 h at $20\ °C$ before silver contacts were

thermally evaporated, whereas films destined for cross-linking were first heated at their specific cross-linking temperature for 2 h and then given the same silver contacts. Charge-carrier mobility (μ) was measured by the time-of-flight (TOF) method between 190 and 297 K in a cryostat, using a multimode Nd:YAG laser for excitation.

TOF transients became more dispersive after cross-linking in all investigated materials, transit times are longer in cross-linked layers than in non-cross-linked ones. As an illustration of dispersive transients V1179 transient signals are provided in **Fig. 24**. More dispersive transient shapes and lower hole mobilities (**Fig. 25, Table 1**) indicate changes in molecular arrangement of HTM layers after cross-linking.

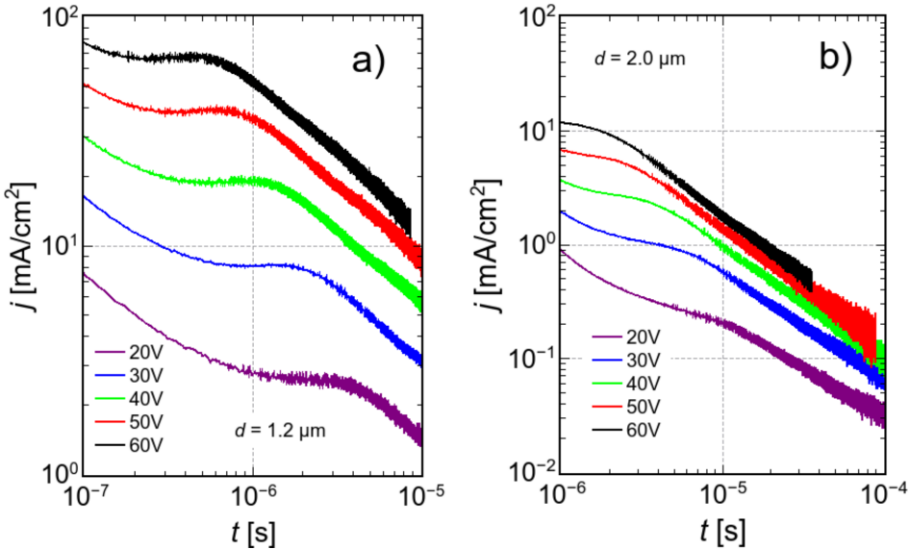

Fig. 24 Time-of-flight transients in V1179 a) non-cross-linked, b) cross-linked layers at room temperature.

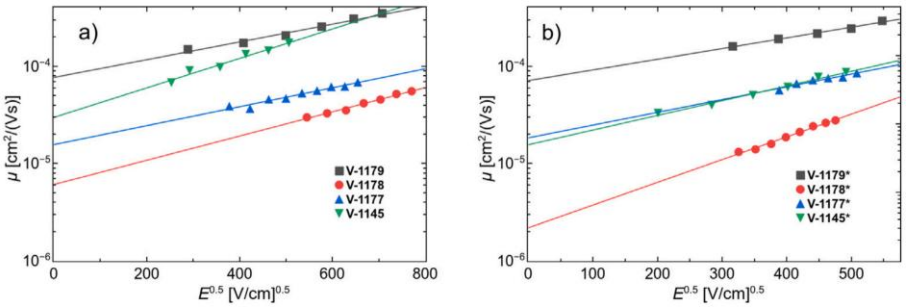

Fig. 25 Mobility µ versus electric field in a) non-cross-linked, b) cross-linked layers of V-1145, V1177, V1178, V1179 compounds.

If methyl groups are added to as radicals R1 and R2 (**Fig. 21**), hole drift mobility decreases (**Table 1**), what can be explained by lowered conjugation in a whole molecule and a smaller π-electron intersection between molecules in a layer (materials **V1145**, **V1177** and **V1178**). The additional phenyl group extends the conjugated system in a whole molecule, therefore **V1179** has the highest mobility values among other investigated materials.

A cross-linking influence on layer morphology was studied by measuring mobility dependencies on electric field under varying temperatures and estimating spatial and energetic disorder parameters. These dependencies are presented in **Fig. 26-27**. Spatial and energetic disorder parameters (σ and Σ) were calculated according to Bässler's formalism[100], which describes the relation between mobility, electric field and temperature:

$$\mu(E,T) = \mu_0 exp\left[-\left(\frac{2\sigma}{3kT}\right)^2\right] exp[C(\sigma^2 - \Sigma^2)E^{0.5}]$$

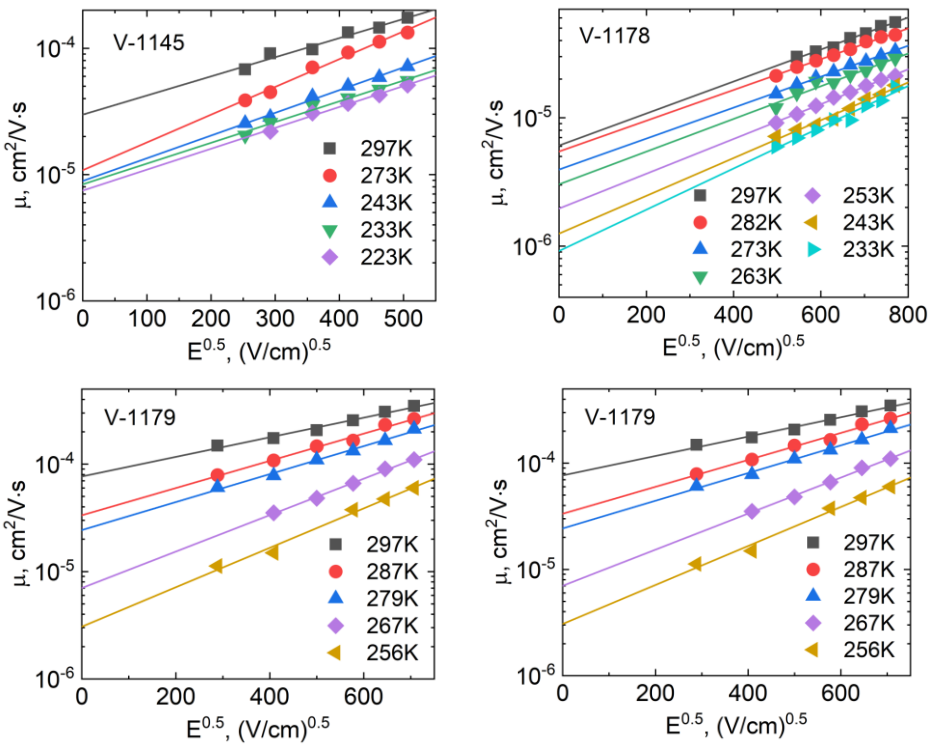

Fig. 26 Mobility μ versus electric field under varying temperatures in a regular V-1145, V1177, V1178, V1179.

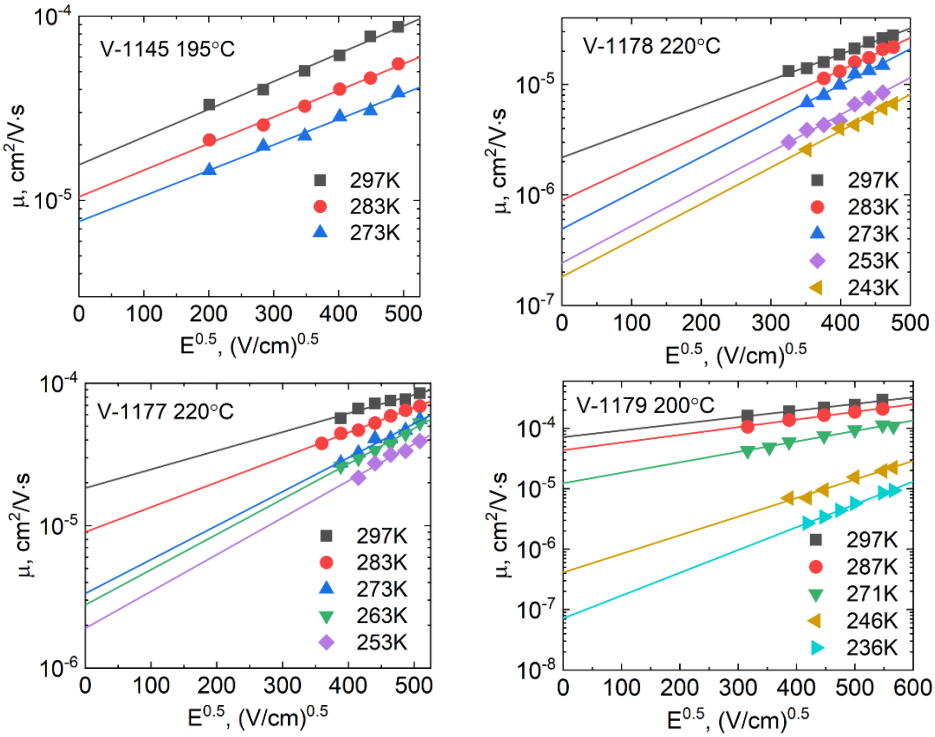

Fig. 27 Mobility μ versus electric field under varying temperatures in cross-linked V-1145, V1177, V1178, V1179.

Table 1. Energetic and spatial disorder parameters σ and Σ, hole mobility μ_0 at electric field $E = 0$, before and after cross-linking.

Material		σ, meV	Σ	μ_0, $cm^2V^{-1}s^{-1}$	σ*/σ	Σ*/Σ
V1145	Regular	22,51	1,69	$2{,}99\cdot10^{-5}$	3,26	2,74
	Cross-linked	61,72	5,52	$1{,}56\cdot10^{-5}$		
V1177	Regular	46,80	0,67	$1{,}56\cdot10^{-5}$	4,77	2,05
	Cross-linked	96,10	3,20	$1{,}84\cdot10^{-5}$		
V1178	Regular	56,30	1,37	$6{,}08\cdot10^{-6}$	1,34	1,5
	Cross-linked	84,98	1,85	$2{,}18\cdot10^{-6}$		
V1179	Regular	117,30	3,90	$7{,}67\cdot10^{-5}$	1,23	1,13
	Cross-linked	133,59	4,87	$7{,}12\cdot10^{-5}$		

Cross-linking process increased an energetic and spatial disorder (**Table 1**), thus hole drift mobility decreased in all investigated compounds. This can be observed in transients (**Fig. 24**) - after cross-linking, the signals are much more dispersive. Interestingly, an addition of CH_3 groups leads to a smaller change

in spatial disorder Σ after cross-linking when compared to **V1145** (**Table 1**). The same effect was observed in the case of additional phenyl groups in **V1179.**

The incorporation of cross-linkable materials into BHJs holds significant potential to enhance their long-term stability under ambient conditions. This approach can mitigate the effects of thermally activated phase separation, as well as minimize intrinsic and extrinsic degradation. To assess the suitability of cross-linkable materials for BHJ systems, **V1179** was employed as a donor material in blends with the PCBM acceptor at varying weight ratios. The time-of-flight (TOF) technique was used to evaluate the charge transport properties of the blends both before and after cross-linking.

TOF transients for the standard and cross-linked 1:1 weight ratio blends are shown in **Fig. 28** and **Fig. 29**, respectively. The corresponding mobility dependencies on the electric field are presented in **Fig. 30** and **Fig. 31**. **Table 2** summarizes the results, revealing that hole mobility decreased slightly after cross-linking, consistent with expectations due to increased disorder, as discussed earlier. This increase in disorder is also evident from the more dispersive hole transients shown in **Fig. 24**. Conversely, electron mobility increased after cross-linking, suggesting some degree of PCBM domain rearrangement. This was also replicated using different weight ratios which adds a degree of freedom in choosing an additional blend component.

These findings indicate that **V1179** is a promising candidate as a donor material for BHJ systems, providing a pathway to improved operational stability and performance.

Table 2. Charge carrier mobilities of V1179:PCBM blends before and after crosslinking.

V1179:PCBM			**V1179:PCBM cross-linked**		
wt.% ratio	μ_0^e, $cm^2/V \cdot s$	μ_0^h, $cm^2/V \cdot s$	**wt.% ratio**	μ_0^e, $cm^2/V \cdot s$	μ_0^h, $cm^2/V \cdot s$
1.5:1	$1.67 \cdot 10^{-4}$	$1.25 \cdot 10^{-4}$	**1.5:1**	$1.55 \cdot 10^{-3}$	$8.88 \cdot 10^{-5}$
1.25:1	$4.57 \cdot 10^{-4}$	$1.60 \cdot 10^{-4}$	**1.25:1**	$1.74 \cdot 10^{-3}$	$8.00 \cdot 10^{-5}$
1:1	$2.80 \cdot 10^{-3}$	$1.62 \cdot 10^{-4}$	**1:1**	$3.29 \cdot 10^{-3}$	$5.19 \cdot 10^{-5}$

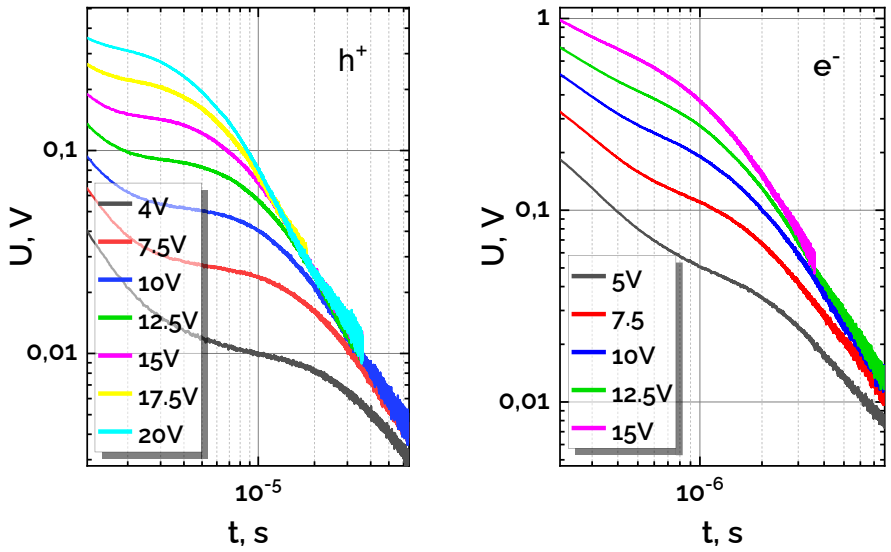

Fig. 28 Time-of-flight transients in 1:1 wt. % ratio of regular V1179:PCBM blend for holes and electrons.

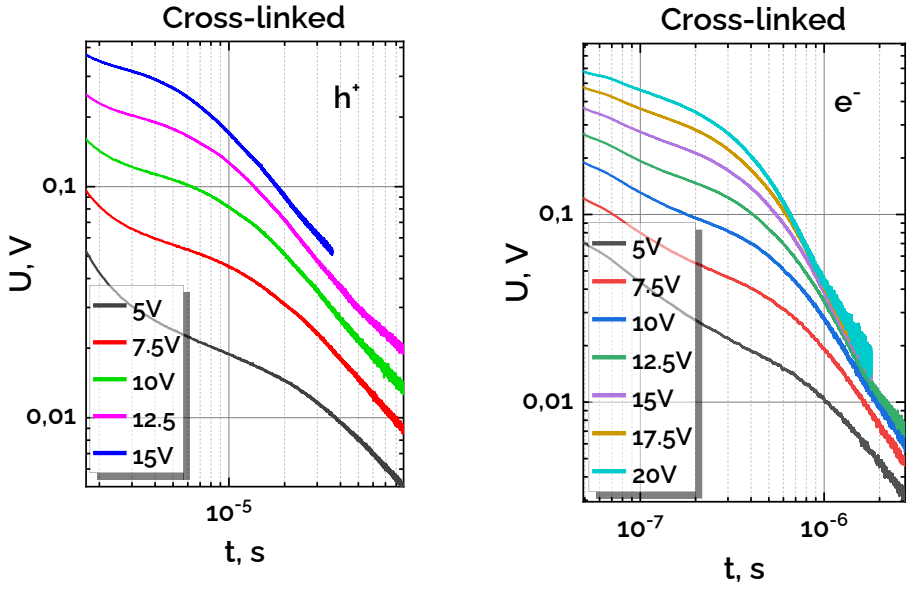

Fig. 29 Time-of-flight transients in 1:1 wt. % ratio of cross-linked V1179:PCBM blend for holes and electrons.

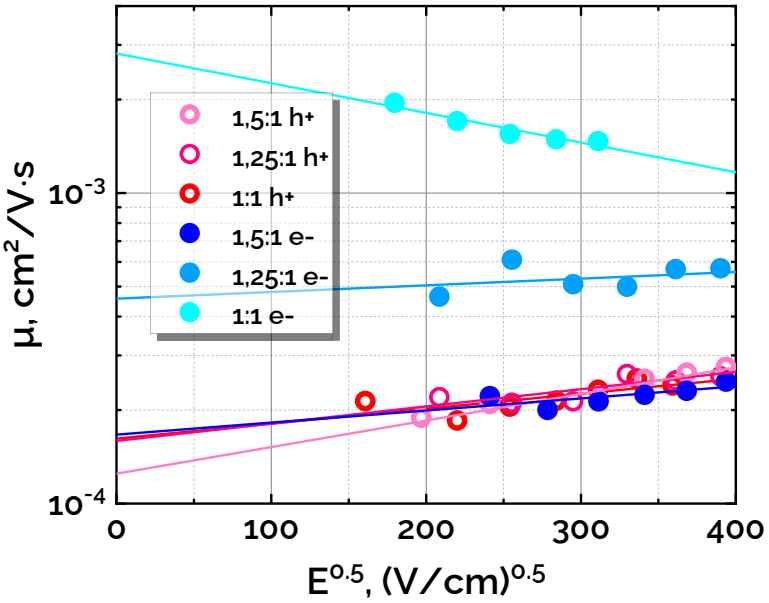

Fig. 30 Mobility μ versus electric field in regular V1179:PCBM blends.

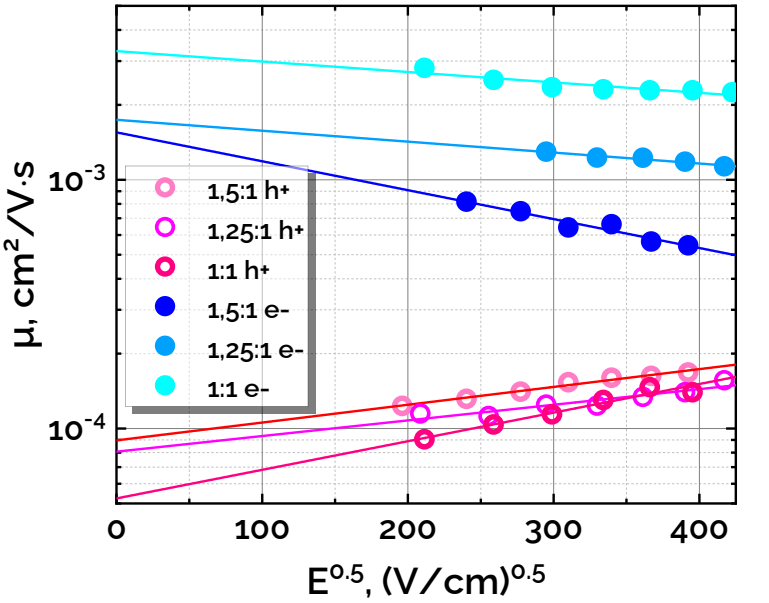

Fig. 31 Mobility μ versus electric field in cross-linked V1179:PCBM blends.

To summarize, four fluorene-based hole-transporting materials (HTMs) containing vinyl groups were successfully thermally cross-linked at temperatures above 200 °C, forming films that remained stable up to 400 °C. Cross-linking, commonly employed in organic electronics, helps lock the molecular architecture in place through covalent bonds, thereby improving morphological stability and offering potential as an isolating layer against external degradation factors—particularly valuable in inverted device structures. All four materials exhibited high hole drift mobilities and appropriate HOMO energy levels, underscoring their strong potential for use as HTMs in perovskite solar cells. Remarkably, the HOMO levels were essentially unchanged by cross-linking (APPENDIX II), with any slight variations falling within the margin of error. However, cross-linking did lead to a decrease in hole drift mobility and an increase in both spatial and energetic disorder. Although the introduction of $-CH_3$ groups did not significantly enhance the hole drift mobility as initially anticipated, it did help mitigate changes in spatial disorder (Σ) after cross-linking.
This leads to a conclusion that:

- Thermal polymerization of vinyl-functional fluorene cores locks film morphology and boosts thermal stability without shifting the HOMO level; the penalty is a modest drop in hole mobility and a rise in energetic/spatial disorder. The best-performing derivative bearing additional phenyl rings (V1179) showed just a 1.23-fold rise in energetic disorder and a 1.13-fold rise in spatial disorder.

Moreover, in a V1179:PCBM bulk heterojunction (BHJ) blend, V1179 served as a donor material without compromising electron or hole mobilities upon cross-linking. In fact, the cross-linked blend layer displayed enhanced electron mobility, possibly reflecting a rearrangement of PCBM domains. Taken together, these findings highlight the promise of cross-linkable fluorene-based HTMs for achieving stable, high-performance optoelectronic devices, while also offering an additional protective advantage against environmental degradation in inverted architectures. This lets us conclude that:

- In V1179:PCBM blends, cross-linking preserves—or even enhances—electron mobility while only slightly impairing hole transport, indicating that covalent locking need not compromise hole\electron mobility balance.

4.3. Fluorene-based bipolar charge transporting materials with balanced charge mobility

In this last section we focus on bipolar charge-transporting materials (CTMs). A key goal is to develop CTMs with balanced hole and electron mobilities because any imbalance can trigger space-charge effects, leading to accumulation of the slower carrier. This buildup screens the electric field and hinders the extraction of remaining carriers, thereby heightening recombination losses. If integrated into BHJs, such CTMs could improve charge separation and transport within the active layer. Accordingly, this section presents an investigation into novel fluorene-based CTMs, encompassing both quantum chemistry simulations (conducted by A. Gruodis) and a thorough analysis of their charge transport properties.

Generally, soluble and air-stable bipolar CTMs have quite complex structures and require expensive starting materials and/or elaborate multistep synthesis. V. Getautis group designed and synthesized air-stable and solution-processable fluorine-based bipolar materials **V1393, V1421, V1457, V1458, V1484,** and **V1485** (**Fig. 32**). These CTMs were obtained from inexpensive starting materials through simple reactions and possess electron transporting anthraquinone, 9-fluorenone, or 9-dicyanofluorenylidine with attached carbazolyl electron-donating moieties. The optical, thermal, and charge carrier transport properties of the synthesized CTMs were studied. The existence of possible conformers and excitation energies were calculated by the means of quantum chemistry simulations.

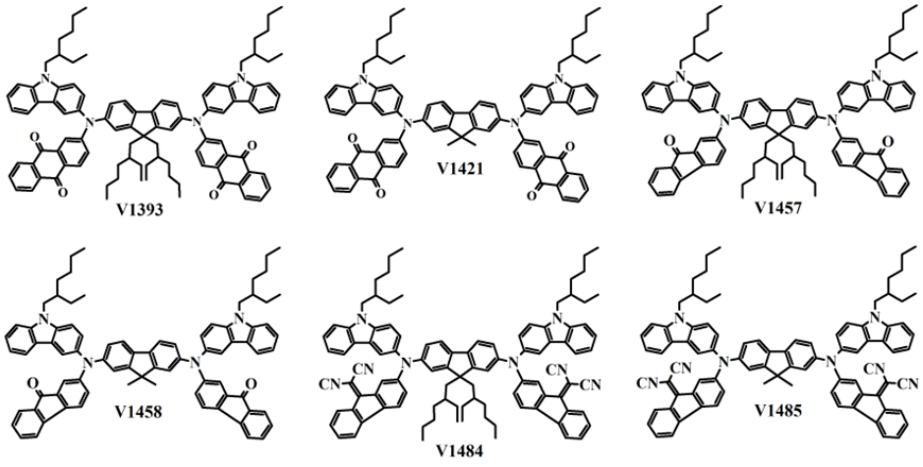

Fig. 32 Chemical structures of the synthesized bipolar compounds bearing different structural units.

Thermal stability of new bipolar molecules was evaluated by thermogravimetric analysis (TGA) in nitrogen atmosphere. As seen from **Fig. 33**, all bipolar compounds are thermally stable at temperatures higher than 400°C that is well above operating temperatures of most electronic devices.
The results of differential scanning calorimetry (DSC) measurements are shown in **Fig 34**. According to the DSC scans, the glass transition temperatures (T_g) were observed at 109 and 153 °C for **V1393** and **V1421**, respectively. Notably, the T_g of **V1457** and **V1458** are lower than those of their analogues with anthraquinone moieties (92°C for **V1457** and 133°C for **V1458**). The glass transition temperatures increased when the cyano groups were incorporated into the molecules (112°C for **V1484** and 161°C for **V1485**). Furthermore, as expected, all materials with longer alkyl side chains demonstrated lower glass transition temperatures than those of the ones with shorter alkyl chains. No endothermic peaks were observed during two heating cycles, what proves that all new materials are amorphous. It is preferable that new bipolar molecules would have an amorphous state in order to obtain good quality films.

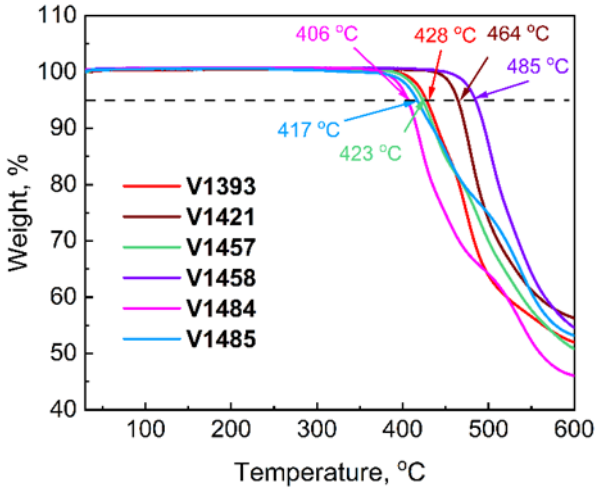

Fig. 33 TGA curves of new bipolar molecules.

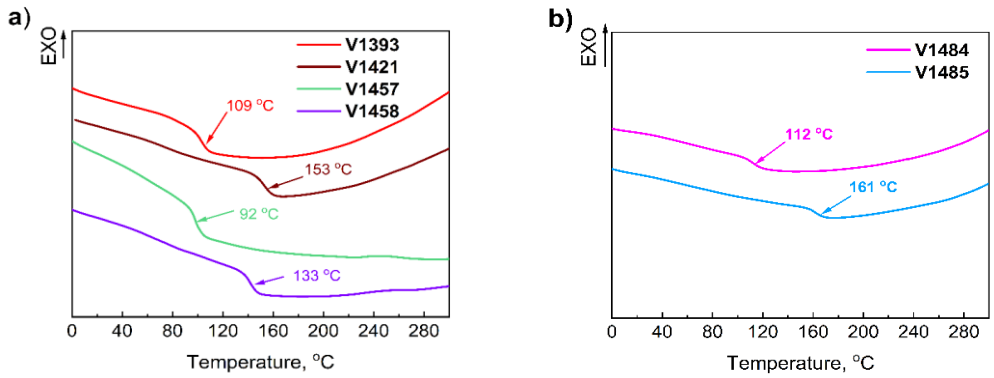

Fig. 34 DSC curves for the second run of the bipolar molecules bearing a) carbonyl groups (V1393, V1421, V1457 and V1458) and b) cyanoylidene moieties (V1484 and V1485) (heating rate of 10 °C min, N2 atmosphere).

4.3.1. Charge transport and recombination in fluorene-based bipolar charge transporting materials

A comparison of the UV–visible absorption spectra of the new HTMs recorded in THF solution and from solid films is shown in **Fig. 35**, and the corresponding data are listed in **Table 3**. In general, the spectra of all target compounds display not less than three absorption bands. As expected, the same group molecules, which structures differ in the length of the alkyl chains, present similar absorption profiles from 250 to 900 nm. The spectra of all new compounds display an intensive π–π* absorption bands at 270–450 nm, while the weak absorption band with maximum in the visible region has n-π* nature.

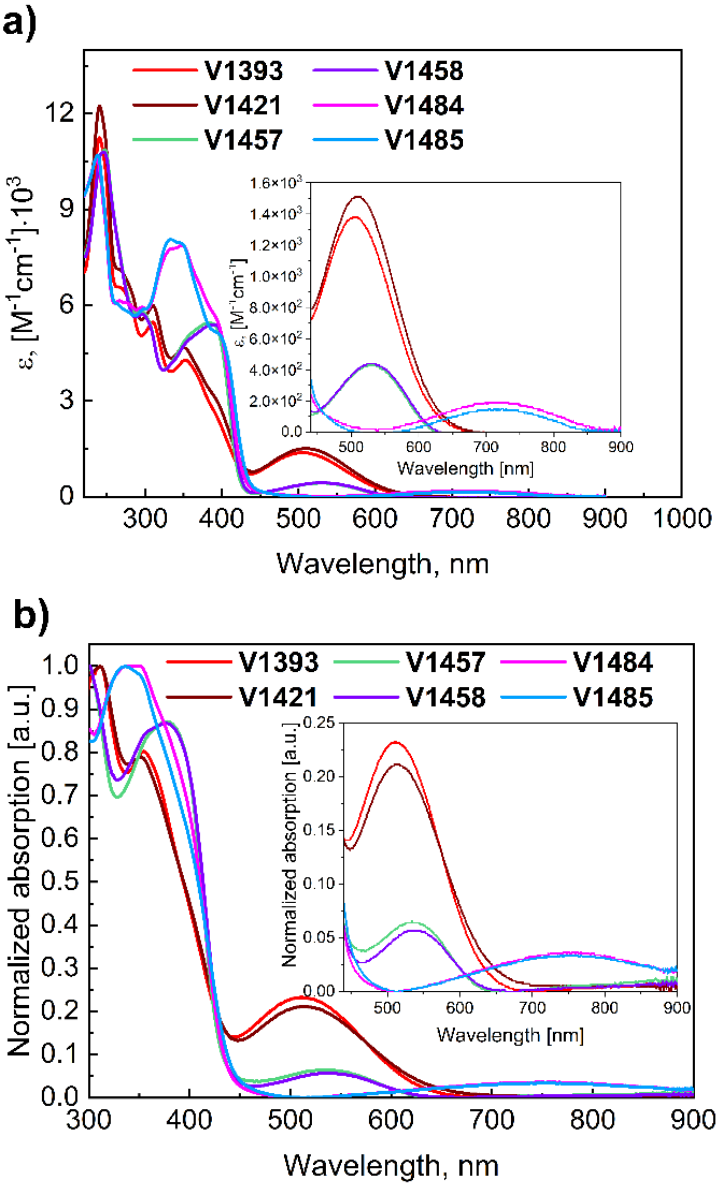

Fig. 35 UV-vis spectra of the target compounds from a) THF solutions (c=10-4 mol/l); b) solid films.

While comparing spectra of **V1393**, **V1421**, and **V1457**, **V1458** the red shifted absorption peaks can be detected. Stronger absorption for **V1393**, **V1421** around 510 nm is attributed to the presence of carbonyl groups. The same phenomenon was observed for **V1457** and **V1458**.

When compared to the solution samples, the absorption of film samples exhibits a minimal red shift (~3nm) (**Fig. 35b**), this might suggest weak interactions in solid phase. On the other hand, this shift could support the presence of aggregates even in low-concentration solutions as quantum chemistry calculations suggest that such intermolecular transitions were only feasible in dimer structures (APPENDIX III). The photoluminescence (PL) measurements were conducted on the solutions and solid layers of materials, but no observable emission was detected.

Table 3. a) UV−vis spectra were measured from thin layers; b) ionization energies of the films were measured using PESA; c), d) HOMO and LUMO energy levels were estimated from the CV measurements; e) hole mobility value at zero field strength; f) electron mobility value at zero field strength.

Compound	λ_{abs} [nm][a)]	I_p [eV][b)]	*HOMO* [eV][c)]	*LUMO* [eV][d)]	$\mu_{0\ \text{Hole}}$ [cm^2/Vs][e)]	$\mu_{0\ \text{Elec.}}$ [cm^2/Vs][f)]
V1393	311, 355, 512,	5.18	5.38	3.85	2.6×10^{-7}	4.6×10^{-9}
V1421	311, 352, 514	5.21	5.51	4.0	1.4×10^{-7}	1.1×10^{-9}
V1457	378, 534	5.02	5.34	3.97	3.9×10^{-7}	-
V1458	377, 537	5.02	5.46	4.09	9.2×10^{-8}	-
V1484	337, 346, 760	5.18	5.54	4.16	1.2×10^{-7}	1.0×10^{-8}
V1485	337, 750	5.16	5.42	4.09	2.8×10^{-8}	3.5×10^{-9}

The hole and electron mobility are a fundamental parameters when bipolar molecules are evaluated. To analyze the charge transport properties of novel compounds, xerographic time-of-flight measurements (XTOF) were employed; the transient signals are presented APPENDIX IV. The material solution (THF) was poured onto aluminum-coated glass plates. The sample was poured from a solution of pure substance. The layers were dried for 1 h at $60°C$. The thickness of the transport layer was measured with an optical microscope-interferometer. The drift mobility of electron holes (μ) was determined in electrophotographic mode at an electric field of $(0.1 \div 1) \cdot 10^6\ V/cm$. Charge carriers were generated at the layer surface by

illumination with nitrogen laser nanosecond pulses (λ=337 nm). These measurements were conducted in films of the pure compounds, and the obtained mobility dependencies on electrical field are presented in **Fig. 36**.

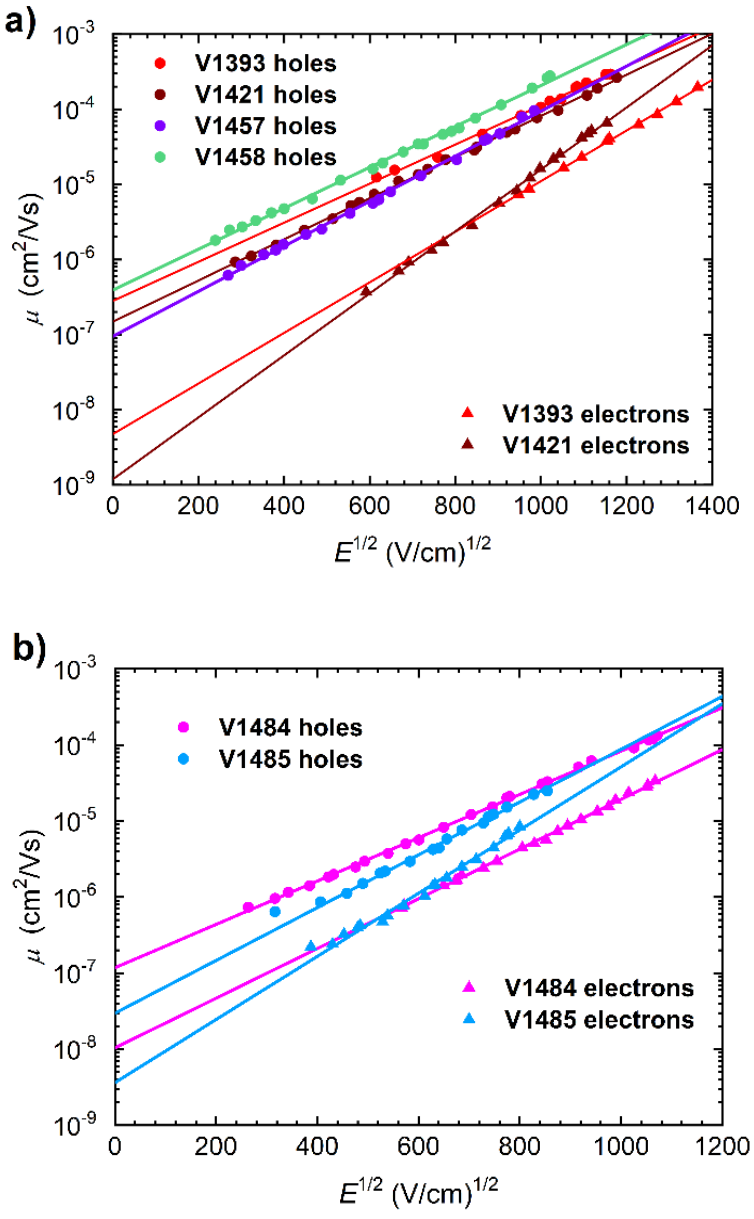

Fig. 36 Electric field dependencies of the new materials containing a) anthraquinone and fluorenone functional groups (**V1393**, **V1421**, **V1457**, and **V1458**) and b) cyanoylidene group (**V1484** and **V1485**).

The results have clearly indicated that molecules containing anthraquinone fragments (**V1393**, **V1421**) and cyanoylidene substituents (**V1484**, **V1485**) exhibit both negative and positive charge transport capabilities with hole mobility reaching values of one order of magnitude higher than those of electrons.

However, no electron-clear transients were obtained in compounds **V1457** and **V1458** bearing 9-fluorenone chromophores as electron acceptors. The only noticeable effect of longer alkyl chains (**V1393**, **V1457**, and **V1484**) was a slight improvement of hole mobilities at low electric fields, thus a case could be made that longer alkyl chains may be beneficial for more optimal molecular arrangement for charge transport.

Replacement of the keto groups with cyanoylidene groups resulted in decreased hole drift mobility and increased electron mobility. The most balanced charge mobility has been recorded in the bipolar molecules **V1484** and **V1485**, where the hole mobility is 1.2×10^{-7} cm^2 V^{-1} s^{-1}, and the electron mobility is 1.0×10^{-8} V^{-1} s^{-1} at near zero electric fields.

Photocurrent decay measurements were conducted to gain deeper insights into charge transport within the layers. Surface generation was employed by illumination with nitrogen laser nanosecond pulses ($\lambda = 355\,nm$), small photogenerated charge mode was used ($Q << CU$). We applied electrical field which was insufficient to facilitate the extraction of charge carriers from the layer (about $60\,kV/cm$, resulting kinetics were in the pre-transit region $t < t_{tr}$), causing photocurrent decay to be predominantly influenced by charge carrier trapping, detrapping, and recombination processes[101,102]. The resulting profiles were normalized to compare the photocurrent tail regions of decay (ranging from $2 \cdot 10^{-5}$ to $1 \cdot 10^{-4}$ s), which could be attributed to deep traps and recombination. The type of carriers observed was changed by changing the polarity of the applied voltage. In layers featuring anthraquinone fragments (**Fig. 37b**), the photocurrent decay profiles for both holes and electrons exhibit similar kinetics with minimal observable impact from additional alkyl groups. On the contrary, the most significant alterations in the slower decay region were observed when altering the length of the alkyl chains in compounds containing fluorenone groups (**V1458, V1457**) (**Fig. 37a**). The lengthening of the alkyl chains resulted in a reduced influence of trapping and detrapping on hole transport and increased recombination, as evidenced by the significantly lower hole mobilities observed in **V1458**. However, electron photocurrent decay seemed to exhibit only marginal sensitivity to the same alkyl chain modifications.

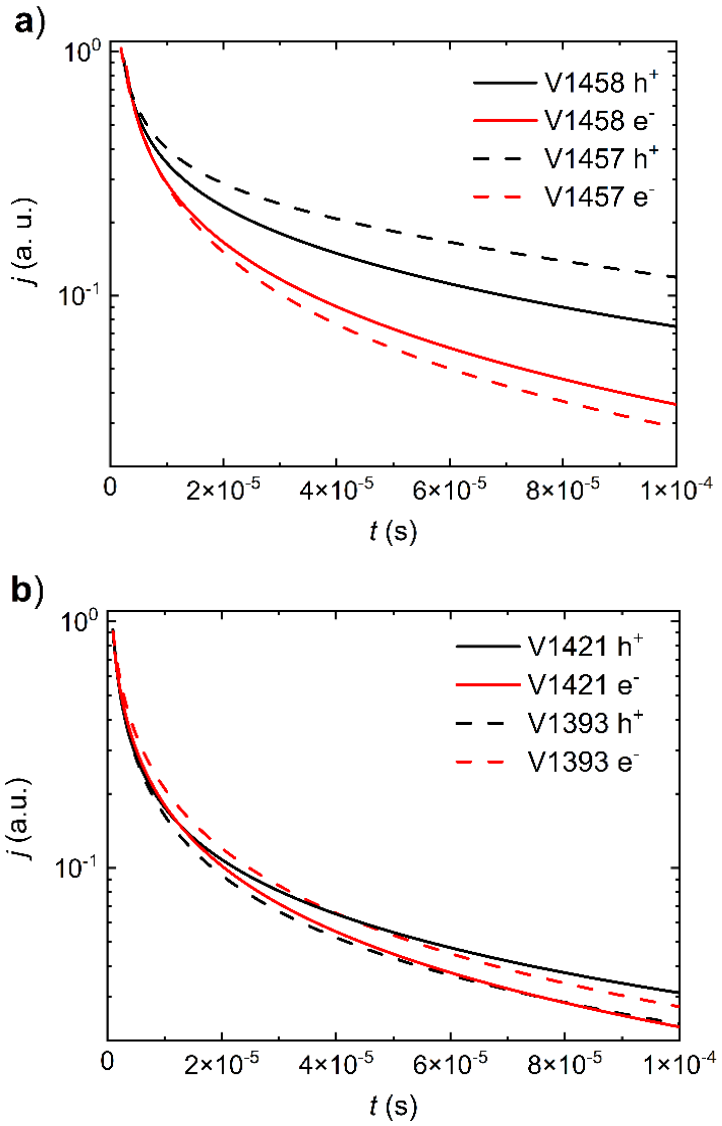

Fig. 37 Photocurrent decay profiles of compound films containing a) fluorenone functional groups (**V1457** and **V1458**) and b) anthraquinone groups (**V1393** and **V1421**).

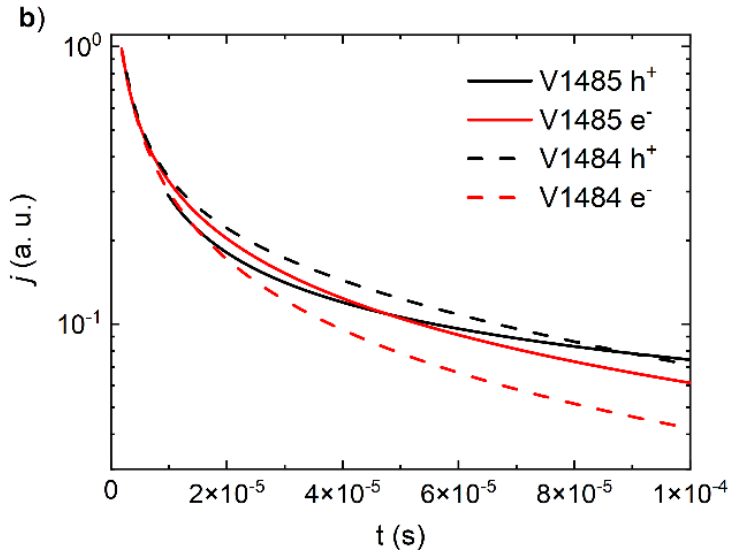

Figure 38. Photocurrent decay profile of compound film containing cyanoylidene fragments (**V1485** and **V1484**).

Compounds featuring cyanoylidine fragments (**V1484, V1485**) (**Fig. 38**) displayed a similar improvement when additional alkyl chains were introduced. This led to slower electron photocurrent decay alongside higher electron mobilities. These findings underscore the importance of additional alkyl groups in optimizing the molecular arrangement within the layer, subsequently enhancing charge carrier transport. Notably, the discernible differences in hole and electron current decays corroborate the discrepancies found in charge carrier mobilities.

In conclusion, new amorphous bipolar fluorene-based materials were developed, bearing anthraquinone, 9-fluorenone, or 9-dicyanofluorenylidine substituents, together with carbazolyl electron-donating moieties. These materials were synthesized via a straightforward route, and they exhibit good film-forming properties suitable for solution processing. Optical absorption measurements combined with quantum chemistry simulations confirm the formation of an intramolecular charge-transfer (CT) complex, alongside the emergence of probable dimer structures, specifically V-type and core-to-core type arrangements. Notably, multiple stable conformers are observed, as indicated by quantum chemistry calculations, reflecting the molecules' complex geometries.

All materials show hole mobilities on the order of 10^{-4} to 10^{-5} cm²/V·s, while compounds containing anthraquinone or 9-dicyanofluorenylidine moieties

possess electron mobilities roughly one order of magnitude lower. Interestingly, for the 9-fluorenone-based compounds, the electron transport is highly dispersive, and no clear photocurrent kink appears under measurement. These results let us conclude that:

- New amorphous fluorene derivatives with anthraquinone, 9-fluorenone, or dicyanofluorenylidene units form intramolecular charge-transfer complexes and exhibit balanced hole (10^{-4}–10^{-5} cm^2 V^{-1} s^{-1}) and electron transport suitable for implementations in organic devices.

CONCLUSIONS

- Extraction of injected charge carriers measurements map how bimolecular recombination velocity varies with carrier density in P3HT:PCBM bulk-heterojunctions, uncovering interfacial-state filling followed by an encounter-limited regime. Two distinct carrier-concentration regimes in P3HT:PCBM blend originate from traps at the polymer–fullerene interface, confirming that recombination is largely interfacial rather than encounter-limited.
- Recombination velocities measured with the EIC technique indicate that, in P3HT:PCBM films thicker than 400 nm, the additive 1,8-diiodooctane induces morphology changes that heighten recombination losses as the layer thickness increases.
- Thermal polymerization of vinyl-functional fluorene cores locks film morphology and boosts thermal stability without shifting the HOMO level; the penalty is a modest drop in hole mobility and a rise in energetic/spatial disorder. The best-performing derivative bearing additional phenyl rings (V1179) showed just a 1.23-fold rise in energetic disorder and a 1.13-fold rise in spatial disorder.
- In V1179:PCBM blends, cross-linking preserves—or even enhances—electron mobility while only slightly impairing hole transport, indicating that covalent locking need not compromise hole\electron mobility balance.
- New amorphous fluorene derivatives with anthraquinone, 9-fluorenone, or dicyanofluorenylidene units form intramolecular charge-transfer complexes and exhibit balanced hole (10^{-4}–10^{-5} cm^2 V^{-1} s^{-1}) and electron transport suitable for implementation in organic devices.

SANTRAUKA

1. Įvadas

Pastaraisiais metais pigių ir efektyvių fotovoltinių prietaisų kūrimas dažnai siejamas su organinėmis ir hibridinėmis struktūromis[1]. Jos pasižymi didžiuliu potencialu kaip alternatyva neorganiniams atitikmenims –prietaisai yra potencialiai pigūs, lengvai pagaminami ir neturi neigiamo poveikio aplinkai[2-5]. Organinių saulės elementų (OSC, ang. „organic solar cells“) srityje buvo padaryta didelė pažanga tobulinant aktyviąsias sluoksnio medžiagas, elektrodus, tarpinius sluoksnius bei diegiant inovatyvias įrenginių struktūras. Ypač pažymėtina pažanga aktyviosiose medžiagose – naujų donorinių ir akceptorinių medžiagų kūrimas reikšmingai pagerino OSC naudingumo koeficientą (PCE, ang.-„power conversion efficiency“).

Pirmosios kartos organiniai saulės elementai turėjo vieną aktyvų sluoksnį tarp dviejų skirtingo išlaisvinimo darbo elektrodų. Šių įrenginių PCE buvo mažesnis nei 0,1 %, nes eksitonų (elektrono–skylės porų) disociacija buvo neefektyvi, o rekombinacija – didelė. 1986 m. Tang pristatė dvisluoksnę heterosandūros struktūrą su donoro ir akceptoriaus medžiagomis[6], pasiekdamas apie 1 % PCE. Vis dėlto, ribotas donoro/akceptoriaus sandūros plotas trukdė efektyviam eksitonų difuzijos ir disociacijos procesui.

1995 m. Yu ir kt. pasiūlė tūrinės heterosandūros (BHJ, ang.-„bulk-heterojunction“) OSC koncepciją, kurioje aktyvusis sluoksnis buvo donoro ir akceptoriaus medžiagų mišinys[7]. Ši struktūra padidino sandūros plotą ir sumažino kelią, kurį eksitonai turi nudifunduoti iki sandūros (kur vyksta jų disociacija į laisvus krūvininkus), reikšmingai pagerindama įrenginių veikimą. Nuo to laiko OSC PCE pasiekė daugiau nei 18 %[8], tapdama viena iš perspektyviausių fotovoltinių technologijų.

Organinių saulės elementų veikimas glaudžiai susijęs su jų morfologija – medžiagų išsidėstymu ir pasiskirstymu aktyviajame sluoksnyje. Šios morfologijos supratimas ir valdymas yra itin svarbus siekiant optimizuoti įrenginio efektyvumą, stabilumą ir bendrą veikimą. Ideali morfologija turi užtikrinti efektyvų krūvio atskyrimą donoro–akceptoriaus sandūroje ir sudaryti nenutrūkstamus kelius krūvių pernašai į elektrodus, kartu sumažinant rekombinacijos nuostolius. Tūrinės heterosandūros struktūros gamybos sąlygos, tokios kaip tirpiklio pasirinkimas, atkaitinimo temperatūra ir nusodinimo metodai, daro didelę įtaką morfologijai[9–12]. Paprastesnėse sistemose šias sąlygas galima nesunkiai optimizuoti derinant bandymų–klaidų metodą su tikslingais eksperimentais. Tačiau sudėtingose daugiasluoksnėse sistemose optimizavimo galimybės susiaurėja, o įvairių komponentų tarpusavio sąveika apsunkina galutinio rezultato prognozavimą.

Iš pradžių OSC srityje dominavo dvinariai donoro ir akceptoriaus mišiniai, pvz., P3HT (polimerinis donoras) ir PCBM (fulereno akceptorius)[13]. Jau tuomet morfologijos valdymas buvo nemenkas iššūkis. Visgi tokių struktūrų morfologiją buvo galima pakankamai tiksliai įvertinti naudojant elektronų pralaidumo mikroskopiją (TEM, ang. „Transmission electron microscopy“)[14,15], atominių jėgų mikroskopiją (AFM ang.-„Atomic force microscopy“)[16] ir rentgeno spindulių difrakciją (XRD ang.-„X-ray diffraction“)[17]. Šie metodai leido tirti fazinę atskirtį, kristališkumą ir domenų grynumą, suteikdami žinių apie tai, kaip gamybos sąlygos siejasi su įrenginio veikimu.

Norint pasiekti dar didesnį efektyvumą, buvo pradėti kurti trinariai[18] ir keturnariai[19] mišiniai, įtraukiant papildomus donorinius ar akceptorinius komponentus. Trinarių BHJ strategija praplėtė šviesos sugerties spektrą panaudojant skirtingų sugerties juostų medžiagas[20]. Trečiasis komponentas taip pat gali sukurti energijos kaskados efektą, taip pagerindamas krūvių pernašą ir sumažindamas jų rekombinaciją[21]. Vis dėlto tokios sistemos yra daug sudėtingesnės morfologiškai, nes medžiagų tarpusavio sąveika priklauso nuo jų kristalizacijos tendencijų, tarpusavio maišymosi ir fazinio atsiskyrimo. Tam reikia pažangesnių tyrimo metodų ir teorinių modelių. Pavyzdžiui, TEM ir AFM suteikia aukštos raiškos paviršiaus morfologijos vaizdus[22], tačiau negali atskleisti vidinės sluoksnio struktūros. Todėl svarbiomis tapo tokios rentgeno sklaidos technikos kaip GIWAXS (ang.-„ grazing-incidence wide-angle X-ray scattering“) metodas[23,24]. Visgi šių duomenų interpretacija reikalauja gana sudėtingų modelių ir simuliacijų, nes didelis medžiagos kiekis apsunkina sklaidos analizę.

Be to, daugeliu atvejų kelių komponentų sistemos formuoja mišrias fazes su tarpusavyje persipynusiais tinklais. Tai apsunkina fazių identifikavimą įprastais vaizdiniais metodais. Tam pasitelkiami pažangūs metodai, tokie kaip rezonansinė minkštųjų rentgeno spindulių sklaida (RSoXS) ir elektronų tomografija[25], tačiau jie reikalauja specializuotos įrangos ir įgūdžių, todėl yra sunkiau prieinami.

OSC morfologija taip pat yra dinamiška – per savo gyvavimo trukmę įrenginio morfologija gali pakisti dėl šviesos, šilumos ar mechaninio poveikio. Tokiems pokyčiams stebėti būtinos in-situ stebėjimo metodikos, tokios kaip in-situ GIWAXS ar in-situ AFM, kurios leidžia stebėti realaus laiko morfologijos evoliuciją[26,27]. Šie metodai dar tik plėtojami ir dažnai turi ribotą laiko bei erdvinę skyrą.

Paini morfologija lemia ir sudėtingą krūvio pernašos ir rekombinacijos dinamiką mišiniuose su keliomis donoro-akceptoriaus sandūromis, įvairiais energetiniais lygmenimis ir skirtingomis medžiagų savybėmis. Šių mechanizmų identifikavimas ir kiekybinis vertinimas yra sudėtingas, ypač kai jie vyksta skirtingu metu ir skirtingose vietose sluoksnyje.

Net ir paprastose dvinarėse sistemose rekombinacijos kinetika yra netriviali – su keliomis laiko konstantomis, priklausomybėmis nuo krūvininkų tankio, temperatūros ir elektrinio lauko[28,29]. Tokia sudėtinga dinamika apsunkina kinetinių parametrų, tokių kaip rekombinacijos koeficientai ar krūvininkų gyvavimo trukmė, nustatymą iš eksperimentinių duomenų.

Dar viena reikšminga problema, apsunkinanti OSC kūrimą ir charakterizavimą – jų degradacija[30–32]. Ilgainiui, ypač veikiant aukštai temperatūrai, šviesai ar elektriniam laukui, aktyviojo sluoksnio medžiagos linkusios migruoti į termodinamiškai stabilesnę būseną. Kadangi sistema yra linkusi minimizuoti savo laisvąją energiją, tai dažnai veda prie donoro ir akceptoriaus fazių išsiskyrimo į didesnius, aiškiau apibrėžtus domenus. Tai sumažina sandūros paviršiaus plotą, blogina krūvio atskyrimą. Didėjant fazių atskyrimui, ankstesnė donoro ir akceptoriaus tinklo struktūra gali būti pažeista, o tai neigiamai paveikia krūvio pernašą. Galiausiai šie morfologiniai pokyčiai mažina krūvio atskyrimo našumą, didina rekombinaciją ir blogina OSC prietaiso veikimą. Naujos ir besivystančios skersaryšinamos krūvio pernašos medžiagos galėtų išspręsti šias problemas stabilizuojant mišinio sluoksnio morfologiją bei izoliuojant galutinį invertuotos struktūros prietaisą nuo aplinkos poveikio (deguonies ir drėgmės).

Be anksčiau minėtų problemų, OSC dažnai susideda iš kelių sluoksnių – aktyviojo sluoksnio, elektronų pernašos sluoksnio (ETL), skylių pernašos sluoksnio (HTL) ir elektrodų. Kiekvienas sluoksnis turi būti kruopščiai suprojektuotas, kad užtikrintų efektyvų krūvių surinkimą ir sumažintų nuostolius. Ypač svarbios yra sluoksnių sandūros – defektai ar sluoksnių persimaišymas gali stipriai pakenkti įrenginio veikimui. Šių daugiasluoksnių struktūrų sudėtingumas apsunkina gamybą ir padidina defektų riziką, o tai mažina gamybos efektyvumą ir patikimumą. Naujų bipolinių pernašos medžiagų panaudojimas saulės elemento architektūroje ar tiesiogiai tūrinės heterosandūros mišinyje galėtų padėti sumažinti daugiasluoksnės struktūros sudėtingumą ir pagerinti tarpsluoksnių medžiagų energetinį suderinamumą.

OSC sudėtingumas tiesiogiai lemia didesnes MTEP (mokslinių tyrimų ir eksperimentinės plėtros) sąnaudas. Reikia sudėtingos įrangos, pažangių medžiagų, daug bandymų – tai didina finansinę investicijų riziką. Įmonėms ir investuotojams tai gali tapti rimtu atgrasymu.

Norint įžiebti naują OSC vystymo ir komercializavimo etapą, būtina spręsti tokias problemas kaip fazių atskyrimas, sudėtinga morfologija ir brangūs tyrimo metodai, pasitelkiant naują pigių medžiagų sintezę, pažangias gamybos strategijas ir naujus tyrimo metodus.

1.1. Darbo tikslas ir uždaviniai

Ši disertacija apima kelias organinių saulės elementų (OSE) vystymo sritis – nuo krūvio pernašos ir rekombinacijos procesų bei jų charakterizavimo iki mišinių morfologijos ir jos stabilizavimo. Darbe tobulinami nusistovėję krūvio pernašos ir rekombinacijos analizės metodai, ypač siekiant nustatyti rekombinacijos spartos priklausomybę nuo krūvininkų koncentracijos bei morfologiją reguliuojančių priedų įtakos. Taip pat šioje disertacijoje dėmesys skiriamas skersaryšinamų skylių pernašos medžiagų (HTM, ang.-„Hole transporting material“) vystymui, kadangi jos gali atlikti dvigubą paskirtį OSC: tarnauti kaip izoliaciniai sluoksniai virš aktyviojo sluoksnio ir kaip matricos donorų–akceptorių mišiniams, taip apsaugant OSC nuo morfologinės degradacijos eksploatacijos metu.

Be to, disertacijoje tiriamos naujos fluoreno pagrindo bipolinės krūvio pernašos medžiagos, pasižyminčios subalansuotu skylių ir elektronų judriu. Tokios medžiagos gali būti naudojamos organiniuose fotovoltiniuose įrenginiuose bei donorų–akceptorių mišiniuose, siekiant optimizuoti krūvio pernašą ir pagerinti bendrą prietaiso našumą.

Siekiant nurodytų tikslų, atliktos šios užduotys:

• Įvertinti rekombinacijos greičio priklausomybę nuo krūvininkų koncentracijos poli(3-heksiltiofeno-2,5-diilo) (P3HT) ir [6,6]-fenil-C_{61} sviesto rūgšties metilo esterio (PCBM) tūrinėse heterosandūrose, taikant skaitmeninius metodus, injektuotų krūvininkų ekstrakcijos metodą (EIC, ang.-„Extraction of injected charge carriers“) ir lėkio trukmės (TOF, ang.-„Time-of-flight“) metodiką.

• Nustatyti rekombinacijos greičio priklausomybę nuo P3HT:PCBM heterosandūros sluoksnio storio su 1,8-diiodooktano (DIO) priedu ir be jo, naudojant skaitmeninius metodus, EIC ir TOF.

• Ištirti kryžminės polimerizacijos įtaka krūvio pernašai bei erdvinei ir energetinei netvarkai naujai susintetintose fluoreno pagrindo HTM.

• Charakterizuoti naujas amorfines fluoreno pagrindo bipolines krūvio pernašos medžiagas, turinčias antrachinono, 9-fluorenono ir 9-dicianfluorenilideno grupes.

1.2. Mokslinis naujumas

• Pirmą kartą buvo taikytas injektuotų krūvininkų ekstrakcijos (EIC) metodas kartu su lėkio trukmės metodu (TOF), siekiant kiekybiškai įvertinti rekombinacijos spartos priklausomybę nuo krūvininkų koncentracijos ir tūrinės heterosandūros storio. Šis metodas leido unikaliu būdu nustatyti dvi-komponentę rekombinacijos greičio priklausomybę nuo krūvininkų koncentracijos, kurią lemia tarpfazinės būsenos. Taip pat buvo parodyta, kaip

DIO sukelti morfologiniai pokyčiai lemia rekombinacijos greičio kitimą didėjant sluoksnio storiui. Šis subtilus rekombinacijos dinamikos supratimas, ypač storesniuose mėginiuose, kur DIO, atrodo, padidina rekombinacijos nuostolius, suteikia svarbių įžvalgų, kaip optimizuoti BHJ saulės elementų veikimą kontroliuojant apdorojimo sąlygas ir morfologiją. Tai yra reikšmingas ir naujas indėlis į organinių fotovoltinių technologijų sritį.

• Naujos fluoreno pagrindo skersaryšinamos skylių pernašos medžiagos, turinčios vinilo grupes, kurios yra termiškai polimerizuojamos temperatūrose virš 200 °C. Nustatyta, kad kryžminės polimerizacijos procesas reikšmingai pagerina šių medžiagų terminį ir morfologinį stabilumą, neturėdamas reikšmingos įtakos jų energetiniams lygmenims ir elektrinėms savybėms. Šis rezultatas turi perspektyvos išspręsti vieną iš svarbiausių OSC technologijos iššūkių – poreikį HTM medžiagoms, kurios būtų ne tik našios, bet ir užtikrintų ilgalaikį saulės elementų stabilumą.

• Naujos fluoreno pagrindo bipolinės krūvio pernašos medžiagos. Šios medžiagos išsiskiria atsparumu orui ir galimybe apdirbti iš tirpalo – savybėmis, itin svarbiomis praktiniam taikymui organiniuose elektroniniuose įrenginiuose. Naujovė slypi elektronus pernešančių antrachinono, 9-fluorenono ir 9-dicianfluorenilideno grupių derinyje su karbazolio tipo skylių donorinėmis grupėmis, dėl ko gaunamos medžiagos su subalansuota skylių ir elektronų pernaša. Skirtingai nuo daugelio krūvio pernašos medžiagų (CTM, ang.-„Charge transporting material“), kurių sintezė sudėtinga ir reikalauja brangių pradinių medžiagų, šie nauji junginiai sintetinami paprastais metodais, todėl jie yra ir inovatyvūs, ir praktiški.

1.3. Ginamieji teiginiai

• Injektuotų krūvininkų ekstrakcijos (EIC) metodas leidžia nustatyti rekombinacijos spartos priklausomybę nuo krūvininkų koncentracijos P3HT:PCBM tūrinių heterosandūrų prietaisuose, suteikdamas įžvalgų apie krūvininkų rekombinacijos dinamiką organiniuose saulės elementuose.

• Tarpfazinių būsenų užpildymas P3HT:PCBM tūrinėse heterosandūrose gali būti ištirtas pasitelkus EIC metodą, analizuojant rekombinacinės spartos priklausomybę nuo krūvininkų koncentracijos.

• EIC metodas gali atskleisti, kaip 1,8-dijodooktano priedo sukelti morfologiniai pokyčiai P3HT:PCBM tūrinėje heterosandūroje gali sukelti rekombinacijos spartos pokyčius didėjant sluoksnio storiui.

• Naujose fluoreno pagrindo skylių pernašos medžiagose su vinilo grupėmis skersaryšinimas pagerina terminį ir morfologinį stabilumą su nežymiais elektroninių savybių pokyčiais.

• Pigios stabilios amorfinės fluoreno pagrindo bipolinės krūvio pernašos medžiagos, turinčios antrachinono ir 9-fluorenono elektronus pernešančias

grupes, pasižymi subalansuotu skylių ir elektronų judrumu. Šis balansas yra itin svarbus optimizuojant organinių elektroninių prietaisų veikimą, ypač siekiant efektyvios krūvio pernašos.

1.4. Autoriaus indėlis

Autorius atliko išsamius krūvininkų judrio matavimus, taikydamas lėkio trukmės (TOF) metodą tiek tūrinės heterosandūros mišiniams, tiek skersaryšinamoms ir bipolinėms krūvio pernašos medžiagoms. Be to, autorius vykdė injektuotų krūvininkų ekstrakcijos (EIC) matavimus, siekdamas įvertinti krūvio pernašos dinamiką šiose medžiagose. Autorius taip pat buvo atsakingas už visų eksperimentinių mėginių paruošimą EIC ir TOF analizei – tai apėmė tirpalų ir mišinių paruošimą, TiO_2 blokuojančio sluoksnio purškimą, aktyviojo ir tarpinių sluoksnių nusodinimą lašiniu metodu bei nusodinimo ant besisukančio padėklo būdu, taip pat elektrodų nusodinimą.
Autorius dalyvavo rezultatų aptarimuose ir prisidėjo prie susijusių mokslinių publikacijų rengimo. Be to, jis atliko eksperimentinių duomenų analizę ir parašė šią disertaciją užtikrindamas, kad visa informacija, gauta iš išorinių šaltinių, būtų tinkamai cituojama.
KTU (Kauno technologijos universiteto) V. Getaučio grupė susintetino skersaryšinamas skylių pernašos ir bipolines krūvio pernašos medžiagas bei pateikė atitinkamus TGA, DSC, Ramano ir CV duomenis.
K. Genevičius parašė ir suteikė FDM modeliavimo kodą bei padėjo interpretuoti simuliuotų kinetikų duomenis.
A. Gruodis atliko kvantinės chemijos skaičiavimus bipolinės krūvio pernašos molekulėms ir jų dimerams.

2. Literatūros apžvalga

Organiniai saulės elementai iš esmės skiriasi nuo neorganinių saulės elementų savo šviesos vertimo į elektros energiją mechanizmais. Organinių medžiagų žemesnė dielektrinė konstanta lemia stipriai surištų elektronų ir skylių porų, vadinamų eksitonais, susidarymą, todėl reikalingos specialios architektūros efektyviam krūvių atskyrimui. Tūrinės heterosandūros struktūros, kuriose donoro ir akceptoriaus medžiagos sudaro nanometrinį tinklą, efektyviai sprendžia šią problemą, maksimaliai padidindamos sandūros paviršiaus plotą ir ženkliai pagerindamos eksitonų skilimą į laisvus krūvininkus. Tačiau OSC krūvininkų pernaša vyksta peršokant tarp lokalizuotų molekulinių būsenų – tai mažiau efektyvus mechanizmas, palyginus su juostine pernaša neorganiniuose puslaidininkiuose, dėl ko didėja rekombinacijos nuostoliai.

Plačiai ištyrinėta P3HT:PCBM sistema iliustruoja esminius BHJ iššūkius ir jų sprendimus. Optimalus P3HT:PCBM santykis, dažniausiai artimas 1:1 pagal mases, užtikrina subalansuotą elektronų ir skylių judrį. Atkaitinimo procedūra pagerina morfologiją, didindama P3HT kristališkumą ir skatindama PCBM agregaciją, taip pagerindama eksitonų išskyrimą ir laisvų krūvininkų judrį. Alternatyvūs metodai, tokie kaip sluoksnio laikymas tirpiklio garuose, leidžia papildomai kontroliuoti morfologiją ir yra naudingas lanksčiųjų elementų gamyboje. Priedas 1,8-dijodooktanas (DIO) padeda sureguliuoti fazių atskyrimą ir kristališkumą, paveikdamas tirpiklio garavimo greitį, taip ženkliai pagerindamas prietaisų veiką dėl efektyvesnės krūvio generacijos ir mažesnės rekombinacijos.

Nepaisant pažangos, P3HT:PCBM pagrindu pagamintų elementų efektyvumas pasiekė plato ties maždaug 3,5 %, kadangi yra ribojamas vidinių veiksnių, tokių kaip ribotas sugerties spektras, vidutinis krūvininkų judrumas ir morfologijos jautrumas gamybos sąlygoms. Stabilumas išlieka dideliu iššūkiu dėl vidinių degradacijos mechanizmų (morfologinio nestabilumo, cheminės degradacijos ir tarpinių sluoksnių korozijos) bei išorinių veiksnių (deguonies, drėgmės, ultravioletinės spinduliuotės ir temperatūros pokyčių poveikio). Siekiant sumažinti šiuos efektus, taikomos invertuotos struktūros, pažangūs hermetizavimo metodai, pvz., hibridiniai barjeriniai sluoksniai ir skersaryšinamos medžiagos, gerinančios morfologinį ir tarpsluoksnių stabilumą.

OSC rekombinacijos dinamika yra ypač sudėtinga. Gimiringų krūvininkų porų rekombinacija vyksta, kai stipriai surišta elektronų ir skylių pora rekombinuoja dar prieš atsiskirdama, o neporinė rekombinacija apima skirtingų eksitonų sugeneruotus laisvus krūvininkus, kuriems egzistuoja keli rekombinacijos keliai. Bimolekulinė rekombinacija, aprašyta Langevino teorijos, stipriai priklauso nuo krūvininkų judrumo ir dielektrinės konstantos. Tačiau realiuose prietaisuose dažnai stebima sumažinta Langevino

rekombinacija dėl morfologijos optimizavimo, energetinės netvarkos ir prilipimo būsenų, mažinančių krūvininkų rekombinacijos tikimybę.
Sudėtingi charakterizavimo metodai, tokie kaip laikinės absorbcijos spektroskopija, laikinės fotoįtampos ir fotostrovės matavimai bei photo-CELIV metodas, yra esminiai analizuojant krūvininkų dinamiką. Kiekvienas metodas turi savo privalumų ir trūkumų, todėl jų derinys yra būtinas siekiant tiksliai suprasti rekombinacijos mechanizmus.
Naujausi tyrimai pabrėžia nefulereninių akceptorių, tokių kaip ITIC ir Y6, svarbą, nes jie pasižymi platesniu sugerties spektru, geresniu energinių lygmenų suderinamumu, didesniu kristališkumu ir mažesniu energetiniu netvarkingumu, lyginant su tradiciniais fulerenais. Šios savybės ženkliai sumažina rekombinacijos nuostolius, pagerindamos bendrą OSC veikimą. Toliau vykdomi tyrimai pažangių trinarių ir keturnarių sistemų, naujų polimerų ir NFA srityse gerina efektyvumą, tačiau gilesnis fundamentinių procesų supratimas išlieka esminiu ateities proveržiams.

3. Metodikos

3.1. Lėkio trukmės metodas (TOF)

Lėkio trukmės metodas (TOF, ang.-„Time-of-fight“), naudojamas krūvininkų judriui ir bimolekulinės rekombinacijos koeficiento tyrimams, sukurtas R.G. Keplerio mažo dreifinio judrio amorfinėms medžiagoms tirti, išliko plačiai naudojamas dėl savo paprastumo. Metodas pagrįstas fotogeneruotų krūvininkų dreifo stebėjimu per visą bandinio storį, veikiant pastoviam elektriniam laukui.

Įprastame TOF eksperimente prie mažo laidumo bandinio, turinčio bent vieną blokuojantį kontaktą, prijungiama įtampa užtvarine kryptimi. Trumpu šviesos impulsu fotogeneruojami krūvininkai, kurių kiekis turi neviršyti krūvio, sukaupto ant bandinio elektrodų ($Q_0 \ll CU$). Sugeneruoti krūvininkai pradeda dreifuoti prijungto elektrinio lauko kryptimi. Atitinkamo ženklo krūvininkai, keliaudami per viso bandinio storį, generuoja srovę. Jiems pasiekus priešingo ženklo elektrodą, srovė pradeda staigiai kristi. O priešingo ženklo krūvininkai juda prie kito (apšviesto) elektrodo, kur jie greitai surekombinuoja. Esant stipriai sugerčiai, šių krūvininkų dreifo kelias yra gana trumpas ir jie įtakos srovės kinetikai neturi. Stebimas krūvininkų tranzito laikas leidžia apskaičiuoti jų judrį naudojantis šia išraiška:

$$\mu = \frac{d^2}{U t_{tr}}\,, \tag{3.1}$$

kur d yra bandinio storis, o U yra prijungta prie bandinio įtampa.

Apskaičiavus judrį, galima įvertinti Langevino rekombinacijos koeficientą B_L:

$$B_L = \frac{e(\mu_e + \mu_h)}{\varepsilon}, \tag{3.2}$$

čia μ_e ir μ_h - elektronų ir skylių judriai, e – elementarusis krūvis, ε-medžiagos dielektrinė konstanta.

Norint užtikrinti tikslius matavimus, TOF metode turi būti tenkinamos kelios sąlygos:

- Elektrinis laukas bandinyje turi būti pastovus ir vienalytis, t.y. $t_d > RC$, kur R yra apkrovos varža, o C – bandinio talpa, t_d – šviesos impulso uždelsimo trukmė.
- Medžiaga turi būti mažo laidumo, kad pusiausvyriniai krūvininkai neiškraipytų elektrinio lauko (Maksvelo relaksacijos trukmė $\tau_\sigma = \frac{\varepsilon\varepsilon_0}{\sigma} > t_d + t_{tr}$, kur σ – medžiagos laidumas).
- Krūvininkai turi pasiekti priešingo ženklo elektrodą prieš surekombinuodami ($\mu\tau E > d$, čia τ – krūvininkų gyvavimo trukmė, E – elektrinio lauko stipris).

Egzistuoja keli TOF režimai: diferencialinis ($RC < t_{tr}$) ir integralinis ($RC > t_{tr}$) (**Fig. 10**). Norint nustatyti srovę kuriančių krūvininkų tipą, turi būti tenkinama ši sąlyga:

$$\alpha d \gg 1, \tag{3.3}$$

kur α – sugerties koeficientas.

Kai fotogeneruotų krūvininkų tankis tampa artimas ar viršija CU, sistema pereina į krūvio perturbuotą režimą ($Q \approx CU$) arba į erdvinio krūvio ribotos srovės režimą (SCLC) ($Q \gg CU$). SCLC režime judantys krūvininkai ekranuoja elektrinį lauką už savęs, taip koncentruodami ir sustiprindami elektrinį lauką mažesniame tūryje. Dėl šios priežasties krūvininkų paketas pasiekia priešingą elektrodą greičiau nei per tranzito trukmę.

Plonuose bandiniuose ($\alpha d \leq 1$), integriniame režime ($RC > t_{tr}$), fotogeneruotų krūvininkų tankis laikui bėgant mažėja dėl monomolekulinės rekombinacijos:

$$\frac{dn}{dt} = -\frac{n}{\tau}, \quad n(t,x) = \frac{L\alpha}{e} e^{-\alpha x} e^{-\frac{t}{\tau}}, \tag{3.4}$$

čia L – šviesos intensyvumas ($\frac{C}{cm^2}$).

Esant intensyviai lazerio spinduliuotei, monomolekulinė rekombinacija tampa nereikšminga, pradeda dominuoti bimolekulinė rekombinacija, kuri seka kvadratinę priklausomybę nuo krūvininkų tankio:

$$\frac{dn}{dt} = -Bn^2 \tag{3.5}$$

Suintegravus, per visą bandinio storį gaunamas bendras ištrauktų krūvininkų skaičius:

$$N(t) = \frac{1}{Bt\alpha}\left(\alpha d - \ln\left(BtL\alpha + e^{\alpha d}\right) + \ln(BtL\alpha + 1)\right) \tag{3.6}$$

Esant didelėms L reikšmėms, bendra ištrauktų krūvininkų skaičiaus išraiška supaprastėja:

$$N(t) = \frac{d}{Bt} \tag{3.7}$$

Bimolekulinės rekombinacijos koeficientas B gali būti apskaičiuojamas iš ekstracijos trukmės t_e ir srovės integralo (ištraukto krūvio):

$$B = \frac{ed}{t_e \int_0^\infty j\, dt}, \tag{3.8}$$

o jo santykis su Langevino rekombinacijos koeficientu išreiškiamas:

$$\frac{B}{B_L} = \frac{CU}{Q}\frac{t_{tr}}{t_e}. \tag{3.9}$$

3.2. Injektuotų krūvininkų ekstrakcijos metodas (EIC)

Injektuotų krūvininkų ekstrakcijos metodas šiame darbe buvo taikytas tirti rekombinacijos spartą υ, matuojant ištraukto krūvio Q priklausomybę nuo injekcinės j_{in} srovės stiprio:

$$\upsilon = \frac{2kT\varepsilon\varepsilon_0 j_{in}}{eQ^2}$$

Nors EIC metodas įprastai taikomas dvisluoksnėse heterosandūrose, kuriose injektuojamų krūvininkų srovė yra apsprendžiama rekombinacijos sandūros plokštumoje, šį metodą galima pritaikyti ir BHJ sistemoje, kur donorinės ir akceptorinės fazės sudaro trimatį tinklą ir rekombinacija vyksta per visą sluoksnio storį. Šiuo atveju υ laikome efektyviu, per visa storį suvidurkintu rekombinacijos greičiu.

Jei injekcinė srovė būtų ribojama monomolekulinės rekombinacijos, tuomet:

$$j_{in} \propto e\frac{n(x)}{\tau} \propto en(x)\upsilon, \tag{3.10}$$

čia rekombinacijos sparta nepriklauso nuo krūvininkų tankio ir krūvininkų gyvavimo trukmė τ yra atvirkščiai proporcinga υ. Esant bimolekulinei rekombinacijai:

$$j_{in} \propto e\beta n(x)^2\,, \tag{3.11}$$

rekombinacinės spartos υ ir bimolekulinės rekombinacijos koeficientas β yra tiesiogiai proporcingi:

$$\beta \propto \frac{\upsilon}{n(x)} \propto \frac{\upsilon}{Q}\ . \tag{3.12}$$

Teoriškai, bimolekulinės rekombinacijos atveju, υ turėtų augti tiesiškai su $n(x)$. Tačiau praktinėse BHJ struktūrose krūvininkai yra pasiskirstę per visą sluoksnio tūrį, todėl norint ištirti kaip šis tūrinis pasiskirstymas veikia υ, kitame skyriuje aprašomas skaitmeninis modelis, leidžiantis simuliuoti EIC kinetiką ir interpretuoti υ koeficiento priklausomybę nuo krūvininkų tankio.

3.3. Baigtinių skirtumų metodas (FDM) krūvio pernašai ir rekombinacijai tirti

Šiame darbe baigtinių skirtumų metodas (FDM) buvo taikomas skaitmeniniam krūvininkų pernašos ir rekombinacijos procesų modeliavimui tūrinėse heterosandūrose (BHJ), esant krūvininkų injekcijos ir ekstrakcijos sąlygoms. FDM yra plačiai pripažintas diferencialinių lygčių sprendimo metodas, kai nagrinėjama fizinė sistema yra diskretizuojama į tinklą, o išvestinės pakeičiamos baigtiniais skirtumais, leidžiančiais tiksliai modeliuoti

sudėtingus reiškinius, tokius kaip dreifas, difuzija ir rekombinacija tiek laiko, tiek erdvės ašimis.

Šiame darbe aktyvusis saulės elemento sluoksnis modeliuojamas kaip vienmatė diskretizuotų celių eilė. Iš pradžių krūvininkai injektuojami į pirmąją ir paskutinę tinklo celes, taip imituojant elektronų ir skylių injekciją per atitinkamus elektrodus. Injektuojamų krūvininkų kiekis atitinka aktyviojo sluoksnio talpos sukauptą krūvį esant prijungtai įtampai ($Q = CU$). Sukurti krūvininkai juda veikiami dviejų pagrindinių procesų: dreifo dėl išorinio elektrinio lauko ir difuzijos, nulemtos krūvininkų koncentracijos gradientų.

Elektronų ir skylių dreifo srovės tankis apskaičiuojamas naudojant narvelio krūvininkų koncentraciją, judrį ir elektrinio lauko stiprį. Difuzijos srovės apskaičiuojamos pagal koncentracijos gradientus, vadovaujantis Fiko dėsniu, kai difuzijos koeficientas susiejamas su judriu per Einšteino ryšį. Kiekviename tinklelio taške dreifo ir difuzijos poveikis apskaičiuojamas atskirai, o jų derinys lemia bendrą krūvininkų srautą tarp gretimų celių.

Rekombinacija kiekvienoje celėje modeliuojama kaip Langevino tipo rekombinacija, kur rekombinacijos greitis yra proporcingas elektronų ir skylių koncentracijų sandaugai. Tačiau, siekiant atsižvelgti į eksperimentuose stebimą rekombinacijos koeficiento sumažėjimą BHJ sistemose, į rekombinacijos lygtis įvedamas redukcijos faktorius. Tai leidžia realistiškai modeliuoti mažesnius rekombinacijos greičius nei prognozuoja standartinė Langevino teorija.

Kiekviename laiko žingsnyje, atnaujinus krūvininkų pasiskirstymą, vietinis elektrinis laukas perskaičiuojamas naudojant Puasono lygtį, kuri sieja elektrinio lauko pokytį su lokaliu krūvininkų tankiu. Taikomos ribinės sąlygos užtikrina, kad elektrinis laukas per visą mėginį atitiktų prijungtą įtampą.

Simuliacija vyksta dviem ciklais:

- Injekcijos ciklas: Krūvininkai injektuojami tol, kol nusistovi srovė, kai injektuotų krūvininkų skaičius ir rekombinavusiųjų krūvininkų skaičius susilygina.
- Ekstrakcijos ciklas: Pasiekus stacionarią būseną, įtampos poliarumas pakeičiamas ir sukaupti krūvininkai ištraukiami per elektrodus. Visa ištraukimo proceso srovės kinetika registruojama.

Modelis automatiškai reguliuoja laiko žingsnį, siekiant užtikrinti skaičiavimų stabilumą ir tikslumą.

Kombinuojant FDM skaitmeninį modelį kartu su eksperimentiniais TOF ir EIC metodais, galima pasiekti gilesnį kiekybinį organinių BHJ sistemų struktūros ir funkcijos ryšių suvokimą: krūvininkų judrio santykio, morfologijos įtaką rekombinacijos sumažinimui bei elektrinio lauko elgseną, esant nestabilioms krūvininkų koncentracijoms.

4. Rezultatai ir jų aptarimas

4.1. Rekombinacinių procesų tyrimas P3HT:PCBM tūrinėje heterosandūroje, pasinaudojant injektuotų krūvinikų ekstrakcijos metodu

Kaip aptarta ankstesniuose skyriuose, rekombinacijos sparta polimerų ir fulerenų mišiniuose, tokiuose kaip P3HT:PCBM, yra iki 10^4 kartų lėtesnė nei prognozuoja Langevino teorija. Be to, šiuose mišiniuose rekombinacija nėra tiesiogiai antrinio laipsnio – pastebėta aukštesnė rekombinacijos priklausomybė nuo krūvininkų koncentracijos (rekombinacijos eilė 2,3–2,8), o tai rodo, kad vien sumažintos Langevino rekombinacijos modelis negali paaiškinti stebimų procesų. Sudėtinga P3HT:PCBM morfologija, įskaitant trečiosios amorfinės fazės buvimą (dėl molekulinio susimaišymo), leidžia manyti, kad vyraujantis rekombinacijos kelias yra per tarpines būsenas.
Šiame kontekste buvo taikytos kelios metodikos – injektuotų krūvininkų ištraukimas, lėkio trukmės matavimai ir baigtinių skirtumų metodas, siekiant įvertinti rekombinacijos priklausomybę nuo krūvininkų koncentracijos ir sluoksnio storio. Rekombinacijos priklausomybė nuo sluoksnio storio ypač svarbi naudojant 1,8-dijodooktano (DIO) priedą, kuris keičia P3HT:PCBM mišinio morfologiją priklausomai nuo plėvelės storio.

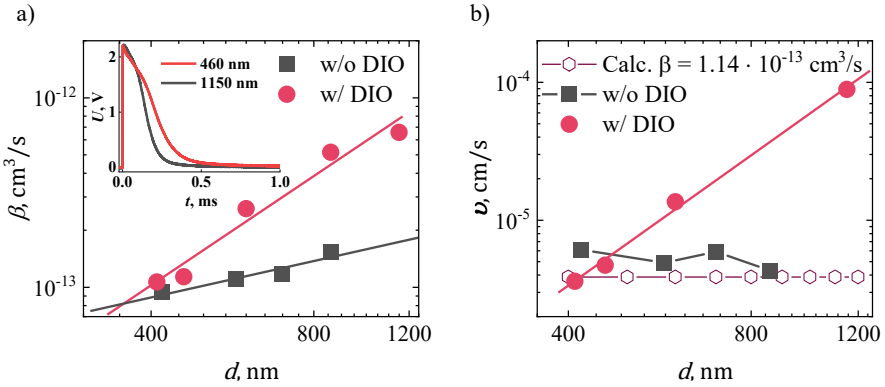

Pav. 1 a) Bimolekulinės rekombinacijos koeficientas β, nustatytas TOF; b) rekombinacijos spartos υ priklausomybė nuo P3HT: PCBM (1:1 masių santykio) sluoksnio storio (su ir be DIO priedu). Įbrėžtinė kreivė a) parodo integrinio TOF režimo įsisotinusias kinetikas skirtingo storio sluoksniuose su DIO priedu.

Eksperimentams paruošti P3HT:PCBM tūrinių heterosandūrų bandiniai buvo gaminami lašinant tirpalą ant TiO_2 padengtų FTO padėklų tiek su DIO priedu (3%) P3HT:PCBM tirpale, tiek be jo.

Nustačius bimolekulinės rekombinacijos koeficientą ir įvertinus krūvininkų judrius TOF metodu, gautus rezultatus buvo galima palyginti su EIC išvestais rekombinacinės spartos υ dydžiais ir FDM skaitmeniniais modeliavimais (**Pav. 1**).

Tyrimų rezultatai atskleidė, kad rekombinacija ženkliai išauga didėjant sluoksnio storiui, kuomet gamybos metu yra naudojamas DIO priedas. O mėginiai be priedo išlaiko panašias rekombinacijos greičio vertes nepriklausomai nuo storio. Bandiniuose be DIO rekombinacijos sparta υ seka FDM skaitmeninio modelio projekcijas ir praktiškai nekinta keičiantis sluoksnio storiui, o tai sufleruoja, kad bandiniuose su DIO tikėtina antro ar aukštesnio laipsnio rekombinacija. Šiek tiek didėjanti bimolekulinės rekombinacijos priklausomybė bandiniuose be DIO (**Pav. 1a**) gali būti paaiškinta skirtingais šviesos sugerties profiliais, tačiau ši priklausomybė yra ganėtinai silpna, lyginant rekombinaciją bandiniuose, pagamintuose su DIO.

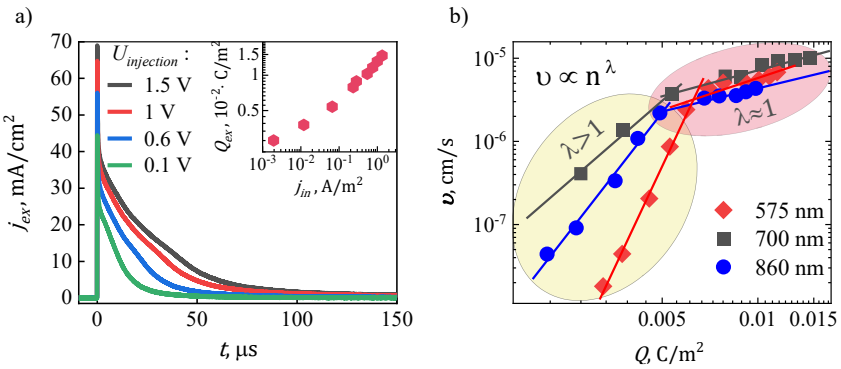

Pav. 2 a) Srovės kinetikos su įbrėžtine ištraukto krūvio priklausomybe nuo injekcinės srovės, b) ir rekombinacinės spartos priklausomybės nuo ištraukto krūvio, esant skirtingiems P3HT: PCBM 1:1 bandinio storiams.

Išmatavus υ priklausomybę nuo injektuoto krūvio, buvo pastebėta netiesinė priklausomybė nuo krūvininkų koncentracijos (**Pav. 2**), kuri rodo aukštesnės eilės rekombinaciją, būdingą sistemoms su daug pagavimo lygmenų. Pradžioje rekombinacija vyksta užpildant pagavimo lygmenis $\lambda > 1$ ir, kuomet lygmenys yra įsotinami, rekombinacija pereina į Lanževeno modelį ($\lambda \approx 1$). Reikia atsižvelgti į pagavimo lygmenis, rekombinaciją per daugkartinio lygmenų pagavimo-paleidimo modelį (MTR) ir tai, kad grynų medžiagų fazės, turinčios Gausinį lygmenų pasiskirstymą, yra atskirtos trečios amorfinės maišytos fazės su eksponentiniu būsenų pasiskirstymu[103]. Tai lemia greitesnį pagavimo lygmenų užsipildymą, lyginant su lygmenimis, esančiais

grynose fazėse, o tai reiškia, kad rekombinacija nėra apspręsta susitikimo tikimybės, kaip yra aprašyta Lanževino modelyje.
Apibendrinant, EIC metodas leido įvertinti, kaip rekombinacija priklauso nuo krūvininkų koncentracijos ir sluoksnio morfologijos P3HT:PCBM tūrinėse heterosandūrose. Nustatyta, kad sluoksnio storis naudojant DIO priedą turi esminę įtaką rekombinacijos greičiui. Be to, tyrimas atskleidė dvilypį rekombinacijos pobūdį – tik įvykus pagavimo lygmenų užpildymui rekombinacija pereina į Lanževino rekombinacijos modelį. Todėl, remiantis šiais rezultatais, galima daryti šias išvadas:

- EIC matavimai atskleidžia, kaip rekombinacijos greitis kinta priklausomai nuo krūvininkų tankio P3HT:PCBM tūrinėse heterosandūrose. Nustatyta, kad rekombinacija vyksta dviem etapais: pradžioje dominuoja pagavimo būsenų pildymas polimero–fulereno sandūroje, po kurio pereinama į Lanževino rekombinacijos ribojamą režimą. Šie du aiškūs režimai patvirtina, kad rekombinacija šioje sistemoje daugiausia yra pagavimo būsenų pobūdžio, o ne tūrinė.
- EIC metodu išmatuoti rekombinacijos greičiai rodo, kad P3HT:PCBM plėvelėse, kurių storis viršija 400 nm, priedas 1,8-diodooktanas sukelia morfologinius pokyčius, kurie padidina rekombinacinius nuostolius didėjant sluoksnio storiui.

4.2. Skersaryšinamos fluoreno pagrindo skylių pernašos medžiagos

Ilgalaikis tūrinių heterosandūrų organinių saulės elementų stabilumas yra apribotas įvairių degradacijos mechanizmų – tiek vidinių, tiek išorinių. Vienas iš perspektyviausių sprendimų – naudoti skersaryšinamus organinius junginius, kurie, termiškai apdoroti, sudaro kovalentiškai sujungtus polimerinius tinklus. Šie tinklai stabilizuoja aktyviojo sluoksnio morfologiją, sumažina fazių išsiskyrimą ir sustiprina mechaninį bei cheminį atsparumus, ypač svarbius apverstos architektūros (inverted) prietaisuose.
Šiame tyrime buvo nagrinėjami keturi naujai susintetinti fluoreno pagrindo skylių pernašos junginiai – **V1145, V1177, V1178 ir V1179**, sukurti V. Getaučio grupės (KTU). Šios medžiagos turi šoninių grupių (metilinių ir fenilinių) variacijas, kurios gali turėti įtakos molekulių išsidėstymui, skersaryšinimui ir krūvininkų pernašai. Pagrindinis tikslas buvo ištirti kaip skersaryšinimas paveikia krūvio pernašą: naujų ryšių sukūrimas ir senų ryšių nutraukimas polimerizacijos metu gali padidinti erdvinę ir energetinę netvarką. Papildomai viena iš medžiagų buvo išbandyta tūrinės heterosandūros matricoje, siekiant įvertinti tokios struktūros veikimą.

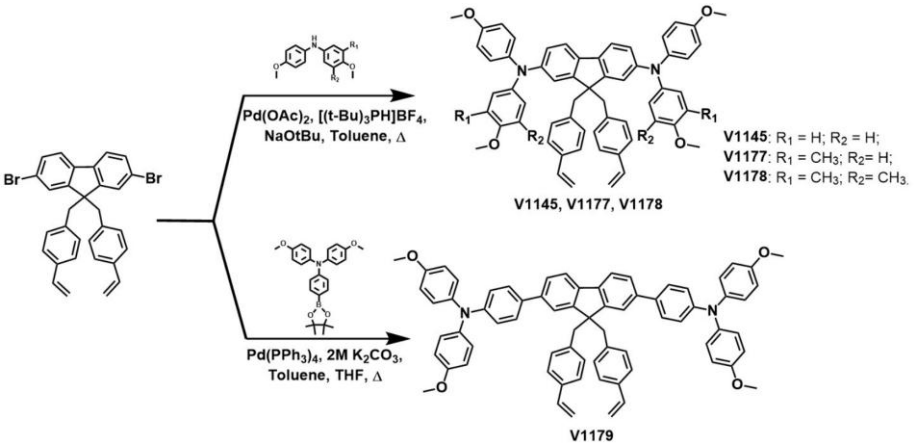

Pav. 3 Skersaryšinami skylių pernašos junginiai **V1145, V1177, V1178, V1179** ir jų sintetinimo keliai.

Visi junginiai buvo sintetinti taikant Buchwald–Hartwig aminavimo reakciją, naudojant komerciškai prieinamus arilaminus ir specifinius tarpininkus, kurie sujungti su vinil-funkcionalizuotu dibromo-fluorenu. Struktūriniai tyrimai (rezultatai APPENDIX II) patvirtino tikslinių junginių susidarymą.
Sugerties ir fotoliuminescencijos (PL) spektrai parodė, kad **V1145** sugerties maksimumas yra 378 nm, o fenilinėmis grupėmis modifikuotas **V1179** yra šiek tiek pasislinkęs į ilgabangę pusę. Metilinti junginiai (**V1177, V1178**) demonstravo sugerties smailės poslinkį į trumpesnius bangų ilgius dėl galimai sumažėjusios konjugacijos. Visi junginiai šiek tiek sugeria matomoje srityje, tai gali turėti nedidelį neigiamą poveikį fotogeneracijos efektyvumui, naudojant juos kaip pernašos sluoksnius saulės elementuose.

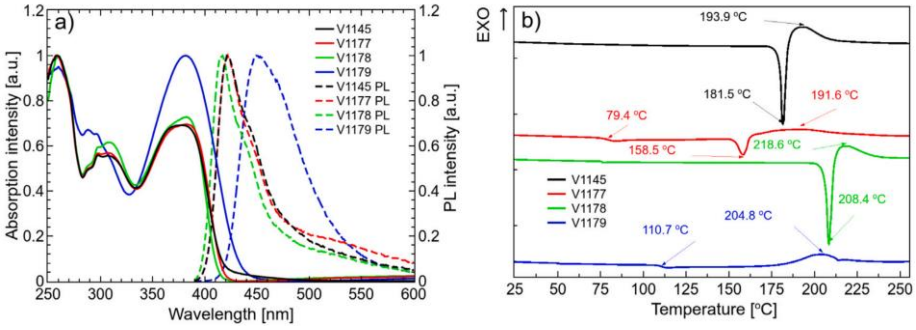

Pav. 4 (a) Sugerties ir fotoliuminescencijos spektrai; (b) DSC kreivės ir lydymosi, skersaryšinimo, stiklėjimo temperatūros.

Terminės gravimetrijos analizės (TGA) (APPENDIX II) tyrimai parodė, kad visi junginiai yra termiškai stabilūs, o 5 % svorio netekimo temperatūra viršija

387–403 °C. Diferencinės skenuojančios kalorimetrijos (DSC) analizė parodė, kad skersaryšinimas prasideda nuo ~190 °C. Tai patvirtinama tuo, kad antrame šildymo cikle nebeaptinkama lydimosi ar stiklo perėjimo temperatūrų.
Raman spektroskopija (**66 psl.**), atlikta **V1145** junginiui, aiškiai parodė vinilo grupių dalyvavimą polimerizacijos reakcijoje – po kaitinimo C=C ir =C–H vibraciniai virpesiai sumažėjo, o jų pozicijos šiek tiek pasislinko. Polimerizacijos efektyvumas **V1145** junginiui po 1 val. prie 200 °C buvo apie 40 %. Kitiems junginiams efektyvumas įvertintas pagal sugerties spektro pokyčius (rezultatai pateikti APPENDIX II).

4.2.1 Krūvininkų pernaša ir netvarka fluoreno pagrindo skersaryšinamose skylių pernašos medžiagose

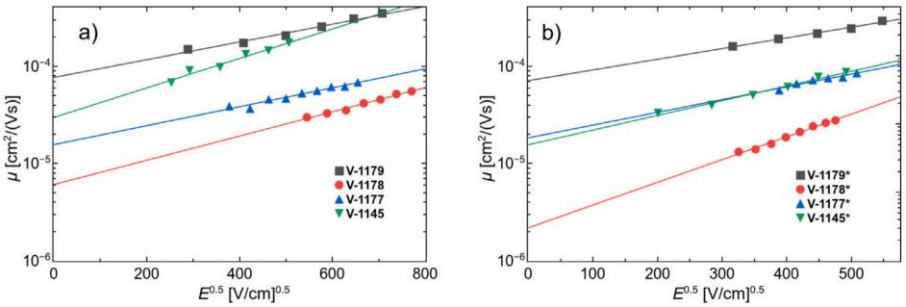

Pav. 5 Skylių judrio priklausomybės nuo elektrinio lauko a) neskersaryšintuose ir b) skersaryšintuose **V1145, V1177, V1178, V1179** sluoksniuose.

Naudojant TOF metodą, buvo įvertinta skylių judrio priklausomybė nuo elektrinio lauko ir temperatūros prieš ir po skersaryšinimo. Po skersaryšinimo visų junginių TOF kinetikos (**67 psl.**) tapo labiau dispersinės, o tranzito laikas pailgėjo – tai rodo padidėjusį netvarkingumą ir molekulinį persitvarkymą sluoksniuose po skersaryšinimo.
Molekulinė struktūra turėjo didelę įtaką krūvio pernašai(**1 lent.**). Metilinės grupės (**V1177, V1178**) galimai sumažino konjugaciją ir π–π orbitalių sąveikas, taip mažindamos skylių judrį. Fenil grupė **V1179** molekulėje priešingai – išplėtė konjugacinę sistemą, todėl šis junginys pasižymėjo didžiausiu skyliniu judriu.
Remiantis Bässler'io formalizmo modeliu buvo apskaičiuoti erdvinio (Σ) ir energetinio (σ) netvarkingumo parametrai, kurie parodė, kad skersaryšinimas didina abi netvarkas, o tai koreliuoja su stebimu judrio sumažėjimu (**1 lent.**). Papildomos metilo grupės lėmė šiek tiek mažesnį pokytį erdvinėje netvarkoje

po skersaryšinimo lyginant su **V1145**. Panašus efektas stebimas ir esant papildomoms fenil grupėms.
Nors skylių judris ir sumažėjo, HOMO energijos lygis išliko praktiškai nepakitęs (APPENDIX II), kas yra itin svarbu energetinių lygių derinimui prietaisuose.

1 Lentelė. Energetinės ir erdvinės netvarkos parametrai σ ir Σ, skylių judriai μ_0 , kuomet elektrinis laukas $E = 0$, prie ir po skersaryšinimo.

Material		σ, meV	Σ	μ_0, $cm^2V^{-1}s^{-1}$	σ*/σ	Σ*/Σ
V1145	Regular	22,51	1,69	$2,99 \cdot 10^{-5}$	3,26	2,74
	Cross-linked	61,72	5,52	$1,56 \cdot 10^{-5}$		
V1177	Regular	46,80	0,67	$1,56 \cdot 10^{-5}$	4,77	2,05
	Cross-linked	96,10	3,20	$1,84 \cdot 10^{-5}$		
V1178	Regular	56,30	1,37	$6,08 \cdot 10^{-6}$	1,34	1,5
	Cross-linked	84,98	1,85	$2,18 \cdot 10^{-6}$		
V1179	Regular	117,30	3,90	$7,67 \cdot 10^{-5}$	1,23	1,13
	Cross-linked	133,59	4,87	$7,12 \cdot 10^{-5}$		

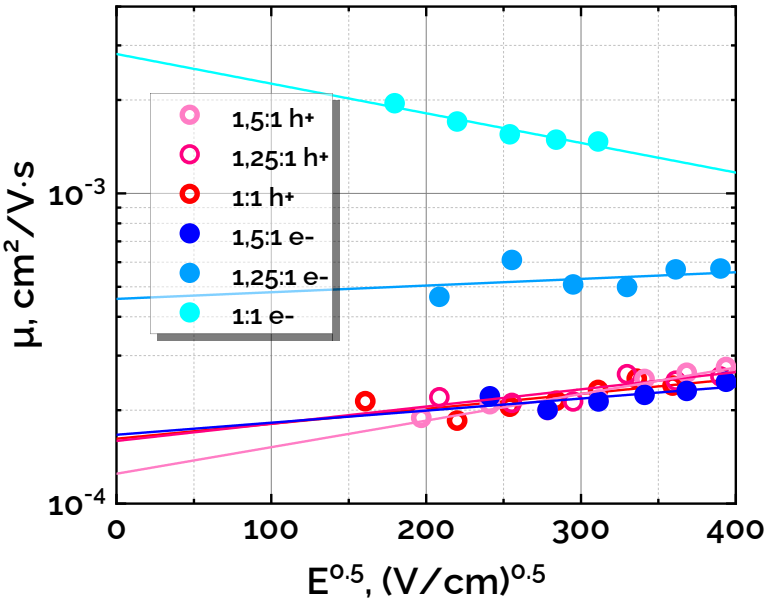

Pav. 6 Krūvininkų judrio priklausomybė nuo elektrinio lauko skirtingų masės santykių V1179:PCBM mišinių sluoksniuose.

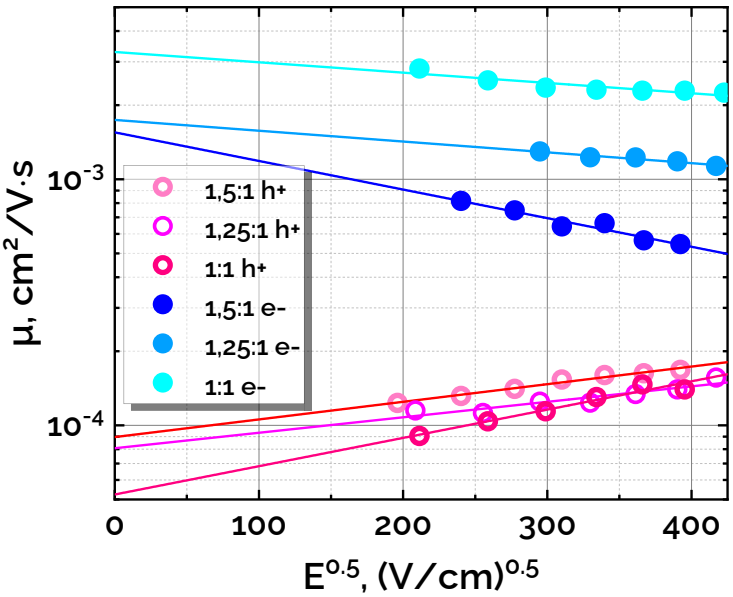

Pav. 7 Krūvininkų judrio priklausomybė nuo elektrinio lauko skirtingų masės santykių skersaryšintuose V1179:PCBM mišinių sluoksniuose.

Siekiant įvertinti šių junginių tinkamumą praktiniams įrenginiams, **V1179** buvo pasirinktas kaip donorinė medžiaga BHJ mišinyje su PCBM (akceptorius) skirtingais masių santykiais (1.5:1, 1.25:1 ir 1:1). TOF matavimai prieš ir po skersaryšinimo parodė, kad:

- Skylių judris šiek tiek sumažėjo po skersaryšinimo dėl nežymios energetinės ir erdvinės netvarkos padidėjimo. (**2 Lentelė**)
- Elektronų judris padidėjo, dėl PCBM palankaus domenų persitvarkymo skersaryšinimo metu. Šis efektas buvo stebimas esant skirtingiems mišinių santykiams. (**2 Lentelė**)

Tai rodo, kad **V1179** galima naudoti kaip donorinę medžiagą BHJ struktūrose net ir skersaryšinant, nepažeidžiant bendros krūvininkų pernašos dinamikos.

2 Lentelė. V1179:PCBM sluoksnių krūvininkų judriai prieš ir po skersaryšinimo.

V1179:PCBM			**V1179:PCBM cross-linked**		
wt.% ratio	μ_0^e, $cm^2/V \cdot s$	μ_0^h, $cm^2/V \cdot s$	**wt.% ratio**	μ_0^e, $cm^2/V \cdot s$	μ_0^h, $cm^2/V \cdot s$
1.5:1	$1.67 \cdot 10^{-4}$	$1.25 \cdot 10^{-4}$	**1.5:1**	$1.55 \cdot 10^{-3}$	$8.88 \cdot 10^{-5}$
1.25:1	$4.57 \cdot 10^{-4}$	$1.60 \cdot 10^{-4}$	**1.25:1**	$1.74 \cdot 10^{-3}$	$8.00 \cdot 10^{-5}$
1:1	$2.80 \cdot 10^{-3}$	$1.62 \cdot 10^{-4}$	**1:1**	$3.29 \cdot 10^{-3}$	$5.19 \cdot 10^{-5}$

Taigi, fluoreno pagrindu sukurti skersaryšinami skylių pernašos junginiai yra perspektyvūs kandidatai ilgalaikei organinių saulės elementų stabilizacijai. Visi keturi junginiai (**V1145, V1177, V1178, V1179**) buvo sėkmingai termiškai polimerizuoti esant >200 °C, o jų plėvelės išlaikė stabilumą iki ~400 °C. Skersaryšinimas nežymiai padidino erdvinį ir energetinį netvarkingumą ir sumažino skylių judrį, tačiau HOMO lygiai išliko stabilūs. Ypač pažymėtinas **V1179**, kuris pasižymėjo dideliu judriu prieš skersaryšinimą ir po jo. Net ir BHJ mišinyje su PCBM **V1179** išlaikė efektyvią krūvininkų pernašą, o elektronų judris netgi padidėjo suskersaryšinus sluoksnį. Šios savybės rodo, kad tokie HTM junginiai gali būti integruoti į veikiančius fotovoltinius įrenginius – ypač apverstuose architektūriniuose sprendimuose, kur reikalingas didesnis atsparumas išoriniams poveikiams.

4.3. Subalansuoto judrio bipolinės fluoreno pagrindo krūvio pernašos medžiagos

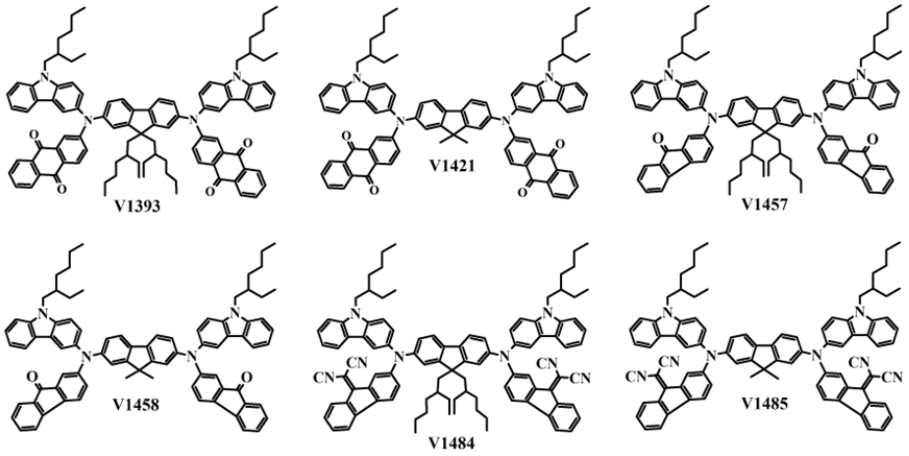

Pav. 8 Susintetinti bipoliniai junginiai su skirtingais struktūriniais vienetais.

Šioje dalyje dėmesys skiriamas bipolinėms fluoreno pagrindo krūvio pernašos medžiagoms, kurios sukurtos siekiant užtikrinti subalansuotą skylių ir elektronų pernašą – tai ypač svarbus aspektas aukštos kokybės organiniuose prietaisuose. Nesubalansuotas skylių ir elektronų judris gali sukelti erdvinio krūvio efektą, kuris lems lėčiau judančių krūvininkų akumuliaciją. Tai sukurs vidinį elektrinį lauką, kuris stabdys kitų krūvių ištraukimą ir didins rekombinacinius nuostolius. Subalansuotų judrių bipolinės pernašos medžiagos, pritaikytos, pvz., organiniuose saulės elementuose, galėtų pagerinti krūvininkų atskyrimą ir pernašą, o pritaikytos tūrinių heterosandūrų mišiniuose galėtų išspręsti ir donoro/akceptoriaus suderinamumo ir fazinės atskirties problemas.

Įprastai tirpūs ir ore stabilūs bipoliniai pernašos junginiai turi gana sudėtingas struktūras, kurios reikalauja sudėtingos kelių žingsnių sintezės ir brangių pradinių medžiagų. Šiame darbe V.Getaučio grupė susintetino šešis naujus fluoreno pagrindo bipolinius junginius – **V1393, V14211, V1457, V1458, V1484 ir V1485** (**Pav. 8**), kurie gali būti dengiami iš tirpalo ir yra termiškai stabilūs temperatūrose iki 400°C. Šie junginiai gali būti pagaminti paprastais ir ekonomiškais būdais, naudojant komerciškai prieinamas pradines medžiagas. Šie junginiai turi elektronų akceptorius – antrachinoną, 9-fluorenoną arba dicianofluorenilideno grupes bei elektronų donorus – karbazolil grupes. Tokia donoras-akceptorius (D-A) molekulinė sandara skatina intramolekulinį krūvininkų pernašos mechanizmą, būtiną bipolinei pernašai.

TGA ir DSC analizės parodė aukštą medžiagų šiluminį stabilumą bei amorfines savybes, kurios palankios kokybiškų sluoksnių formavimui iš tirpalo. DSC skenavimai parodė stiklėjimo perėjimo temperatūras (T_g) nuo 92°C iki 161°C, priklausomai nuo šoninių grandinių ilgio bei pakaitų. Pastebėta, kad ilgesnės alkilo grandinės mažina T_g, o tai gali pagerinti sluoksnių formavimą, bet sumažinti šiluminį atsparumą. Visose medžiagose nebuvo pastebėta jokių endoterminių smailių ir medžiagos išliko amorfinės net po kelių šildymo ciklų. Amorfinė būsena yra pageidautina norint gauti aukštos kokybės amorfinius sluoksnius.

4.3.1. Krūvio pernaša ir rekombinacija bipoliniuose fluoreno pagrindo dariniuose

Naujų medžiagų tirpalo (THF tirpiklyje) ir kietos fazės sluoksnio sugerties spektrų palyginimas pateiktas **Pav. 9**, atitinkami išvestiniai duomenys pateikti **3 lentelėje**. Sugerties spektrai parodė kelias sugerties juostas - stipri π–π* sugertis tarp 270–450 nm ir silpnesnė n–π* sugertis matomoje srityje (~510 nm), ypač junginiuose su antrachinono ar dicianoylideno grupėmis. Lyginant V1393, V1421 sugerties spektrus su V1457, V1458 sugerties spektrais, galima įžiūrėti sugerties smailių raudonąjį poslinkį. Stipresnė V1393, V1421 sugertis ties 510 nm gali būti paaiškinta papildomais deguonies atomais molekulės struktūroje. Panašus efektas stebimas ir su dicianoylideno grupėmis. Nedidelis spektrinis poslinkis plėvelėse (~3 nm), lyginant su tirpalo spektru, gali sufleruoti apie silpną tarpmolekulinę sąveiką kietoje būsenoje. Kita vertus, šis poslinkis galėtų reikšti ir agregatų formavimąsi net mažos koncentracijos tirpale, ką galėtų paremti kvantinės chemijos skaičiavimai rodantys, kad tarpmolekulinės būsenos yra galimos tik esant dimerinėms molekulių struktūroms (pvz., V tipo ir branduolys-branduolys, APPENDIX III). Nepaisant sudėtingos sandaros, nei tirpaluose, nei plėvelėse fluorescencija nebuvo užfiksuota.

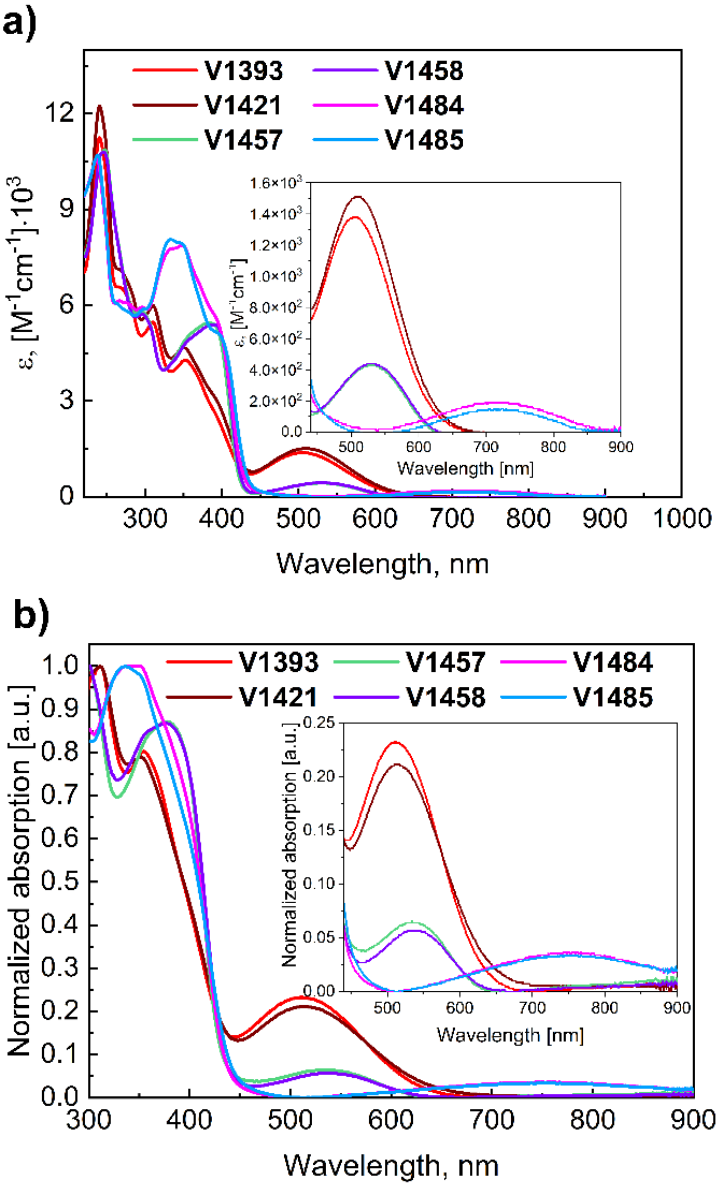

Pav. 9 Bipolinių pernašos junginių sugerties spektrai iš: a) THF tirpalo ($c=10^{-4}$ mol/l); b) plėvelės.

3 Lentelė. a) Sugerties maksimumai plėvelėse;b) Jonizacinė energija išmatuota PESA; c), d) HOMO ir LUMO lygmenys nustatyti CV matavimais; e) Skylių judris esant nuliniam electrinio lauko stipriui; f) Elektronų judris esant nuliniam electrinio lauko stipriui

Compound	λ_{abs} [nm][a)]	I_p [eV][b)]	*HOMO* [eV][c)]	*LUMO* [eV][d)]	$\mu_{0\ \text{Hole}}$ [cm^2/Vs][e)]	$\mu_{0\ \text{Elec.}}$ [cm^2/Vs][f)]
V1393	311, 355, 512,	5.18	5.38	3.85	2.6×10^{-7}	4.6×10^{-9}
V1421	311, 352, 514	5.21	5.51	4.0	1.4×10^{-7}	1.1×10^{-9}
V1457	378, 534	5.02	5.34	3.97	3.9×10^{-7}	-
V1458	377, 537	5.02	5.46	4.09	9.2×10^{-8}	-
V1484	337, 346, 760	5.18	5.54	4.16	1.2×10^{-7}	1.0×10^{-8}
V1485	337, 750	5.16	5.42	4.09	2.8×10^{-8}	3.5×10^{-9}

Siekiant įvertinti krūvininkų pernašos savybes, buvo pasitelktas TOF metodas nustatyti skylių ir elektronų judriams. XTOF kinetikos pateiktos APPENDIX IV. Gautos judrių priklausomybės nuo elektrinio lauko pateiktos **Pav. 10.** Rezultatai aiškiai parodė, kad molekulės, turinčios antrachinono (**V1393**, **V1421**) ir dicianoylideno (**V1484**, **V1485**) grupes, pasižymi neigiamų ir teigiamų krūvininkų pernaša, kur skylių judris yra eile didesnis už elektronų. Tačiau nepavyko išgauti aiškios elektronų kinetikos junginiams su 9-fluorenonu (**V1457**, **V1458**). Vienintelis pastebimas ilgesnių alkilinių grandinėlių poveikis (**V1393**, **V1457**, **V1484**) buvo nedidelis skylinio judrio padidėjimas prie mažesnių elektrinių laukų, todėl galima daryti prielaidą, kad ilgesnės alkilinės grandys lemia palankesnį molekulinį išsidėstymą krūvio pernašai.

Pakeitus keto grupes į dicianoylideno grupes, buvo pastebėtas sumažėjęs skylių judris ir padidėjęs elektronų judris. Geriausiai subalansuotas krūvininkų judris buvo **V1484** ir **V1485** sluoksniuose, kur skylių judris prie nulinio elektrinio lauko siekį $1.2 \times 10^{-7}\ cm^2\ V^{-1}\ s^{-1}$, o elektronų $1.0 \times 10^{-8}\ V^{-1}\ s^{-1}$.

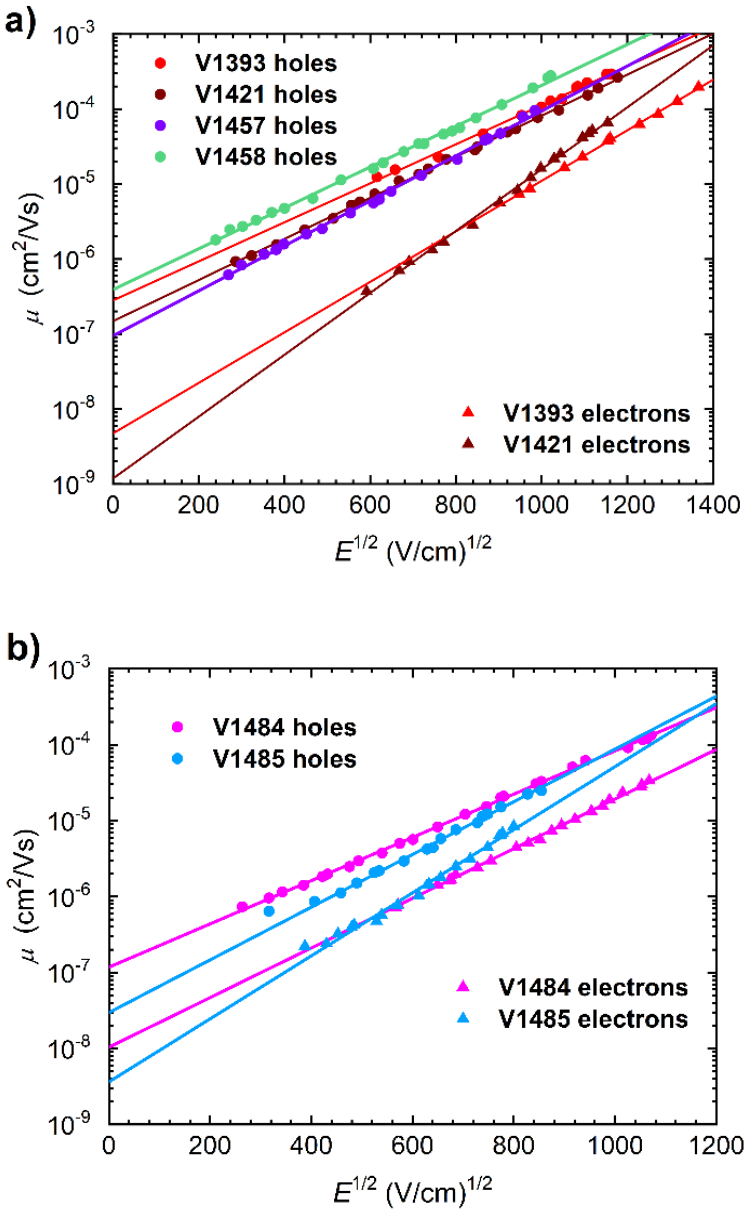

Pav. 10 Judrių priklausomybės nuo elektrinio lauko junginiuose su a) antrachinono ir 9-fluorenono funkcinėmis grupėmis (**V1393**, **V1421**, **V1457**, ir **V1458**) bei b) dicianoylideno grupe (**V1484** and **V1485**).

Fotosrovės gesimo matavimai buvo atlikti siekiant daugiau įžvalgų apie krūvio pernašą šiuose sluoksniuose. Prijungtas elektrinis laukas nebuvo pakankamas, norint ištraukti krūvį iš sluoksnio, todėl fotosrovės gesimas buvo

nulemtas krūvio pagavimo ir rekombinacinių procesų[101,102]. Gauti gesimo profiliai buvo sunormalizuoti, kad galima būtų palyginti fotosrovės gesimo uodegas ($2 \cdot 10^{-5}$ - $1 \cdot 10^{-4}$ s), kurios dažniausiai yra priskiriamos giliems pagavimo lygmenims ir rekombinacijai.

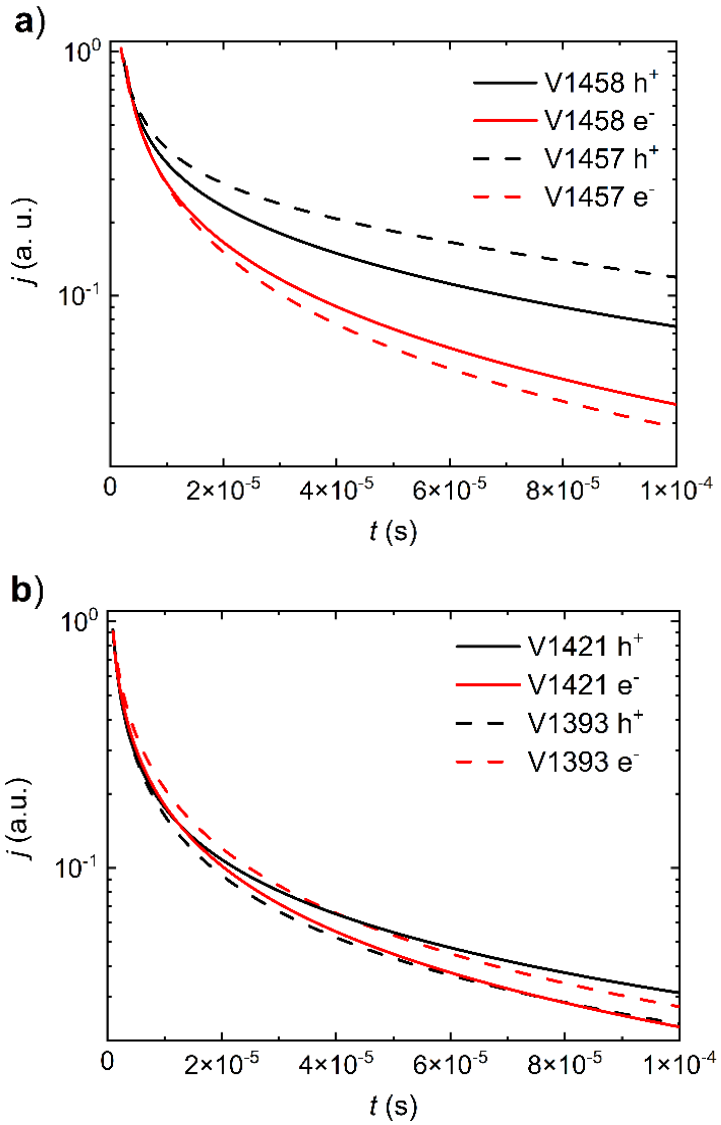

Pav. 11 Fotosrovės gesimo profiliai junginiams su a) 9-fluorenono funkcinėmis grupėmis (**V1457** ir **V1458**) ir b) antrachinono grupėmis (**V1393** ir **V1421**).

Sluoksniuose su antrachinono fragmentais (**Pav. 11b**) fotosrovės gesimo profiliai tiek skylėms, tiek elektronams atkartoja panašias kinetikas su

minimaliu papildomų alkilinių grandinių poveikiu. Stipriausi pokyčiai yra pastebimi keičiant alkilinių grandinių ilgį junginiuose, turinčiuose 9-fluorenono fragmentus(**V1458**, **V1457**) (**Pav. 11a**). Alkilinių grandinių pailgėjimas lėmė mažesnį prilipimą-atlipimą skylių pernašoje ir didesnę rekombinaciją, tai galima paremti ir mažesniu skyliniu judriu, stebimu **V1458**. Be to, elektronų fotosrovės gesimas parodė gana silpną jautrumą tam pačiam alkilinių grandinių pakitimui. Dicianoylideno turinčiuose junginiuose (**V1484**, **V1485**) (**Pav. 12**) priešingai – ilgesnės alkilinės grandinės pagerino elektronų pernašą ir sulėtino fotosrovės gesimą, tikėtina, dėl geresnio molekulių išsidėstymo.

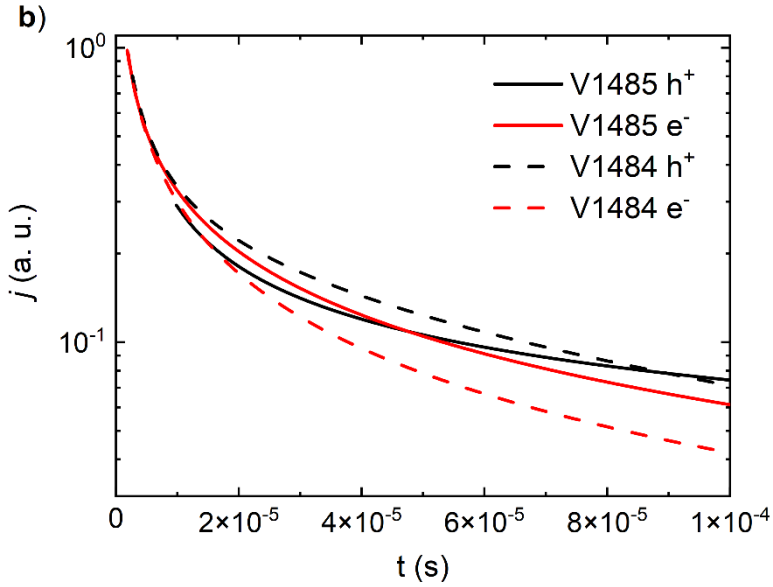

Pav. 12. Fotosrovės gesimo profiliai junginiams su dicianoylidino funkcinėmis grupėmis (**V1484** ir **V1485**).

Apibendrinant, sukurtos naujos, amorfinės, fluoreno pagrindu susintetintos bipolinės krūvininkų pernašos medžiagos, turinčios antrachinono, 9-fluorenono arba dicianoylideno grupes kartu su karbazolo donorinėmis grupėmis. Šie junginiai buvo lengvai susintetinti, turi geras plėvelių formavimo savybes ir tinka apdorojimui iš tirpalo fazės. Optiniai sugerties matavimai kartu su kvantinės chemijos skaičiavimais patvirtina intramolekulinių krūvio pernašos kompleksų formavimąsi bei, tikėtina, dimerinių struktūrų susidarymą, ypač V ir branduolio-branduolio tipo (APPENDIX III).

Visos medžiagos parodė skylinius judrius tarp 10^{-4} ir 10^{-5} $cm^2/V \cdot s$, o junginiai su antrachinonu ir dicianoylidenu turėjo tik eile mažesnius elektronų judrius.

Nors 9-fluorenono turinčių junginių elektronų pernaša buvo dispersinė, kiti junginiai parodė geras perspektyvas būti naudojami organinėje elektronikoje, įskaitant OSC ir OLED. Dėl jų paprastos sintezės, stabilumo, galimybės apdoroti iš tirpalo ir potencialiai subalansuotos pernašos, šie junginiai yra stiprūs kandidatai naujos kartos organiniams įrenginiams.

IŠVADOS

- Injektuoto krūvio ištraukimo (EIC) matavimai atskleidžia, kaip rekombinacijos greitis kinta priklausomai nuo krūvininkų tankio P3HT:PCBM tūrinėse heterosandūrose. Nustatyta, kad rekombinacija vyksta dviem etapais: pradžioje dominuoja pagavimo būsenų pildymas polimero–fulereno sandūroje, po kurio pereinama į Lanževino rekombinacijos ribojamą režimą. Šie du aiškūs režimai patvirtina, kad rekombinacija šioje sistemoje daugiausia yra pagavimo būsenų pobūdžio.
- EIC metodu išmatuoti rekombinacijos greičiai rodo, kad P3HT:PCBM plėvelėse, kurių storis viršija 400 nm, priedas 1,8-diodooktanas sukelia morfologinius pokyčius, kurie padidina rekombinacinius nuostolius didėjant sluoksnio storiui.
- Vinilo funkcionalizuotų fluoreno darinių terminė polimerizacija stabilizuoja plėvelės morfologiją ir padidina šiluminį stabilumą, nekeisdama HOMO energijos lygio. Tačiau tai sukelia nedidelį skylių judrio sumažėjimą ir nežymų erdvinio bei energetinio netvarkingumo padidėjimą. Geriausias (V1179) junginys parodė 1,27 karto didesnę energetinę netvarką ir 1,13 karto didesnę erdvinę netvarką po skersaryšinimo.
- V1179:PCBM mišiniuose skersaryšinimas ne tik išlaiko, bet kai kuriais atvejais net pagerina elektronų judrį, nežymiai pablogindamas skylių pernašą. Tai rodo, kad kovalentinis struktūros „fiksavimas“ nebūtinai pažeidžia skylių ir elektronų pernašos pusiausvyrą.
- Nauji amorfiniai fluoreno dariniai su antrachinono, 9-fluorenono arba dicianofluorenilideno struktūriniais elementais sudaro intramolekulinius krūvininkų pernašos kompleksus ir pasižymi subalansuota skylių (10^{-4}–10^{-5} $cm^2/V \cdot s$) ir elektronų pernaša, tinkama naudoti organiniuose prietaisų taikymuose.

CURRICULUM VITAE

Name: Romualdas Jonas

Surname: Čepas

EDUCATION:

- **2013 – 2017**
  Vilnius University
  Physics
  Bachelor‘s degree in Physics

- **2017 – 2019**
  Vilnius University
  Materials and Technology of Optoelectronics
  Master‘s degree in Technological Sciences

- **2019 –**
  Vilnius University
  Materials Engineering
  Doctoral degree in Technology Sciences

WORK EXPERIENCE:

- **2017 – 2019**
  Vilnius University
  Institute of Chemical Physics
  Technician

- **2019 – 2024**
  Vilnius University
  Institute of Chemical Physics
  Laboratory Technician

  2024 –
  Vilnius University
  Institute of Chemical Physics
  Lecturer

REFERENCES

1. Bulavko, G. V & Ishchenko, A. A. Organic bulk heterojunction photovoltaic structures: design, morphology and properties. *Russian Chemical Reviews* **83**, 575–599 (2014).
2. Shivanna, R. *et al.* Charge generation and transport in efficient organic bulk heterojunction solar cells with a perylene acceptor. *Energy Environ Sci* **7**, 435–441 (2014).
3. Peet, J., Heeger, A. J. & Bazan, G. C. 'Plastic' solar cells: Self-assembly of bulk heterojunction nanomaterials by spontaneous phase separation. *Acc Chem Res* **42**, 1700–1708 (2009).
4. Lin, Y., Li, Y. & Zhan, X. Small molecule semiconductors for high-efficiency organic photovoltaics. *Chem Soc Rev* **41**, 4245–4272 (2012).
5. Scharber, M. C. & Sariciftci, N. S. Efficiency of bulk-heterojunction organic solar cells. *Progress in Polymer Science* vol. 38 1929–1940 (2013).
6. Tang, C. W. Two-layer organic photovoltaic cell. *Appl Phys Lett* **48**, 183–185 (1986).
7. Yu, G., Gao, J., Hummelen, J. C., Wudl, F. & Heeger, A. J. Polymer Photovoltaic Cells: Enhanced Efficiencies via a Network of Internal Donor-Acceptor Heterojunctions. *Science* **270**, 1789-1791 (1995).
8. Peng, W. *et al.* Over 18% ternary polymer solar cells enabled by a terpolymer as the third component. *Nano Energy* **92**, (2022).
9. Chen, Y., Zhan, C. & Yao, J. Understanding Solvent Manipulation of Morphology in Bulk-Heterojunction Organic Solar Cells. *Chemistry - An Asian Journal* vol. 11 2620–2632 (2016).
10. Yi, Z. *et al.* Effect of thermal annealing on active layer morphology and performance for small molecule bulk heterojunction organic solar cells. *J Mater Chem C Mater* **2**, 7247–7255 (2014).
11. Shafiey Dehaj, M., Ahmadi, M. & Ghazanfarpour, S. Inverted bulk heterojunction organic solar cells using optimization of active layer deposition via controlling of doctor blade parameters. *Surfaces and Interfaces* **21**, (2020).
12. Park, S. E. *et al.* Fabrication of ordered bulk heterojunction organic photovoltaic cells using nanopatterning and electrohydrodynamic spray deposition methods. *Nanoscale* **4**, 7773–7779 (2012).
13. Vanlaeke, P. *et al.* P3HT/PCBM bulk heterojunction solar cells: Relation between morphology and electro-optical characteristics. *Solar Energy Materials and Solar Cells* **90**, 2150–2158 (2006).

14. Klein, M. F. G. *et al.* Poly(3-hexylselenophene) solar cells: Correlating the optoelectronic device performance and nanomorphology imaged by low-energy scanning Transmission electron microscopy. *J Polym Sci B Polym Phys* **50**, 198–206 (2012).
15. Drummy, L. F. *et al.* Molecular-scale and nanoscale morphology of P3HT:PCBM bulk heterojunctions: Energy-filtered TEM and low-dose HREM. *Chemistry of Materials* **23**, 907–912 (2011).
16. Coffey, D. C., Reid, O. G., Rodovsky, D. B., Bartholomew, G. P. & Ginger, D. S. Mapping local photocurrents in polymer/fullerene solar cells with photoconductive atomic force microscopy. *Nano Lett* **7**, 738–744 (2007).
17. Ruderer, M. A., Meier, R., Porcar, L., Cubitt, R. & Müller-Buschbaum, P. Phase separation and molecular intermixing in polymer-fullerene bulk heterojunction thin films. *Journal of Physical Chemistry Letters* **3**, 683–688 (2012).
18. Doumon, N. Y., Yang, L. & Rosei, F. Ternary organic solar cells: A review of the role of the third element. *Nano Energy* vol. 94 (2022).
19. Ma, X. *et al.* Highly efficient quaternary organic photovoltaics by optimizing photogenerated exciton distribution and active layer morphology. *Nano Energy* **70**, (2020).
20. Zhong, W. *et al.* Enhanced Photovoltaic Performance of Ternary Polymer Solar Cells by Incorporation of a Narrow-Bandgap Nonfullerene Acceptor. *Chemistry of Materials* **29**, 8177–8186 (2017).
21. Ma, X. *et al.* Achieving 17.4% Efficiency of Ternary Organic Photovoltaics with Two Well-Compatible Nonfullerene Acceptors for Minimizing Energy Loss. *Adv Energy Mater* **10**, (2020).
22. Ye, L. *et al.* From binary to ternary solvent: Morphology fine-tuning of D/A blends in PDPP3T-based polymer solar cells. *Advanced Materials* **24**, 6335–6341 (2012).
23. Wang, Z. *et al.* Mechanistic Investigation into Dynamic Function of Third Component Incorporated in Ternary Near-Infrared Nonfullerene Organic Solar Cells. *Adv Funct Mater* **30**, (2020).
24. Liu, F. *et al.* Efficient polymer solar cells based on a low bandgap semi-crystalline DPP polymer-PCBM blends. *Advanced Materials* **24**, 3947–3951 (2012).
25. Gu, Y. *et al.* Guided crystallization of P3HT in ternary blend solar cell based on P3HT:PCPDTBT:PCBM. *Energy Environ Sci* **7**, 3782–3790 (2014).

26. Zhao, F., Filbrun, S. L., Huang, T., Dong, B. & Fang, N. Multiscale evolution of bulk heterojunction solar cell active layers under thermal stress. *Anal Chem* **93**, 1232–1236 (2021).
27. Yang, D. *et al.* In Situ Studies of Solvent Additive Effects on the Morphology Development during Printing of Bulk Heterojunction Films for Organic Solar Cells. *Small Methods* **4**, (2020).
28. Gorenflot, J. *et al.* Nongeminate recombination in neat P3HT and P3HT:PCBM blend films. *J Appl Phys* **115**, (2014).
29. Street, R. A., Schoendorf, M., Roy, A. & Lee, J. H. Interface state recombination in organic solar cells. *Phys Rev B Condens Matter Mater Phys* **81**, 1–12 (2010).
30. Labiod, A. *et al.* Photo-degradation in bulk heterojunction organic solar cells using a fullerene or a non-fullerene derivative electron acceptor. *Org Electron* **107**, (2022).
31. Alam, S. *et al.* Thermally-Induced Degradation in PM6:Y6-Based Bulk Heterojunction Organic Solar Cells. *Adv Funct Mater* **34**, (2024).
32. Rafique, S., Abdullah, S. M., Sulaiman, K. & Iwamoto, M. Fundamentals of bulk heterojunction organic solar cells: An overview of stability/degradation issues and strategies for improvement. *Renewable and Sustainable Energy Reviews* vol. 84 43–53 (2018).
33. Schilinsky, P., Waldauf, C. & Brabec, C. J. Recombination and loss analysis in polythiophene based bulk heterojunction photodetectors. *Appl Phys Lett* **81**, 3885–3887 (2002).
34. Halls, J. J. M., Pichler, K., Friend, R. H., Moratti, S. C. & Holmes, A. B. Exciton diffusion and dissociation in a poly(p-phenylenevinylene)/C60 heterojunction photovoltaic cell. *Appl Phys Lett* **68**, 3120–3122 (1996).
35. Padinger, F., Rittberger, R. S. & Sariciftci, N. S. Effects of postproduction treatment on plastic solar cells. *Adv Funct Mater* **13**, 85–88 (2003).
36. Chirvase, D., Parisi, J., Hummelen, J. C. & Dyakonov, V. Influence of nanomorphology on the photovoltaic action of polymer-fullerene composites. *Nanotechnology* **15**, 1317–1323 (2004).
37. Huang, J., Li, G. & Yang, Y. Influence of composition and heat-treatment on the charge transport properties of poly(3-hexylthiophene) and [6,6]-phenyl C61 -butyric acid methyl ester blends. *Appl Phys Lett* **87**, (2005).

38. Li, G. *et al.* High-efficiency solution processable polymer photovoltaic cells by self-organization of polymer blends. *Nat Mater* **4**, 864–868 (2005).
39. Reyes-Reyes, M., Kim, K. & Carroll, D. L. High-efficiency photovoltaic devices based on annealed poly(3-hexylthiophene) and 1-(3-methoxycarbonyl)-propyl-1- phenyl- (6,6) C61 blends. *Appl Phys Lett* **87**, (2005).
40. Li, G. *et al.* 'Solvent annealing' effect in polymer solar cells based on poly(3-hexylthiophene) and methanofullerenes. *Adv Funct Mater* **17**, 1636–1644 (2007).
41. Mihailetchi, V. D. *et al.* Origin of the enhanced performance in poly(3-hexylthiophene): [6,6]-phenyl C61-butyric acid methyl ester solar cells upon slow drying of the active layer. *Appl Phys Lett* **89**, (2006).
42. Arca, F., Loch, M. & Lugli, P. Enhancing efficiency of organic bulkheterojunction solar cells by using 1,8-diiodooctane as processing additive. *IEEE J Photovolt* **4**, 1560–1565 (2014).
43. Nasiri, M. & Abbasi, F. Effect of 1,8-diiodooctane on the performance of P3HT: PCBM solar cells. *Journal of Solar Energy Engineering, Transactions of the ASME* **137**, (2015).
44. Bertho, S. *et al.* How stable are polymer:PCBM bulk heterojunction solar cells? in *Organic Optoelectronics and Photonics II* vol. 6192 619225 (SPIE, 2006).
45. Bertho, S. *et al.* Effect of temperature on the morphological and photovoltaic stability of bulk heterojunction polymer:fullerene solar cells. *Solar Energy Materials and Solar Cells* **92**, 753–760 (2008).
46. Han, J., Xu, H., Paleti, S. H. K., Sharma, A. & Baran, D. Understanding photochemical degradation mechanisms in photoactive layer materials for organic solar cells. *Chemical Society Reviews* vol. 53 7426–7454 (2024).
47. Cameron, J. & Skabara, P. J. The damaging effects of the acidity in PEDOT:PSS on semiconductor device performance and solutions based on non-acidic alternatives. *Materials Horizons* vol. 7 1759–1772 (2020).
48. Duan, L. & Uddin, A. Progress in Stability of Organic Solar Cells. *Advanced Science* vol. 7 (2020).
49. Patel, J. B. *et al.* Effect of Ultraviolet Radiation on Organic Photovoltaic Materials and Devices. *ACS Appl Mater Interfaces* **11**, 21543–21551 (2019).

50. Zhao, H., Prine, N., Kundu, S., Ma, G. & Gu, X. Effect of Thermal Stress on Morphology in High-Performance Organic Photovoltaic Blends. *JACS Au* **4**, 4334–4344 (2024).
51. Krebs, F. C. Fabrication and processing of polymer solar cells: A review of printing and coating techniques. *Solar Energy Materials and Solar Cells* vol. 93 394–412 (2009).
52. Glen, T. S. *et al.* Grain size dependence of degradation of aluminium/calcium cathodes in organic solar cells following exposure to humid air. *Solar Energy Materials and Solar Cells* **140**, 25–32 (2015).
53. Gong, X. Toward high performance inverted polymer solar cells. *Polymer* vol. 53 5437–5448 (2012).
54. Uddin, A., Upama, M. B., Yi, H. & Duan, L. Encapsulation of organic and perovskite solar cells: A review. *Coatings* vol. 9 (2019).
55. Zhang, B., Wang, Z., Wang, J. & Chen, X. Recent Achievements for Flexible Encapsulation Films Based on Atomic/Molecular Layer Deposition. *Micromachines* vol. 15 (2024).
56. Ha, S. R. *et al.* Water-resistant PEDOT:PSS hole transport layers by incorporating a photo-crosslinking agent for high-performance perovskite and polymer solar cells. *Nanoscale* **10**, 13187–13193 (2018).
57. Xiong, S. *et al.* Waterproof and ultraflexible organic photovoltaics with improved interface adhesion. *Nat Commun* **15**, (2024).
58. Song, W. *et al.* An in situ crosslinked matrix enables efficient and mechanically robust organic solar cells with frozen nano-morphology and superior deformability. *Energy Environ Sci* (2024)
59. Yoon, S. *et al.* Molecular Cross-Linking Enhances Stability of Non-Fullerene Acceptor Organic Photovoltaics. *ACS Energy Lett* **10**, 541–551 (2025).
60. Burke, T. M., Sweetnam, S., Vandewal, K. & McGehee, M. D. Beyond Langevin recombination: How equilibrium between free carriers and charge transfer states determines the open-circuit voltage of organic solar Cells. *Adv Energy Mater* **5**, (2015).
61. Kozub, D. R. *et al.* Polymer crystallization of partially miscible polythiophene/fullerene mixtures controls morphology. *Macromolecules* **44**, 5722–5726 (2011).
62. He, K., Kumar, P., Yuan, Y. & Li, Y. Wide bandgap polymer donors for high efficiency non-fullerene acceptor based organic solar cells. *Materials Advances* vol. 2 115–145 (2021).

63. Wang, H. Y. *et al.* Multiple-Trapping Model for the Charge Recombination Dynamics in Mesoporous-Structured Perovskite Solar Cells. *ChemSusChem* **10**, 4872–4878 (2017).
64. Zheng, Z., Tummala, N. R., Fu, Y. T., Coropceanu, V. & Brédas, J. L. Charge-Transfer States in Organic Solar Cells: Understanding the Impact of Polarization, Delocalization, and Disorder. *ACS Appl Mater Interfaces* **9**, 18095–18102 (2017).
65. Wang, T. *et al.* Correlating Charge Transfer Dynamics with Interfacial Trap States in High-Efficiency Organic Solar Cells. *ACS Appl Mater Interfaces* **15**, 12109–12118 (2023).
66. Arndt, A. P. *et al.* Time-resolved charge-transfer state emission in organic solar cells: Temperature and blend composition dependences of interfacial traps. *Journal of Physical Chemistry C* **119**, 13516–13523 (2015).
67. Chen, M. *et al.* Influences of Non-fullerene Acceptor Fluorination on Three-Dimensional Morphology and Photovoltaic Properties of Organic Solar Cells. *ACS Appl Mater Interfaces* **11**, 26194–26203 (2019).
68. Sharma, R., Jain, N., Lee, H., Kabra, D. & Yoo, S. Comprehensive and Comparative Analysis of Photoinduced Charge Generation, Recombination Kinetics, and Energy Losses in Fullerene and Nonfullerene Acceptor-Based Organic Solar Cells. *ACS Appl Mater Interfaces* **12**, 45083–45091 (2020).
69. Wang, Z. *et al.* Mechanistic Investigation into Dynamic Function of Third Component Incorporated in Ternary Near-Infrared Nonfullerene Organic Solar Cells. *Adv Funct Mater* **30**, (2020).
70. Yang, C. *et al.* Nonfullerene Ternary Organic Solar Cell with Effective Charge Transfer between Two Acceptors. *Journal of Physical Chemistry Letters* **11**, 927–934 (2020).
71. He, L., Wan, C., Dong, H., Zhang, X. & Huang, J. Enhancing Open-Circuit Voltage and Charge Transportation for Ternary Organic Solar Cells with Energy Cascade Double Nonfullerene Acceptors. *IEEE J Photovolt* **9**, 1290–1296 (2019).
72. Song, C. E., Ham, H., Noh, J., Lee, S. K. & Kang, I. N. Efficiency enhancement of a fluorinated wide-bandgap polymer for ternary nonfullerene organic solar cells. *Polymer (Guildf)* **188**, (2020).
73. Firdaus, Y. *et al.* Charge transport and recombination in wide-bandgap Y6 derivatives-based organic solar cells. *Advances in Natural Sciences: Nanoscience and Nanotechnology* **13**, (2022).

74. Wang, J. *et al.* Ultra-narrow bandgap non-fullerene organic solar cells with low voltage losses and a large photocurrent. *J Mater Chem A Mater* **6**, 19934–19940 (2018).
75. Oh, C. M., Lee, J., Park, S. H. & Hwang, I. W. Carrier losses in non-geminate charge-transferred states of nonfullerene acceptor-based organic solar cells. *Spectrochim Acta A Mol Biomol Spectrosc* **250**, (2021).
76. Gélinas, S. *et al.* Ultrafast Long-Range Charge Separation in Organic Semiconductor Photovoltaic Diodes. *Science* **343**, 512-516 (2014).
77. Tress, W. *et al.* Imbalanced mobilities causing S-shaped IV curves in planar heterojunction organic solar cells. *Appl Phys Lett* **98**, (2011).
78. Foertig, A., Rauh, J., Dyakonov, V. & Deibel, C. Shockley equation parameters of P3HT:PCBM solar cells determined by transient techniques. *Phys Rev B Condens Matter Mater Phys* **86**, (2012).
79. Shuttle, C. G. *et al.* Charge extraction analysis of charge carrier densities in a polythiophene/fullerene solar cell: Analysis of the origin of the device dark current. *Appl Phys Lett* **93**, (2008).
80. Howard, I. A., Mauer, R., Meister, M. & Laquai, F. Effect of morphology on ultrafast free carrier generation in polythiophene:fullerene organic solar cells. *J Am Chem Soc* **132**, 14866–14876 (2010).
81. Palomares, E. & Albero, J. Measuring efficiency losses in quantum dot polymer solar cells. in *Organic Photonics V* vol. 8435 843509 (SPIE, 2012).
82. Azzouzi, M. *et al.* Overcoming the Limitations of Transient Photovoltage Measurements for Studying Recombination in Organic Solar Cells. *Solar RRL* **4**, (2020).
83. Etzold, F. *et al.* Ultrafast exciton dissociation followed by nongeminate charge recombination in PCDTBT:PCBM photovoltaic blends. *J Am Chem Soc* **133**, 9469–9479 (2011).
84. Zhang, H. *et al.* Effects of DIO on the charge recombination behaviors of PTB7:PC71BM photovoltaics. *Org Electron* **67**, 50–56 (2019).
85. Mozer, A. J. *et al.* Charge transport and recombination in bulk heterojunction solar cells studied by the photoinduced charge extraction in linearly increasing voltage technique. *Appl Phys Lett* **86**, 1–3 (2005).

86. Vijila, C. *et al.* Relation between charge carrier mobility and lifetime in organic photovoltaics. *J Appl Phys* **114**, (2013).
87. Albrecht, S. *et al.* On the field dependence of free charge carrier generation and recombination in blends of PCPDTBT/PC 70BM: Influence of solvent additives. *Journal of Physical Chemistry Letters* **3**, 640–645 (2012).
88. Kurpiers, J. & Neher, D. Dispersive Non-Geminate Recombination in an Amorphous Polymer:Fullerene Blend. *Sci Rep* **6**, (2016).
89. Kniepert, J. *et al.* Reliability of charge carrier recombination data determined with charge extraction methods. *J Appl Phys* **126**, (2019).
90. Scher, H. & Montroll, E. N. . Anomalous Transit-Time Dispersion in Amorphous Solids. *Phys. Rev. B* **12**, 2455 (1975).
91. Juška, G. & Genevičius, K. Investigation of recombination in organic heterostructures by i-CELIV. *Appl Phys Lett* **113**, (2018).
92. Kavan, L. & Grätzel, M. Highly efficient semiconducting TiO2 photoelectrodes prepared by aerosol pyrolysis. *Electrochim Acta* **40**, 643–652 (1995).
93. Guo, S. *et al.* Influence of solvent and solvent additive on the morphology of PTB7 films probed via X-ray scattering. *Journal of Physical Chemistry B* **118**, 344–350 (2014).
94. Presselt, M. *et al.* Sub-bandgap absorption in polymer-fullerene solar cells studied by temperature-dependent external quantum efficiency and absorption spectroscopy. *Chem Phys Lett* **542**, 70–73 (2012).
95. Sun, X. *et al.* Dopant-Free Crossconjugated Hole-Transporting Polymers for Highly Efficient Perovskite Solar Cells. *Advanced Science* **7**, (2020).
96. Wu, J. *et al.* Fluorinated Cross-linkable and Dopant-free hole transporting materials for efficient and stable perovskite solar cells. *Chemical Engineering Journal* **422**, (2021).
97. Abraham, S., Ganesh, G. P. T., Varughese, S., Deb, B. & Joseph, J. Cross-Linkable Fluorene-Diphenylamine Derivatives for Electrochromic Applications. *ACS Appl Mater Interfaces* **7**, 25424–25433 (2015).
98. Ribeiro-Claro, P. J. A., Amado, A. M. & Teixeira-Dias, J. J. C. Substituted styrene molecules included in cyclodextrins: A Raman spectroscopic study. Part II. *Journal of Raman Spectroscopy* **27**, 155–161 (1996).

99. Noda, L. K. & Sala, O. *A Resonance Raman Investigation on the Interaction of Styrene and 4-Methyl Styrene Oligomers on Sulphated Titanium Oxide*. *Spectrochimica Acta Part A* vol. 56 (1999).
100. Bässler, H. Charge Transport in Disordered Organic Photoconductors a Monte Carlo Simulation Study. *Physica Status Solidi (B)* **175**, 15–56 (1993).
101. Valouch, S., Nintz, M., Kettlitz, S. W., Christ, N. S. & Lemmer, U. Thickness-dependent transient photocurrent response of organic photodiodes. *IEEE Photonics Technology Letters* **24**, 596–598 (2012).
102. McNeill, C. R., Hwang, I. & Greenham, N. C. Photocurrent transients in all-polymer solar cells: Trapping and detrapping effects. *J Appl Phys* **106**, (2009).
103. Presselt, M. *et al.* Sub-bandgap absorption in polymer-fullerene solar cells studied by temperature-dependent external quantum efficiency and absorption spectroscopy. *Chem Phys Lett* **542**, 70–73 (2012).

APPENDIX I

Below the fundamental principles for calculating charge, current, and electric field in the EIC method are presented in detail.

Once injected, charge carriers are moving through the material due to the drift and diffusion. Drift current is described by:

$$j_{dr} = eE(n\mu_e + p\mu_h) = \frac{1}{S}\frac{dQ_{dr}}{dt} \quad (A.1)$$

where j_{dr} is the drift current density, n and p are electron and hole concentrations, μ_e and μ_h are electron and hole mobilities respectively. Electron and hole drift current density in cell i :

$$\frac{1}{S}\frac{dQ_{n,dr_i}}{dt} = \frac{1}{S}eSdx\frac{dn_{dr_i}}{dt} = eE_i n_i \mu_e \quad (A.2)$$

Number of electrons leaving cell i because of drift:

$$dn_{dr_i} = E_i n_i \mu_e dt\frac{1}{dx} \quad (A.3)$$

In parallel, diffusion currents arise from concentration gradients between neighboring cells. The diffusion current for electrons is given by:

$$j_{diff} = eD_n\frac{dn_{dif}}{dx} - eD_p\frac{dp_{dif}}{dx} = \frac{1}{S}\frac{dQ_{n,dif}}{dt} \quad (A.4)$$

where *D* is diffusion coefficient for holes and electrons, which is related to mobility through the Einstein relation:

$$D_n = \frac{kT\mu_e}{e}, \quad (A.5)$$

The diffusion of electrons and holes between cells is governed by Fick's law. The change in electron concentration in cell i due to diffusion in cell j is calculated as:

$$edx\frac{dn_{dif_i}}{dt} = kT\mu_e\frac{n_i - n_j}{dx} \quad (A.6)$$

$$dn_{dif_i} = kT\mu_e\frac{1}{edx}\frac{n_i - n_j}{dx}dt \quad (A.7)$$

Both drift and diffusion contribute to the redistribution of electrons and holes across the cells, which in turn modifies the electric field.

Recombination is another critical process that affects the number of free carriers available for collection. The recombination rate follows Langevin bimolecular recombination, where the rate of recombination is proportional to the product of the electron and hole mobilities. However, as mentioned before, in BHJ systems, the recombination rate is often lower than predicted by the

standard Langevin model. This is accounted for by introducing a reduction factor r:

$$\frac{dn}{dt} = \frac{dp}{dt} = \frac{B_L}{r} np \qquad (A.8)$$

This changes electron and hole concentrations in the cell i accordingly:

$$dn_{R_i} = dp_i = \frac{B_L}{r} n_i p_i \, dt \qquad (A.9)$$

The movement of charge carriers and their recombination affect the electric field within the sample. This electric field is recalculated at every time step using Poisson's equation, which relates the electric field to the local charge density ρ:

$$\frac{dE}{dx} = -\frac{e\rho}{\varepsilon\varepsilon_0} = \frac{e(n-p)}{\varepsilon\varepsilon_0} \qquad (A.10)$$

The change in electric field across the boundaries of a cell due to the difference in electron and hole concentrations is given by:

$$dE_i = \frac{e(n_i - p_i)}{\varepsilon\varepsilon_0} dx \qquad (A.11)$$

This equation indicates that if the concentrations of electrons and holes differ within a cell, the electric field at the edges of the cell will vary accordingly. The electric field must also satisfy the condition that its integral over the entire sample equals the applied voltage:

$$\int_0^d E(x) \, dx = U \qquad (A.12)$$

APPENDIX II

Table A1. Thermal, optical and photophysical properties of **V1145, V1177, V1178** and **V1179.**

HTM	T_g (°C)	T_m (°C)	T_{d5} (°C)	T_c (°C)	$\lambda_{abs.}$ (nm)	I_p (eV)	I^*_p (eV)
V1145		181.5	400	193.9	259, 307, 378	5.11	5.18
V1177	79.4	158.5	396	191.6	259, 307, 383	5.16	5.15
V1178		208.4	387	218.6	259, 309, 383	5.19	5.20
V1179	110.7		403	204.8	260, 288, 383	5.41	5.38

Glass transition (T_g), melting point (T_m), 5% weight loss (T_{d5}), and cross-linking (T_c) temperatures from DSC and TGA, respectively (10 °C/min, N_2 atmosphere)

Ionization energies (I_p) of the films measured using PESA.

Ionization energies (I^*_p) of the cross-linked films measured using PESA.

APPENDIX III

List of several most probable molecular dimers is presented in Table A2 with several most informative projections (not xy) of the mentioned conformations. Those structures were obtained by A.Gruodis using grad optimization technique (convergence of parameters Maximum Force, RMS Force, Maximum Displacement, RMS Displacement has been achieved). Electronic excitations were simulated using semiempirical TD method (for singlets).

Table A2. List of molecular dimers.

Compound	Two initial conformers	Molecular structure after ground state energy optimization using *Gaussian16*, CAM-B3LYP/6-31G(d,p) basis set
Eh0	V1421b + V1421b	
Eh2	V1458b + V1458b	

Projection1

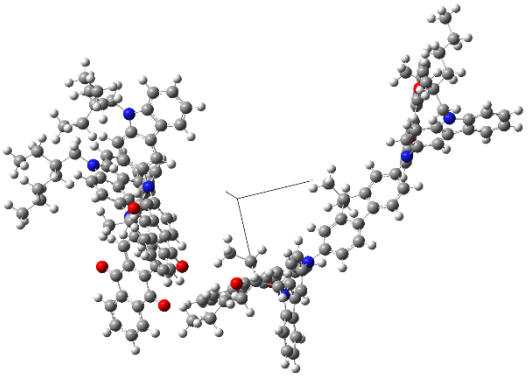

Projection2

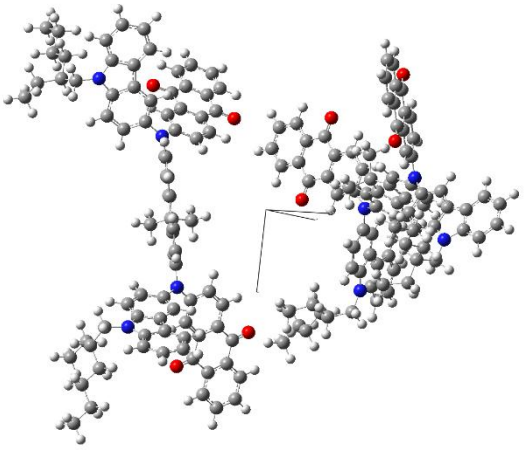

Dimer **Eh0 (**V1421b + V1421b**)**

Projection

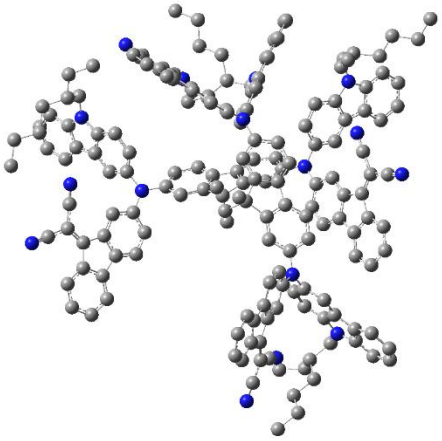

Eh2 (V1458b + V1458b**)**

Presented below are time-of-flight transients of bipolar charge transporting materials (V1393, V1421, V1457, V1458, V1484, V1485).

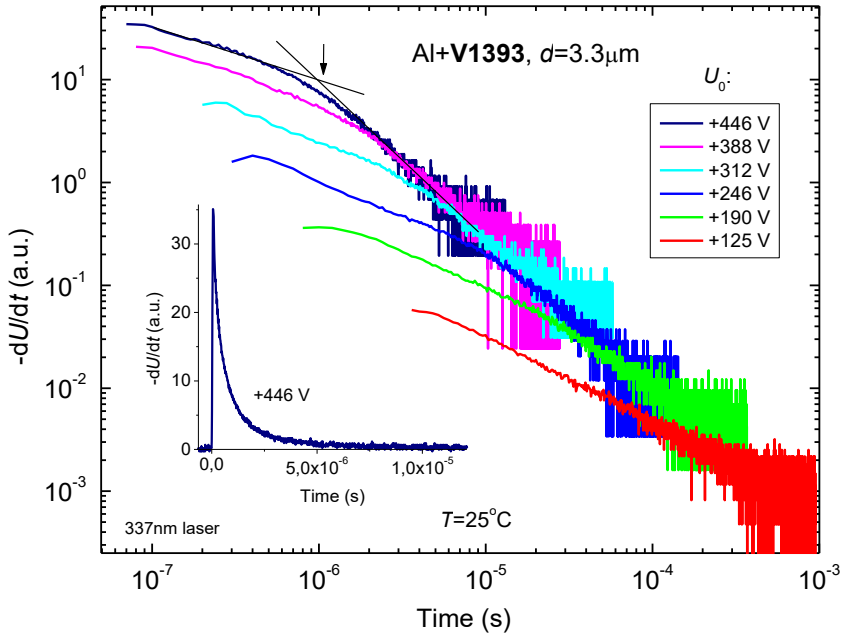

a)

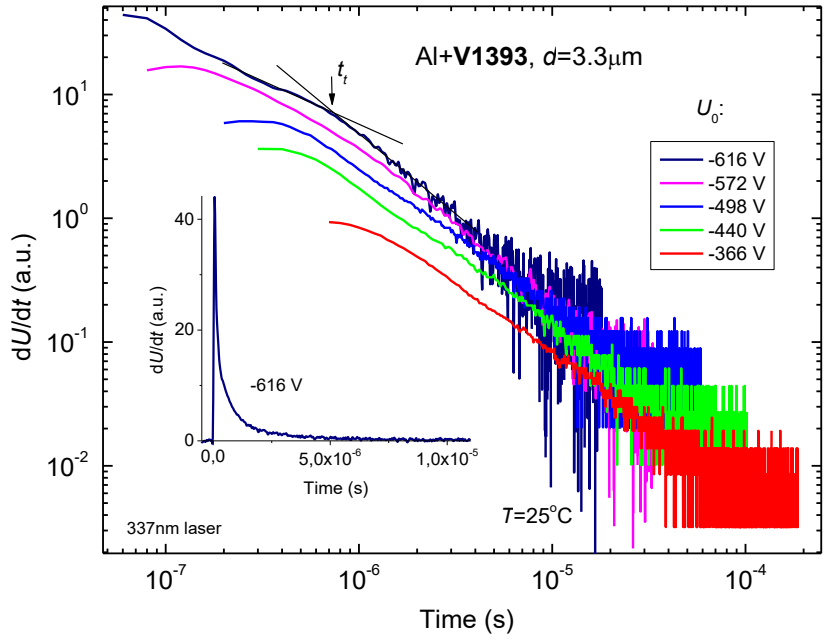

b)

Figure A1. XTOF transients in V1393 sample of holes (a) and electrons (b).

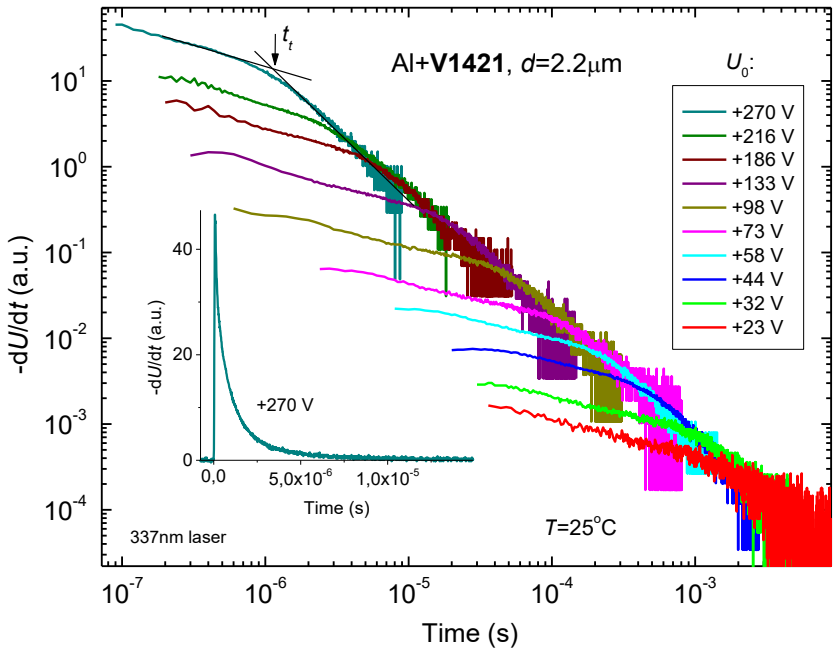

a)

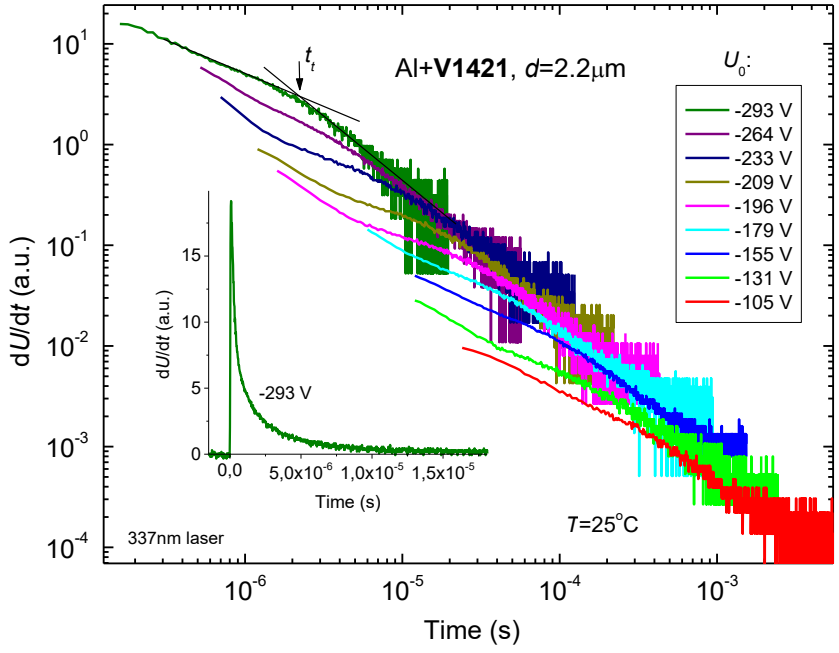

b)

Figure A2. XTOF transients in V1421 sample of holes (a) and electrons (b).

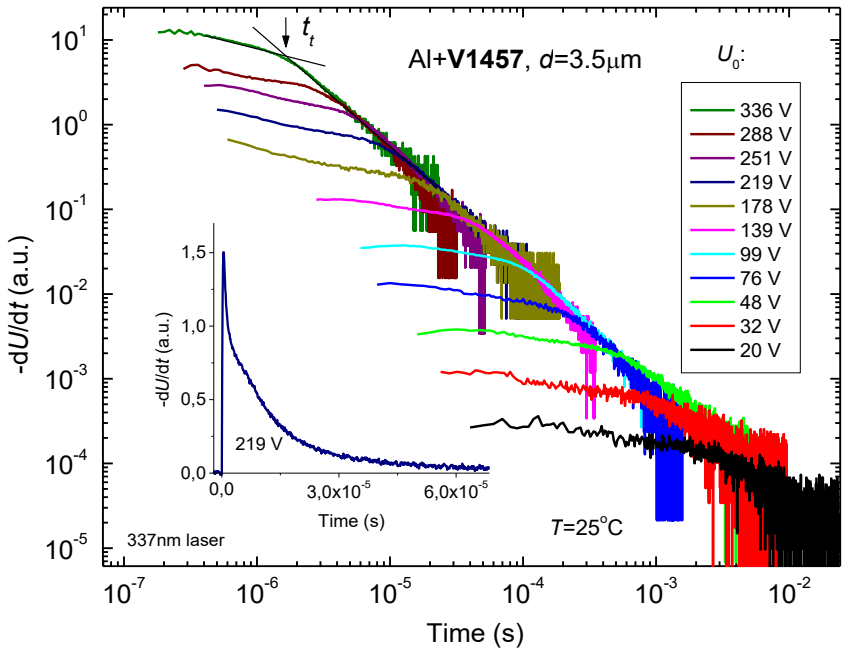

a)

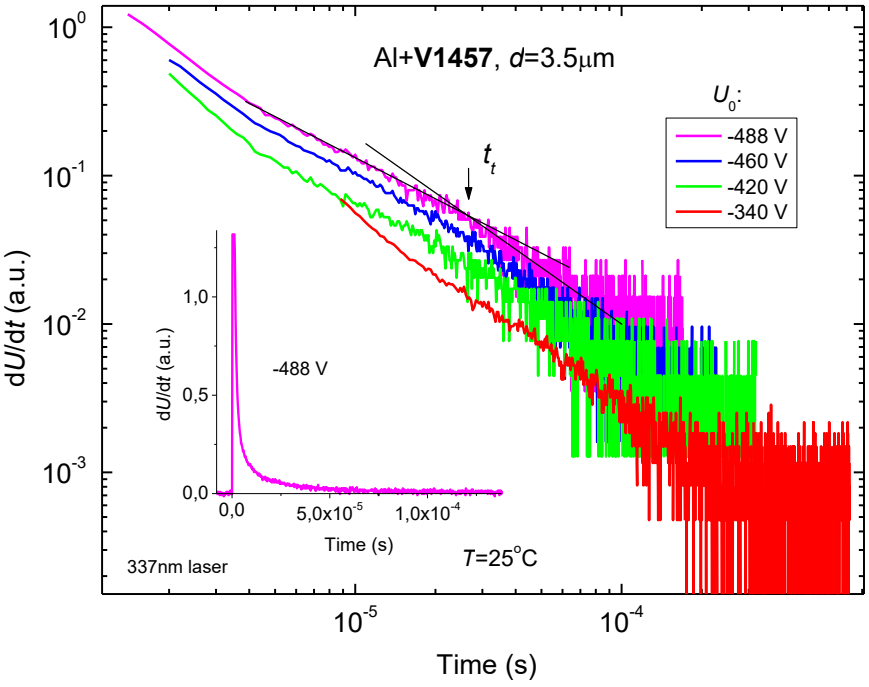

b)

Figure A3. XTOF transients in V1457 sample of holes (a) and electrons (b).

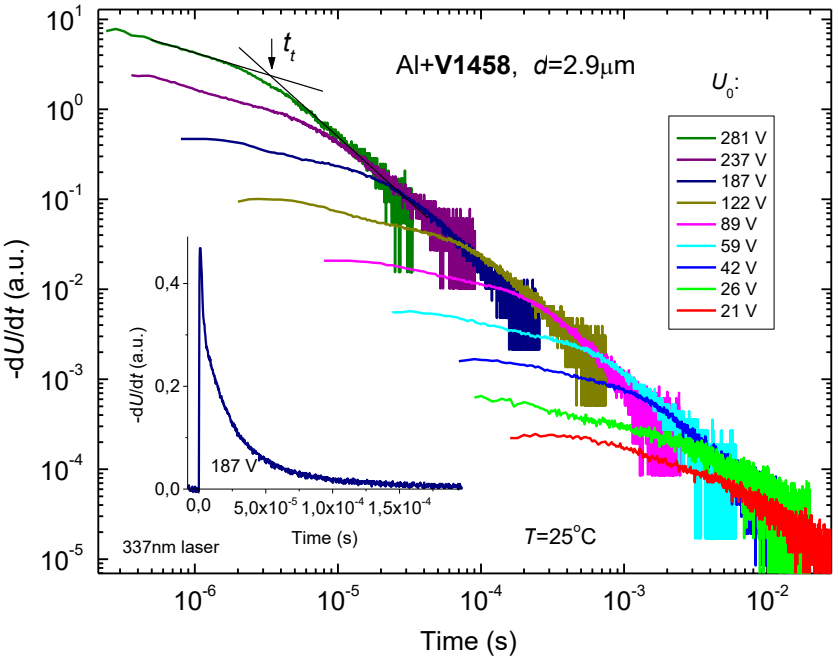

a)

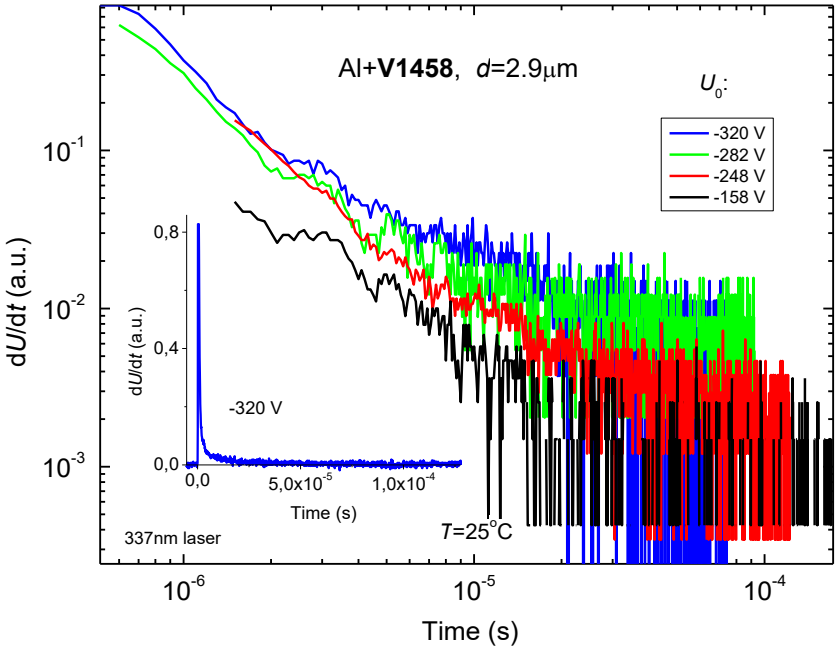

b)

Figure A4. XTOF transients in V1458 sample of holes (a) and electrons (b).

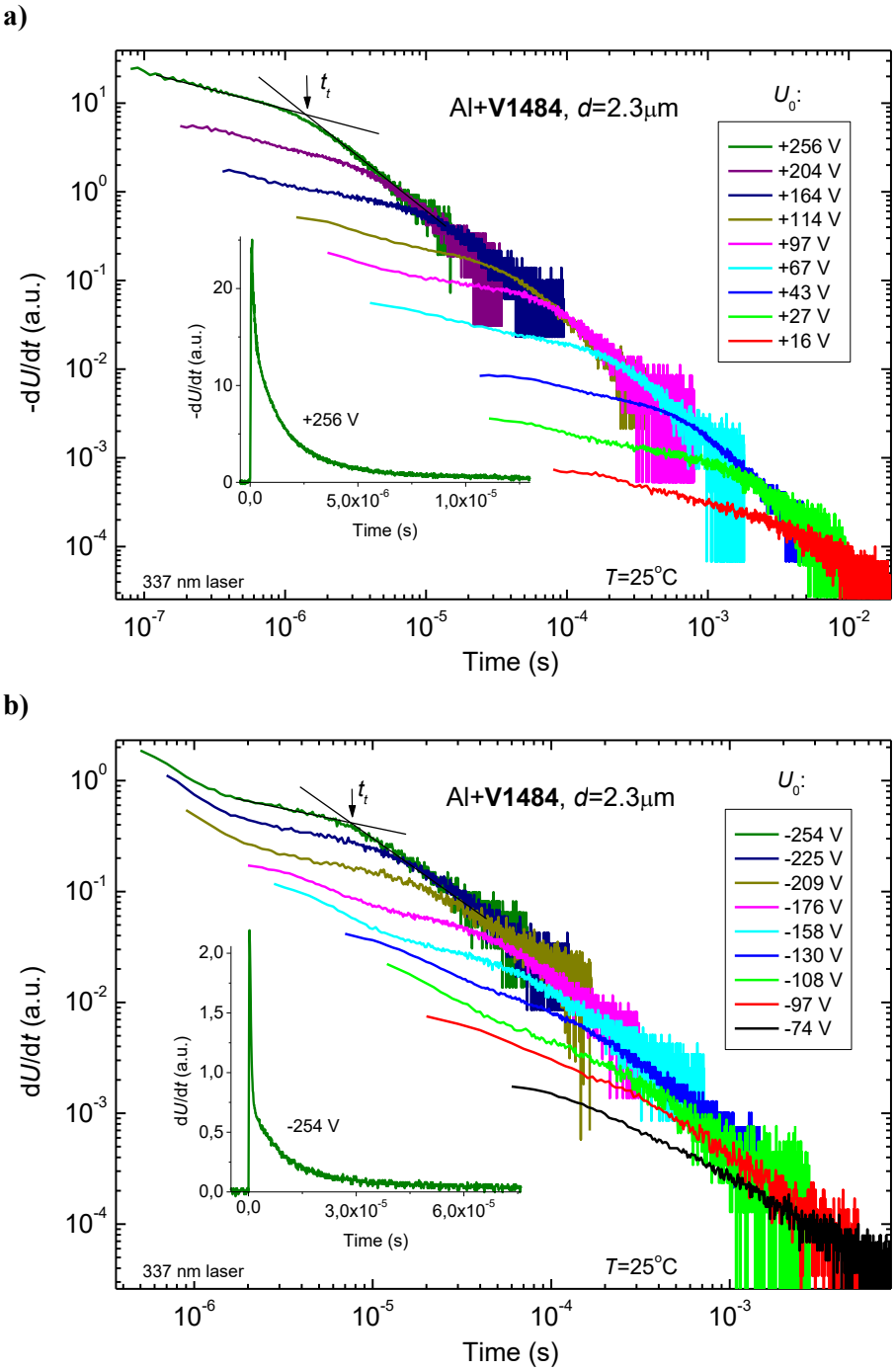

Figure A5. XTOF transients in V1484 sample of holes (a) and electrons (b).

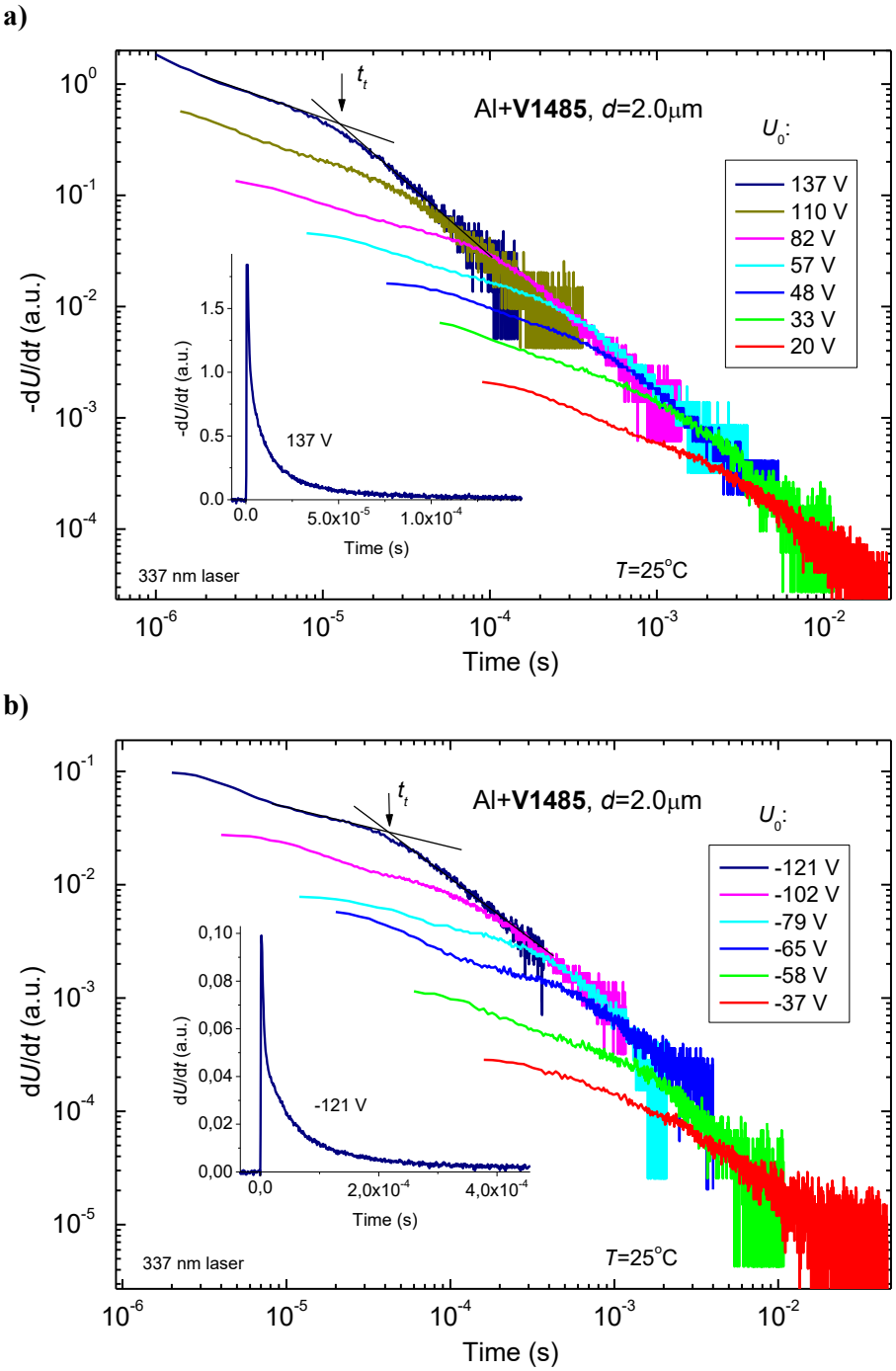

Figure A6. XTOF transients in V1485 sample of holes (a) and electrons (b).

NOTES

Vilniaus universiteto leidykla
Saulėtekio al. 9, III rūmai, LT-10222 Vilnius
El. p. info@leidykla.vu.lt, www.leidykla.vu.lt
bookshop.vu.lt, journals.vu.lt
Tiražas 15 egz.